Bi-Te and Sb-Te Topological Insulator Materials: from first principle calculations towards nanostructures fabrication

Sofia Ferreira Teixeira
Mestrado em Física
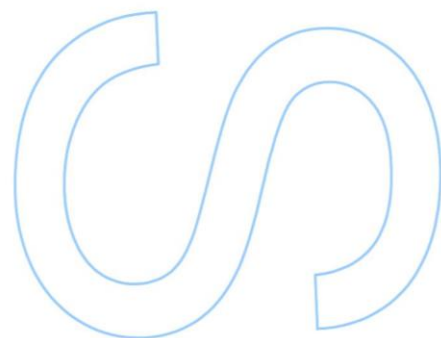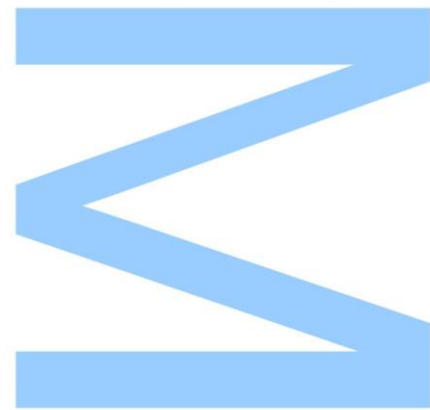Departamento de Física e Astronomia
2017

Orientador
André Miguel Trindade Pereira
Professor Auxiliar, Faculdade de Ciências da Universidade do Porto

Coorientador
João Pedro Esteves Araújo
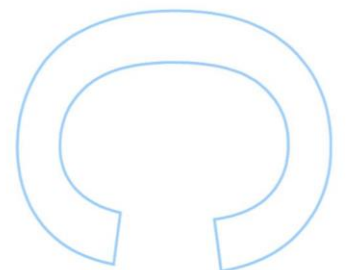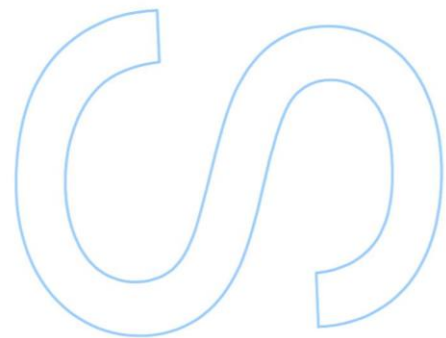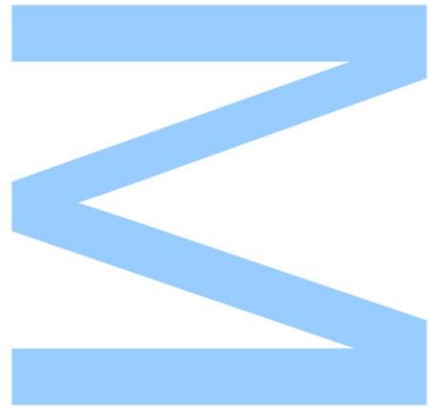Professor Associado, Faculdade de Ciências da Universidade do Porto

U. PORTO

FC FACULDADE DE CIÊNCIAS
UNIVERSIDADE DO PORTO

Todas as correções determinadas
pelo júri, e só essas, foram efetuadas.

O Presidente do Júri,

Porto, _____/_____/_____

Acknowledgements

First of all, I would like to give an enormous thank you to my supervisor, Professor André Pereira, for always pushing me forward, for what is almost four years now, and for allowing me to pursue what is a new research topic. Without his great knowledge and constant support and incentive, this work would not have been possible. To Professor João Pedro Araújo, I would also like to thank for all the insights given when needed and for also always giving me support for the development of my ideas.

This dissertation would not have also been possible without everyone at IFIMUP-IN. The most warmest thank you goes to Ana Lúcia Pires. Although my work sounds like a bunch of crazy stuff, you were always there for me, either to help me with almost all the experimental part or for the moral support needed to be able to complete such an endeavour. I would also like to thank Rui Mário Costa, for teaching me the basics of WIEN2k and for his patience whenever I needed help. A big thank you is also due to Inês Figueiredo, for all the cheerful mornings and help, to Sílvio, for his help with the cryostat measurements and to Gonçalo Oliveira for helping with the magnetoresistance measurements.

This cannot be complete without also a big thank you to everyone who founded and worked with me at PhysikUP, the Núcleo de Física, Engenharia Física e Astronomia da Faculdade de Ciências da Universidade do Porto. To Simão Sá, for being my voice when I couldn't and to Margarida Maia, who is always offering her help and who shared the lab with me in the summer and had the patience to put up with me. To Rita Lima, for sharing the craziness of writing a master thesis and for her dedication and to Rúben Azinheira Alves, for accepting my offer of founding this crazy project of ours just one week after we met. To everyone at PhysikUP, thank you. We did a great thing that hopefully will improve being a physics student at Porto. A thank you also goes to my non Porto physics friends. To Pedro Vianez, for sharing all the problems of doing physics and for all the times at the lab, to Siddharth Mahesh for his patience and support at the finish of this thesis and to Albana Topi for all her advices and for pulling me up.

Last but not least, the biggest of thank you goes to my family, because I would not be here without all of you. To my dad for all his attentiveness, to my godmum for always being there when I needed and to my goddad for always showing interest in the explanations of my work. Lastly, to my mum, without whom all this would not have

been possible. For always being there, for always helping me, for always pushing me and calming my stress down, for all the devotion. Thank you.

Abstract

Topological Insulators (TI) are a recently discovered category of materials, with the term TI only being coined in 2007. They host a protected metallic state on their surface while having an insulating bulk. This state appears in the form of a spin-textured Dirac cone, where spin is locked with momentum. A wide range of applications are foreseen to exist for TI materials. However, more studies and experimental realisation of the TI materials and tuning of the TI state must be accomplished.

TI based on Bi-Te and Sb-Te were fabricated and first principle calculations were performed. Optimised bulk Bi_2Te_3 was synthesised by a solid state reaction and its morphological, structural and transport properties were characterised using numerous techniques, such as SEM, XRD, EDS, temperature dependent resistivity measurements, among others. A great agreement between the transport measurements and the literature was obtained. Using WIEN2k and the BoltzTraP code to calculate the electronic and transport properties of Bi_2Te_3, showed that they are powerful numerical tools due to the good agreement between the experimental results and the theoretical calculations.

On nanostructures, Ion Beam Sputtering Deposition (IBD) was used to fabricate Sb_2Te_3 thin films in glass and Si substrates. The morphology and structure were characterised and the transports properties were measured. An extrinsic semiconductor behaviour was observed in the resistivity dependence with temperature. The bulk band gap of the thin films was calculated from the resistivity and it is between 60 and 120 meV, increasing with film thickness. The Seebeck coefficient of the Sb_2Te_3 thin films was obtained, verifying that the substrate greatly influences this property. First principle calculations of bulk Sb_2Te_3 and 3 nm Sb_2Te_3 thin film (supercell calculation) were also performed and the existence of the TI state in the thin film was observed. Magnetoresistance measurements at high magnetic fields were performed, evidencing the Shubnikov-de Haas effect and estimating the presence of the TI surface state.

To tune the TI state of the Sb_2Te_3 thin films, $NiFe/Sb_2Te_3$ heterostructures were fabricated using IBD and characterised, with the intended structure and morphology being obtained. The behaviour of the transport properties showed the strong interaction between the magnetic and topological insulator layer.

Resumo

Isoladores Topológicos (TI) são uma categoria de materiais recentemente desoberta, sendo que o termo TI só existiu em 2007. Eles apresentam um estado metálico protegido na sua superfície mas um *bulk* isolador. Este estado aparece na forma de um cone de Dirac, em que o spin está fixo ao momento. Várias aplicações são esperadas para estes materiais. No entanto, mais estudos, realizações experimentais e controlo do estado TI têm que ser obtidos.

Materiais TI baseados em Bi - Te e Sb - Te foram fabricados e cálculos de primeiros princípios foram efetuados. *Bulk* Bi_2Te_3 foi produzido por uma reação de estado sólido e as suas propriedades morfológicas, estruturais e de transporte foram caracterizadas usando várias técnicas, como SEM, XRD, EDS, medidas de resistividade em função da temperatura, entre outras. Um acordo excelente entre as medidas das propriedades de transporte e a literatura foi obtido. O uso do *software* WIEN2k e do código BoltzTraP para calcular as propriedades electrónicas e de transporte, mostrou que são ferramentas numéricas poderosas devido ao acordo entre os resultados experimentais e os cálculos teóricos.

Para as nanoestruturas, *Ion Beam Sputtering Deposition* (IBD) foi utilizada para fabricar filmes finos de Sb_2Te_3 em substratos de vidro e Si. A morfologia e estrutura foram caracterizadas e as propriedades de transporte medidas. A resistividade em função da temperatura revelou um comportamento de semicondutor extrinsico. O *bulk band gap* dos filmes foi calculado pelas medidas de resistividade e está entre 60 a 120 meV, aumentando com a sua espessura. O coeficiente de seebeck dos filmes de Sb_2Te_3 foi obtido, tendo-se verificado que o substrato influência esta propriedade. Cálculos de primeiros princípios do *bulk* e 3 nm filme fino (cálculo *supercell*) de Sb_2Te_3 foram feitos e a existência do estado TI para o filme fino foi observada. Medidas de magnetoresistência foram feitas para altos campos, mostrando a evidência das Shubnikov-de Haas oscilações, o que permite estimar a presença do estado de superfície TI.

Para controlar o estado TI dos filmes de Sb_2Te_3, heteroestruturas de $NiFe/Sb_2Te_3$ foram fabricadas usando IBD e caracterizadas, tendo-se obtido a estrutura e morfologia pretendida. O comportamento das propriedades de transporte mostrou uma interação forte entre as camadas magnética e TI.

Contents

List of Figures

List of Tables

Abbreviations

APW	Augmented Plane Waves
APW+lo	Augmented Plane Waves + linear orbits
ARPES	Angle Resolved Photoemission Spectroscopy
DOS	Density of States
EDS	Electron X-ray Dispersive Spectroscopy
GGA	Generalised Gradient Approximation
IBD	Ion Beam Sputtering Deposition
LAPW	Linear Augmented Plane Waves
LDA	Local Density Approximation
MR	MagnetoResistance
SEM	Scanning Electron Microscopy
SOC	Spin Orbit Coupling
TI	Topological Insulator
XRD	X-ray Diffraction
XRR	X-ray Reflectivity

Dedicated to my mother, Carolina Ferreira, for all her dedication...

Chapter 1

Introduction

At the end of the last century, physicists thought all the materials could be categorized as either insulators, conductors or semiconductors, based on the theory of electronic bands. However, some theoretical work and later experimental verifications revolutionized the condensed matter world when a new type of materials was proposed: the topological insulators (TI).

The different phases of matter can be classified by their symmetries and how they are spontaneously broken. In the last years, however, a new way of classifying materials appeared based on the concept of topological order, first developed by Thouless et. al, 2016 Nobel Prize in Physics, in the 80's [1]. Based on spin-orbit coupling, a new type of materials appeared called topological insulators, having an exotic metallic surface state protected by time reversal symmetry, but an insulating bulk. This is a simple explanation, but their theoretical description and even more their experimental realization is not as easy to obtain.

Since 2004, that a lot of work has been done on topological insulators, either theoretical or experimental, having the term being coined only in 2007. Considered a hot topic, after the 2016 Nobel physics prize on the subject and 1141 papers having been published on topological insulators just in 2016 while only 12 in 2004, it is expected that topological insulators research will grow even more. Being a fundamental physics research topic [2], they also attract interest due to possible applications in spintronic and quantum computation [3–5]. This means that in the future, fundamental research will lead to devices being fabricated using topological insulators that take advantage of its exotic properties.

In this dissertation, topological insulators based on Bi-Te and Sb-Te are thoroughly studied and analysed, both experimentally and theoretically. The first proposal of this

dissertation is to realise experimentally topological insulators in bulk form by a solid reaction and in thin film form, by using a scalable and industrialised nano fabrication procedure, such as Ion Beam Sputtering Deposition. A deep study into the morphological and structural properties of the fabricated materials as well as an extensive analysis into their transport properties is also sought after. In parallel, a theoretical description of the electronic structure of Bi-Te and Sb-te materials and the calculation of their transport properties is coveted. With the realisation of the topological insulators thin film materials, a tuning of its properties by coupling with NiFe permalloy magnetic material layers is pursued.

In Chapter 2, an overview of the topological insulators is presented. The emergence of the time reversal protected surface topological state is explained and compared to other exotic insulator effects such as the Quantum Hall state. A description of the first theoretical prediction of a TI material and its experimental realisation is described. The most important TI materials are analysed, with a focus on the Bi_2Te_3 family of semiconductors, followed by the experimental signatures of their topological surface state.

Chapter 3 comprises the experimental material fabrication methods as well as the different performed characterisations and measurements techniques. These characterisations are essential in order to evaluate the structure of the fabricated samples and evaluate their quality. The different techniques deployed to study the electronic transport properties of the samples are also essential to the completion of the proposed work.

The description of first principle calculations of the electronic properties of the TI materials is presented in Chapter 4. Density functional theory calculations are explained and the WIEN2k software package is presented as one of the best existing packages to calculate TI properties. The BoltzTraP code is also briefly described as a tool to calculate the transport properties of TI materials. The calculation parameters are also discussed and presented.

Chapter 5 is devoted to the study of bulk Bi_2Te_3. The fabricated bulk samples, morphology, structure and transport properties are discussed. The comparison with the calculated theoretical properties is analysed. A good agreement is found which establishes that WIEN2k and BolzTraP describe properly the topological insulator Bi_2Te_3 family of materials.

Chapter 6 is dedicated to thin film topological insulator materials based on Sb_2Te_3. Their structural and morphological properties are characterised. The thin film transport

properties are extensively analysed to assess whether the topological surface state is re-alised experimentally. The calculated electronic and transport properties are compared with the experimental results and ultimately are used to demonstrate the topological sur-face state.

In Chapter 7, the coupling of the topological insulator thin films with magnetic mate-rials in the form of heterostructures is presented. An extensive study into their structural and morphological properties is performed. An insight into their transport properties and how they are altered with the presence of the magnetic layer is introduced.

To finalise, the main conclusions are given in Chapter 8, where future perspectives of this work are also presented.

Chapter 2

Topological Insulator Materials

Insulators are one state of matter best described by the simple band theory of solids. An insulator is a material with an energy gap between the occupied valence bands and the unoccupied conduction bands. A semiconductor is rather like an insulator, with the difference being the value of the energy gap, higher for insulators. All these properties of either insulators or semiconductors come from their Hamiltonian. Picturing a tuning of the Hamiltonian, with adiabatic continuity, without closing the band gap, we can transform an insulator into a semiconductor. This means that an insulator and a semiconductor are topological equivalents.

This correspondence can even be taken further. Vacuum is also a topological equivalent to an insulator, since the Dirac's relativistic quantum theory shows that a pair production is equivalent to an energy gap, electrons to a conduction band and positrons to a valance band [6]. However, this does not mean that all insulators are equivalent to the vacuum. If there is no adiabatic path connecting them, the connection between the insulator and the vacuum necessarily implies a phase transition, at which the gap disappears. Two insulators that fall into the last category are the Quantum Hall state and the Topological Insulators.

2.1   Quantum Hall Effect

In a two-dimensional material, placed in a strong magnetic field, the electrons have quantised circular orbits, with quantised energy levels, called Landau levels. With N Landau levels occupied, there is an energy gap between the filled and unoccupied energy levels. When applying an electric field, instead of behaving like a normal insulator, the circular

orbitals drift, which leads to a Hall current having a quantized Hall conductivity, given by 2.1.

$$\sigma_{xy} = Ne^2/h \tag{2.1}$$

The Landau levels can be viewed as the band structure of the 2D material. Due to the momentum components not commuting between each other in the presence of a magnetic field, no momentum k can be defined. If there is a unit cell with area hc/eB with a quantum flux through it, the lattice translations can commute and thus states can be categorized by a momentum k. In this case, the energy levels are constant with no k-dispersion. This is the case depicted in Figure 2.1, where a normal insulator state is compared to the quantum hall state, in terms of the motion of electrons, their band structure and their equivalent topological entities. If the material has a periodic potential, the band dispersion of a quantum Hall state will no longer be independent of the k value.

We are still left with the question of what is the difference between the quantum hall state and a normal insulator. The answer is topology and the Thouless, Kohmoto, Nightingale, and den Njis (TKNN) [7] invariant.
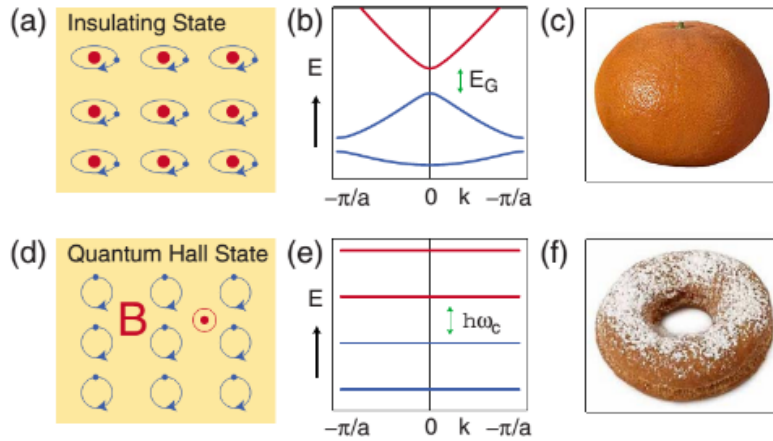
FIGURE 2.1: The insulating state vs. the quantum hall state: the motion of the electrons (a and d), the band structure (b and e) and the equivalent topological surfaces (c and f). Adapted from [6].

2.1.1 Topology and the TKNN invariant

Consider a mapping between two dimensions to three dimensions that defines surfaces. Each surface can be categorized by the genus, g, a mathematical entity that counts the number of holes on a surface. Imagine now an orange, a doughnut (Figure 2.1.c and d)

and a mug. They are completely different objects, but for topology there is only one thing that matters: the genus. With this, the orange has genus 0 and the doughnut has genus 1, like the mug. This means that the orange is not topologically equivalent to the doughnut but that the doughnut and mug are equivalent. They can be turned into one another by a continuous transformation. This is the same situation with normal insulators, vacuum and the Quantum Hall state: a normal insulator can be transformed adiabatically into vacuum, whereas the quantum Hall state is not equivalent to neither the vacuum or the normal insulator.

Now, topology defines a quantised topological invariant that is characteristic of the type of surface (the orange or doughnut) or insulator (the normal insulator or the quantum hall state). For surfaces, the topological invariant is the integral of the Gaussian curvature over the closed surface. This invariant is related to the genus of the surface. A similar topological invariant can be defined for insulators: the Chern number. The Chern number is defined as the total Berry flux in the Brillouin zone. The Berry flux is defined by equation 2.2, where A_m is the Berry phase and u_m are the Bloch wave functions [8]. The Chern number of the occupied band m is then given by equation 2.3.

$$F_m = \bigtriangledown \times A_m, A_m = \imath < u_m | \bigtriangledown_k | u_m > \tag{2.2}$$

A total Chern number, n, can be defined as the sum over the Chern numbers of all the occupied bands. Thouless, Kohmoto Nightingale and den Nijs, in 1982 [7], showed that N, the integer of the quantized conductivity in equation 2.1, is identical to the total Chern number.

$$n_m = \frac{1}{2\pi} \int d^2 \mathbf{k} F_m \tag{2.3}$$

2.2 $\mathbb{Z}_2$ Topological Insulators

Time reversal symmetry being broken is why the Quantum Hall state occurs. However, there is another away of achieving a new topological state of matter through strong orbit coupling [9]. To study the properties of the new topological state, the effect of the time reversal symmetry on particles like electrons with spin $\frac{1}{2}$ must be analysed.

Time reversal symmetry is described by an antiunitary operator Θ, which, for spin $\frac{1}{2}$ particles, has the property of $\Theta^2 = 1$. With this, a constrain is imposed on the system.

A time reversal Hamiltonian has the property described in equation 2.4. The Kramer's theorem dictates that the eigenstates of this Hamiltonian are twofold degenerate. If the system has no spin-orbit coupling, this degeneracy is just the spin up and down states. However, in a system with a spin-orbit interaction, this is changed.

$$\Theta H(\mathbf{k})\Theta^{-1} = H(-\mathbf{k}) \tag{2.4}$$

In this type of systems, one can study the type of Hamiltonians that can suffer an adiabatic transformation while keeping a band gap. The different classes of these Hamiltonians are characterized, as before, by topological invariants. One is the TKKN invariant, which has the value $n = 0$ in these systems, due to time reversal symmetry. The other one, ν, is a $\mathbb{Z}_2$ topological index thus having only the values 0 or 1 and their values can be understood through the bulk-boundary correspondence [10].

On the edges of a 2D insulating system, there can be states bound to the edge inside the gap or not. If there are bounded states inside the gap, Kramer's theorem requires that they are twofold degenerate, at certain special points that are time reversal invariant momenta ($k = 0$ or $\frac{\pi}{a}$). Moving away from these points, the spin orbit breaks this degeneracy and two different situations can occur. The special points can be connected pairwise which means they cross the Fermi energy an even number of times. If this is the case, the bound states can be pushed out of the gap eliminating the edge states. If the connections cross the Fermi level an odd number of times, the edges states cannot be eliminated. This is depicted in Figure 2.2, where the special points are marked as Γ_a and Γ_b.

The second topological invariant describes these two situations. The change in this topological invariant at an interface is equal to the number of Kramer's pairs that cross the fermi level, N_k, and it is thus given by equation 2.5.

$$N_k = \triangle \; \nu mod 2 \tag{2.5}$$

From this description, it can be concluded that a topological insulator is characterized by having topologically protected edge states, namely the states that cross the fermi level an odd number of times. With all this, a certain material can be considered as a possible topological insulator if the topological invariant is 1 and, thus, this invariant must be calculated.

There are several mathematical ways of achieving this. However, and considering the symmetries of the material being studied [11], the calculations can become easier. If the
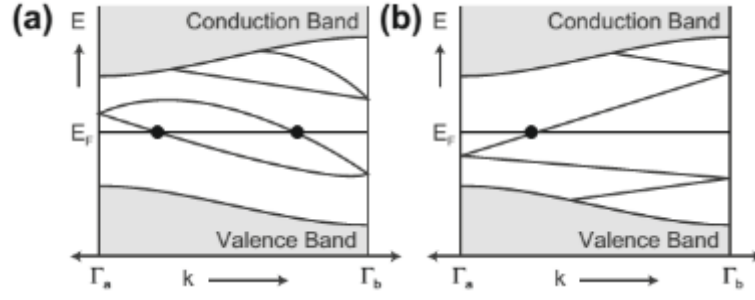
FIGURE 2.2: The electronic band structure between two boundary Kramers degenerate points, Γ_a and Γ_b. The number of crossings of the Fermi energy can be either even (a) or odd (b). Adapted from [2]

material at hand has inversion symmetry [12], there are four points where $\mathbf{k}$ and $-\mathbf{k}$ are coincident, in the 2D bulk Brillouin zone. At these special points, the Bloch states are parity eigenstates with an eigenvalue $\zeta_m(\Lambda_a) = \pm 1$, where m is an occupied band. From the eigenstates, the invariant can be calculated by equation 2.6, where $a = \{1, 2, 3, 4\}$ is one of the special points. Thus, a band structure calculation can unveil if a certain material is a topological insulator.

$$(-1)^\nu = \prod_{a=1}^{4} \delta_a \delta_a = \prod_m \xi(\Lambda_a) \tag{2.6}$$

So far, only 2D systems and thus 2D topological insulators have been discussed. Only in 2006 [13–15], the 3D topological insulator was theoretically predicted. The 3D topological insulators are characterized by 4 $(\nu_0; \nu_1, \nu_2, \nu_3)$ topological invariants instead of just one. With the same bulk-boundary correspondence principal used to obtain the properties of the band structure of the edge 2D TI, the 3D TI surface band structure can be studied.

The 2D Brillouin zone has 4 different special points with time reversal invariant momenta. This points form 2D Dirac points as in graphene [16]. As seen for the 2D TI, this points are Kramer's degenerates, whereas the other points, due to the spin orbit coupling, are not degenerate. There is thus two ways of connecting each one of the special points to one another. If the number of crossings of the Fermi level is even, the material is a normal insulator, while a TI has an odd number of crossings, making this states topologically protected. These two ways of connecting the special points are determined by the 3D four $\mathbb{Z}_2$ invariants.

Having this description, a study of the topological invariants must be made. The first invariant, ν_0, can take two values. Each one corresponds to the two types of 3D topological

insulators: weak and strong. The weak topological insulator can be achieved by stacking layers of a 2D topological insulator. It has $\nu_0 = 0$ while the other indices can be interpreted has the Miller indices of the orientation of the layers. The surface states of this type of 3D TI's are, however, not protected by time reversal symmetry. Although the individual edge states are present, if there is disorder, the surface states can be localized, which justifies the name weak TI.

The strong TI, on the opposite end, has protected surface states and $\nu_0 = 1$. The meaning of ν_0 can be understood as the parameter that defines if the surface Fermi circle encloses either an even $\nu_0 = 0$) or an odd ($\nu_0 = 1$) number of Kramer's points. Thus, in a strong TI only an odd number of the degenerate special points is inside the Fermi surface. The strong TI has thus a 2D topologically protected metallic surface with an electronic structure like graphene, but with only one Dirac point, with the partner Dirac point residing on the opposite surface, thus still obeying the fermion doubling theorem [17]. However, the metallic 2D surface is not like a normal metal, since there is not a degeneracy between spin up and down. The time reversal symmetry implies that states at opposite momenta must have opposite spins. With this, the spin rotates around the Fermi surface.

The main difference between the weak and strong TI is that the electrons cannot be localized on the surface even with strong disorder, with the only requirement being that the bulk stays gapless. The only way to break the protection of the surface states is by breaking the time reversal symmetry, which can be accomplished by using either a magnetic field or magnetic materials and impurities.

2.3 2D Topological Insulators: the quantum wells

As seen in the previous section, it is the spin orbit coupling that causes the topological insulator properties. Due to this, the first materials where topological effects were expected where materials made from heavy elements near the bottom of the periodic table with strong spin orbit coupling. With this, in 2006, Bernevug, Hughes and Zhang [18] presented the idea that HgCdTe quantum wells could be the first 2D topological insulator, also known as the quantum spin Hall insulators.

They studied a structure of a layer of HgTe between two layers of CdTe. With this structure, they obtained a quantum phase transition from a normal insulator to a topological insulator, based on the band inversion of HgTe and the different parity of the occupied

bands, as seen previously. This occurs when the thickness of the layer of HgTe is changed. If the thickness is smaller than a certain value d_c, the bounded 2D electronic states have a normal band order. If the thickness increases for values higher than the critical thickness, the bands invert and the state is that of a 2D topological insulator. All this is explained by considering the band structure of HgTe, constituted by a s-like symmetric conduction band and a p-like valence band and under the approximation that the system has inversion symmetry. This also implies that at the critical thickness, the energy gap closes and that the $\mathbb{Z}_2$ invariant changes from 0 to 1 in the phase transition.

After one year, their theoretical proposal was obtained experimentally by Molenkamp and colleagues [19]. They studied the transport properties of the quantum well structure, namely the electrical resistance of the edge states. They obtained the results presented in Figure 2.3, where the resistance of 3 HgTe quantum wells and their structure is presented, evidencing the integer conductivity. Sample I that has a thickness smaller than the critical thickness does not have a quantized conductivity, whereas the other samples, with thicknesses larger than the critical value, have the integer conductivity. It is also verified that the transport was in the edge of the quantum well, since Sample III and IV have different widths, but the same length and thus the same conductivity.
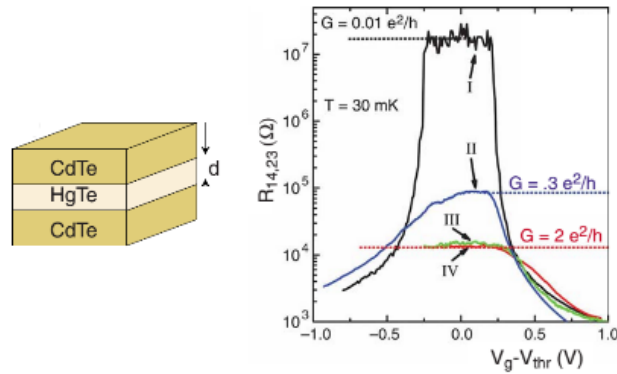
FIGURE 2.3: Quantum well structure and the resistivity of 4 samples as a function of the gate voltage. Sample I has a thickness smaller than the critical thickness and the other samples the same thickness value higher than the critical thickness, with different widths. The characteristic qauntised conductivity is observed, evidencing the topological edge state. Adapted from [19].

2.4   3D Topological Insulators: Bi_xSb_{1-x} and the Bi_2Te_3 family

The first 3D topological insulator to be discovered was the bismuth antimony alloy Bi_xSb_{1-x}. It was discovered in 2008 [20] by an Angle resolved Photoemission Spectroscopy (ARPES)

experiment, with which the exotic band structure was obtained.

Besides being a 3D topological insulator, these compounds are also good thermoelectric materials, having mostly been studied for their thermoelectric properties [21, 22]. Furthermore, Bismuth and Antimony are both semimetals with a finite direct band gap.

Bismuth has the band structure as well as the Brillouin zone represented in Figue 2.4. At the L point in the Brillouin zone, the valence band is antisymmetric, the conduction band is symmetric and there is a small gap. These bands can be described by the Dirac equation with a small mass. When the amount of antimony in the alloy increases, the band gap present in the band structure of bismuth starts to decrease, until the concentration $x = 0.04$. At this point, the bands touch and a 3D massless Dirac point is realized. For values of the concentration higher than this value and smaller than 0.09, the gap reopens and the alloy becomes an insulator. For even more increasing values, the material starts to be a semimetal as before.
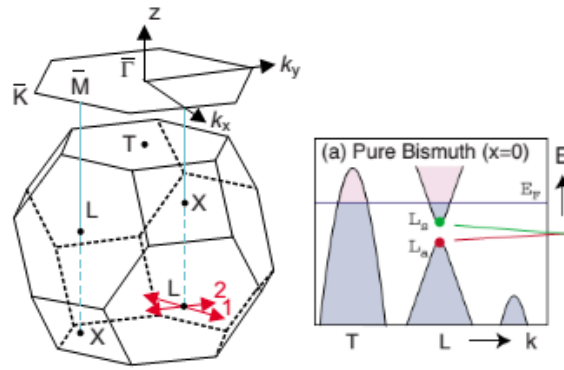
FIGURE 2.4: The Bismuth Brillouin zone and its band structure. Adapted from [6, 20]

Moreover, these alloys have inversion symmetry. With this, the topological invariants can be obtained by band structure calculations, as seen in the previous section. Fu and Kane [12] performed these calculations and obtained the parity and thus the invariants for the occupied Bloch states at the eight time reversal invariant points of the Brillouin zone. With this, they predicted that the alloy would have the topological invariants equal to (1; 111) and 5 Dirac points.

With ARPES experiments, several topological properties were obtained [20, 23, 24] The first one is the band structure of the material, which, as seen before, is extremely important as an insight into if a material is a TI and its properties. Furthermore, if it is carried out in a spin resolution mode, the spin polarization of the bands can be obtained, and the spin locking phenomena can thus be verified. In Figure 2.5, the surface state of

$Bi_{0.92}Sb_{0.08}$ obtained with spin-ARPES is presented, showing the spin texture expected for a TI.
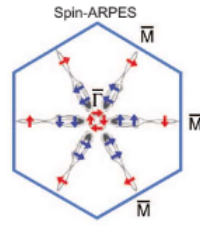
FIGURE 2.5: $Bi_x Sb_{1-x}$ Surface state at the Fermi level obtained with spin-ARPES, evidencing the spin texture with arrows.

After the $Bi_x Sb_{1-x}$ alloy was discovered as a topological insulator, a new family of materials was discovered as being also TI's: the $Bi_2 Te_3$ family. These materials are also one of the best available thermoelectric materials [21] and after ARPES measurements combined with first principle calculations, their topological insulator properties came to light [25–27].

They are characterized by having $(1; 000)$ as the four topological invariants. Moreover, they only have one almost ideal Dirac cone and thus only on Dirac point. With this, some differences form the alloy $Bi_x Sb_{1-x}$ can already be seen. Beside the single Dirac point, their band gap is larger. This has an extreme importance since the materials can exhibit their topological properties at room temperature, opening room for a wide range of applications. They are also pure materials instead of an alloy, which means that they can be prepared with higher purity, improving the accuracy of the experimental studies and theoretical calculations.

These materials were studied using the same techniques as $Bi_x Sb_{1-x}$. In Figure 2.6, the band structure of $Bi_2 Se_3$, obtained experimentally by ARPES, is presented as well as its fermi surface, evidencing the spin polarization. $Bi_2 Te_3$ and $Sb_2 Te_3$ do not have such a simple dirac cone due to a smaller band gap and to the lattice potential [6]. For the case of $Bi_2 Te_3$ and $Sb_2 Te_3$, their band gap is smaller and Dirac cone is not as simple as for $Bi_2 Se_3$. However, they are still two of the most studied materials, either for their TI or thermoelectric properties.
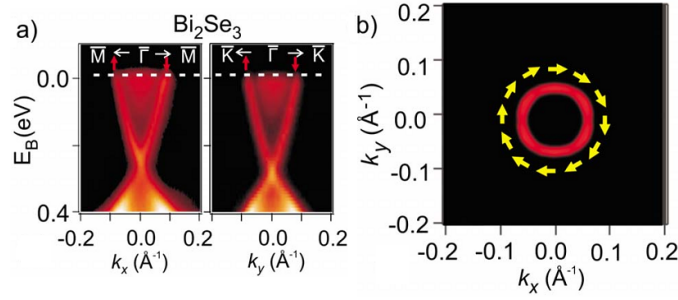
FIGURE 2.6: Bi_2Se_3 band structure and Fermi surface obtained by ARPES. Adapted from
[6]

2.5 Experimental Signatures

The properties of 3D topological insulators are studied using a variety of experimental techniques. Although the predicted theoretical behaviour is rather simple, the experimental verification of such a behaviour is not as simple for the Bi_2Te_3 and Sb_2Te_3 3D TI's. Furthermore, measurement of the transport properties of the topological surface state remains a challenge, since these materials can have extremely high bulk contributions.

Several techniques are used and developed to verify the expected signatures of the topological behaviour and to study its properties. In this section, a brief overview of some of the latest experimental results that demonstrate this behaviour is going to be presented.

2.5.1 ARPES - Angle Resolved Photoemission Spectroscopy

Angle Resolved Photoemission Spectroscopy is a technique that allows for the direct study of the electronic band structure [28]. Since one of the key features of the 3D topological insulators is the Dirac cone of the surface state, ARPES is the go to technique to verify if a certain material is a TI. It was the technique used to discover the Bi_2Te_3 family as topological insulators as described in the previous section.

Chen et al. [29] published in 2009 a deep study into the possibility of Bi_2Te_3 being a 3D topological insulator based on ARPES studies. Figure 2.12 shows the band structure obtained from ARPES measurements along K-Γ-K and M-Γ-M. The Dirac point is signalled as well as the surface state. One sees that it forms a Dirac cone with a broadening at higher energies. It is thus not as ideal as in graphene [16, 30] or Bi_2Se_3 (Figure 2.11) [6, 26, 31]. Sb_2Te_3 has also been deeply studied to verify if it has the surface topological state [32]. Figure 2.8 shows an ARPES measurement performed in a 30 nm Sb_2Te_3 thin film. The

Dirac point and cone are evidenced but by comparing with the Bi_2Te_3 band structure, one sees that Sb_2Te_3 Dirac cone is not as ideal.
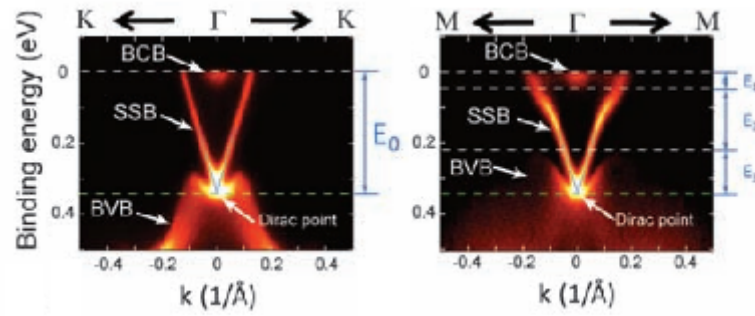
FIGURE 2.7: Bi_2Te_3 Band structure obtained from ARPES measurements. The apex of the V-shape dispersion is the Dirac point. Adapted from [29]
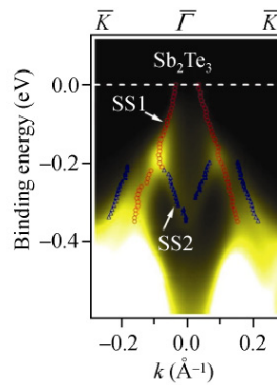
FIGURE 2.8: Sb_2Te_3 Band structure obtained from ARPES measurements. Adapted from [32]

The Fermi surface can also be obtained from an ARPES measurement [29]. Figure 2.9 shows the Fermi surface obtained for different incident photon energies. The outer surface does not vary, which is indicative of its origin being the surface state. On the opposite, the inner shape has a wide change with the photon energy. This means that it is dependent on k_z, which is compatible with the bulk states.
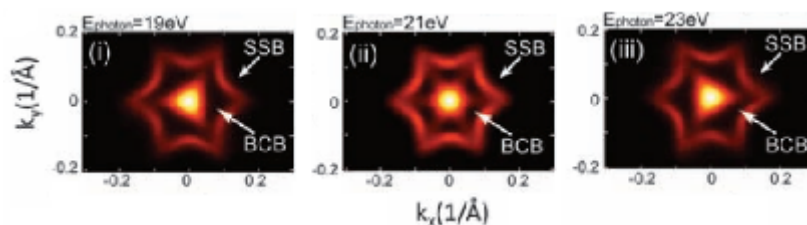
FIGURE 2.9: Maps of the Bi_2Te_3 Fermi surface as a function of the incident photon energy. Adapted from [32]

ARPES can also be used to study the spin polarization of the band structure. By performing spin-ARPES measurement, the spin locking phenomena characteristic of the topologically protected surface states can be observed. Several groups have performed spin studies, either experimental through spin-ARPES or theoretical [31, 33]. Souma et al. combined both and the results are presented in Figure 2.10, where a schematic picture of the spin z component obtained with spin-ARPES is presented as a function of k of the surface state of Bi$_2$Te$_3$ [34]. One sees a clear spin texture of the protected surface state.
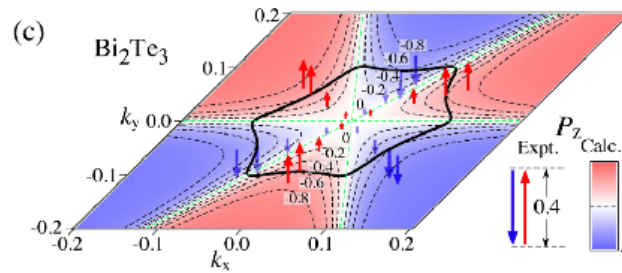
FIGURE 2.10: Schematic picture of the Bi$_2$Te$_3$ spin z component as a function of k in the surface state, obtained with ARPES. Adapted from [34]

2.5.2 Seebeck Coefficient and Magneto Thermopower

The Bi$_2$Te$_3$ family, as seen in the previous section, is a family of thermoelectric materials. Thus, their thermoelectric properties, namely the Seebeck coefficient or Thermopower, must be studied.

Bulk Bi$_2$Te$_3$ has a Seebeck coefficient of around -120 μ V/K [35] at room temperature, which varies with temperature and dopant concentration. In thin films of Bi$_2$Te$_3$, the coefficient can have a different behaviour. In Figure 2.11, Rogacheva et. al [36] studies of the Seebeck coefficient as a function of thin film thickness of Bi$_2$Te$_3$ thin films grown on glass substrates by thermal evaporation is presented. They showed with these results that the Seebeck coefficient oscillates with the thickness in the interval 18-100 nm, having a substantial amplitude and a constant period. They also suggest that this oscillation occurs due to the topological protected surface states.

Another interesting property of Bi$_2$Te$_3$ thin films studied is the magneto thermopower. Several oscillations compatible with the Shubnikov-de Haas effect are reported by Qu et al. [37]. In Figure 2.12, the thermopower following typical representation on TI studies is plotted as a function of the inverse of the magnetic field to detect the small high magnetic field oscillations. These measurements are a good probe of topological surface states in 3D materials, since in the samples studied, the bulk carriers have opposite signs and
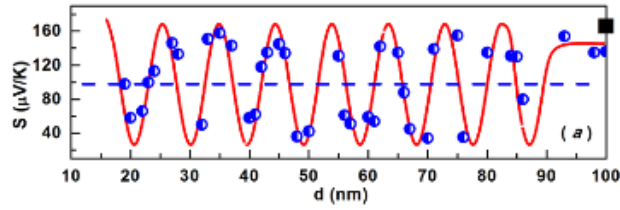
FIGURE 2.11: Seebeck coefficient as a function of the Bi$_2$Te$_3$ thin film thickness at room temperature.

thus make the bulk thermopower almost negligible. Thus, the results presented were a direct measurement of the surfaces states thermopower and thus of the properties of the topological states.
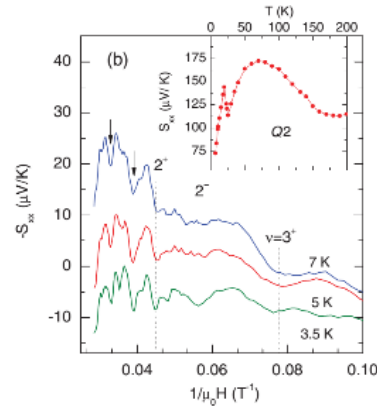
FIGURE 2.12: Thermopower as a function of the inverse of the magnetic field with an inset of the temperature dependence of the thermopower. Adapted from [37].

2.5.3 Resistance and Magnetoresistance

A resistivity measurement is essential for any complete transport properties characterisation. From the resistivity, we can study the type of behaviour of the material. As for the thermopower, the resistivity also has a temperature dependence. In Figure 2.13, the results Le et al. [38] obtained of the resistivity for several Bi$_2$Te$_3$ thin films are plotted against the temperature. It is visible that the resistivity increases with a decrease in the thin film thickness, while increasing with temperature. This is characteristic of metallic behaviour, common in small gap intrinsic semiconductors. However, for temperature smaller than 10K, specially for the smaller thicknesses, the resistivity slightly increases, indicative of an enhancement of the electron-electron disorder.

The magnetoresistance is also a key experimental study for demonstrating the topological insulator behaviour.
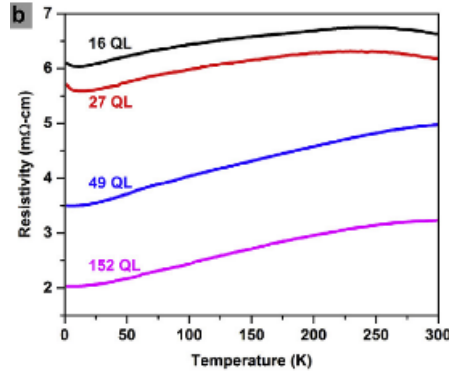
FɪɢᴜʀE 2.13: Resistivity as a function of the temperature for 4 Bi_2Te_3 thin films with different thicknesses (QL≈1nm). Adapted from [38]

At low magnetic fields, the weak antilocalisation effect is a consequence of the topological surface state characteristics [39–41]. Due to the strong spin orbit effect and to the spin polarisation of the surface state, weak antilocalisation is visible at low magnetic fields, especially for thin films with smaller thicknesses. Using the Hikami-Larkin-Nagaoka model [42, 43], the magnetoresistance is given by equation 2.7, with Ψ the digamma function, B_ϕ a magnetic field characterized by the coherence length L_ϕ and α a parameter indicative of the number of conduction channels. In a 3D TI surface, alpha is -0.5 if there is only one coherent transport channel, and it is -1 if there are two independent coherent transport channels with similar coherence length. In Figure 10, the magnetoresistance of 4 Bi_2Te_3 different thin films is presented, as well as a theoretical fit using equation 2.7. The obtained values for α are consistent with a single transport channel for 16 to 49 QL and two independent transport channels for 152 QL.

$$\frac{\Delta R(B)}{[R(0)]^2} = -\alpha \frac{e^2}{2\pi^2 h} \left[\Psi \left(\frac{1}{2} + \frac{B_\phi}{B} \right) - ln \left(\frac{B_\phi}{B} \right) \right] \qquad (2.7)$$

At high magnetic fields, the Magnetoresistance also presents the Shubnikov-de Haas oscillations [44]. As for the magnetothermopower, these oscillations are a probe into the topological surface state, since even in materials with high bulk contribution to the conductivity, as it is the case of the Bi_2Te_3 family, the high mobility of the topological surface state allows the SdH oscillations signal to still be observable [45–47]. By studying the Landau level fan diagram obtained from the SdH oscialltions, the topological surface state can then be assessed. Figure 2.15 shows the SdH osciallations obtained for Bi_2Te_3 at high magnetic fields. These oscillations have also been recently observed for Sb_2Te_3, evidencing its topological insulator behaviour [48].
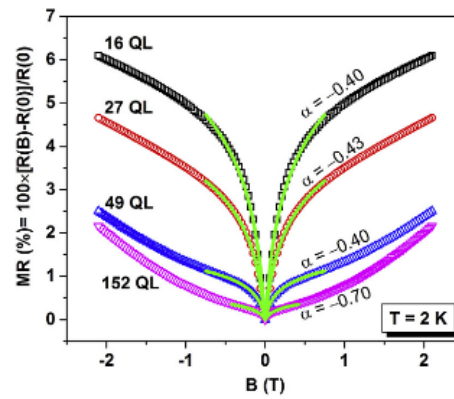
FIGURE 2.14: Magnetoresistance for several Bi_2Te_3 thin film thicknesses measured at 2K. The green lines are the theoretical prediction given by equation 2.7. Adapted from [38]
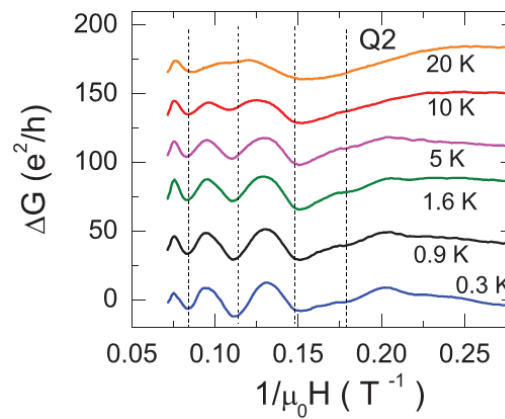
FIGURE 2.15: Magnetoconductance as a function of the inverse of the magnetic field for a cleaved Bi_2Te_3 crystal. The Shubinkov-de Haas oscillations at high magnetic fields are observed. Adapted from [47].

Chapter 3

Experimental Techniques

In this chapter, the various experimental techniques performed throughout this work are going to be described. The fabrication techniques used are going to be covered, specially the thin film deposition technique Ion Beam Sputtering Deposition. The morphological and structural characterisation of the samples is explained, as well as the various transport properties measurements carried out on the fabricated samples.

3.1 Sample Fabrication

Two different kinds of samples were prepared: bulk materials and thin films. Different techniques are used to produce each set of samples; bulk synthesis and thin film deposition.

3.1.1 Bulk synthesis

Bulk Bi_2Te_3 was fabricated using a solid state reaction consisting of the mix of two pure precursors. Commercial high-purity powders of 99.5% Bi (Alfa Aesar under 325 mesh) and 99.8% Te (Acros Organics under 200 mesh) were used as raw materials without further purification and are represented in Figure 3.1. The powders with a stoichiometry of Bi_2Te_3 were weighed, and then mixed uniformly in an agate mortar in air. The mixed powders were pressed into a pellet using steel die in air with 1.3 cm of diameter and 4000 Psi for 60 seconds. Then, three pellets were then introduced into the quartz tube with just one opening which is connected to a diffusion pump and N2 (with a DN25KF connection). Several purges were performed with the aim to avoid oxidation and after the quartz ampoule was sealed with a Bench Burner fuelled with a combination of hydrogen

21

and oxygen gases as seen in Figure 3.1. The tube was then placed inside the oven and subjected to the thermal treatment that it is depicted on Figure 3.2.
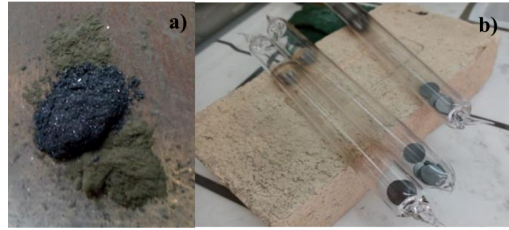
FIGURE 3.1: Synthesis of bulk Bi_2Te_3. a) Initial powders of Bi and Te commercial precursors and b) Bi_2Te_3 pellets inserted in the sealed quartz tube.

First the sample was heated up to 720 ºC at a rate of 5.14 ºC min^{-1}, where it rested for 5 hours. After, it was slowly cooled to 560 ºC at 0.12 ºC min^{-1}. After this point the furnace was turned off and the sample was cooled until room temperature is reached.
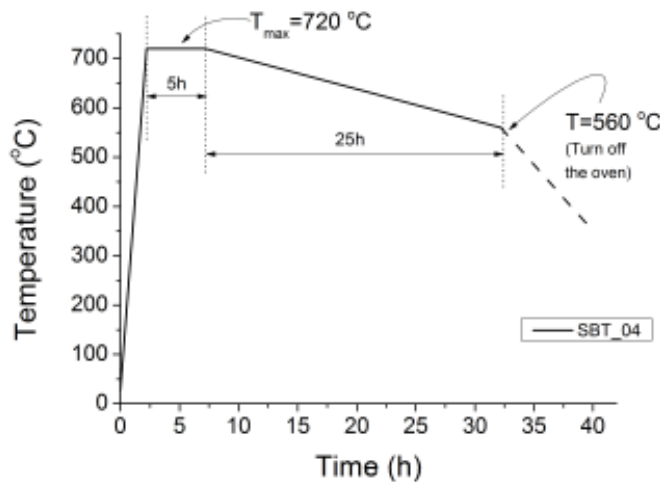
FIGURE 3.2: Thermal treatment performed in the Bi_2Te_3 bulk synthesis.

3.1.2 Ion Beam Sputtering Deposition

Ion Beam Sputtering Deposition (IBD) was used to deposit the thin films studied throughout this work. The samples were produced at the Ion Beam Sputtering Deposition from Commonwealth Scientific Corporation at the clean room of Centro de Materiais da Universidade do Porto (CEMUP).

Ion Beam sputtering deposition is a top-down deposition technique for the fabrication of nanostructures, namely thin films. Figure 3.3 presents a schematic representation of the

ion beam deposition chamber that exists at CEMUP. The basic IBD is constituted by a vacuum system, an ion gun, a target, a substrate holder and a shutter. With this configuration, only conductive thin films can be deposited. However, at Porto, due to the existence of a neutralizer and the assist ion source, oxide materials can also be deposited. The deposition occurs as follows: the argon (Ar) gas is ionised through electron ionization. The Ar ions are then accelerated towards the target of the intended material to be deposited. The target is constantly rotating to avoid nonuniformities in the deposition. With the impact of the ions on the target, material is removed and it is directed towards the substrates held at the substrate holder, which is also always rotating for a greater uniformity of the thin films.
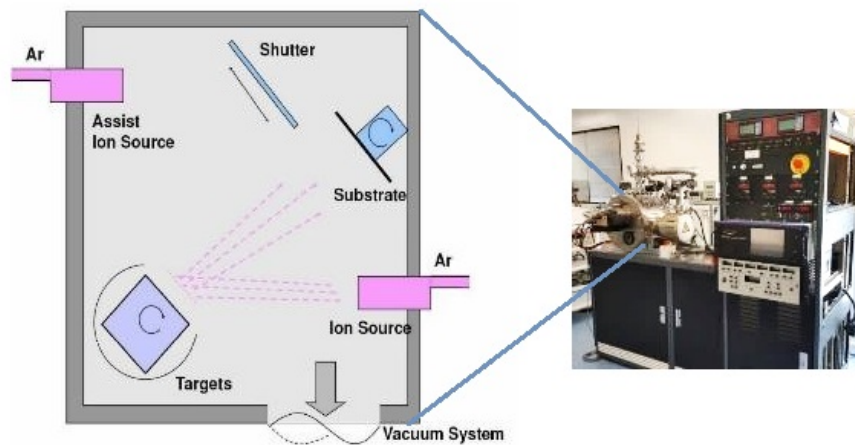
FIGURE 3.3: Schematic representation of the Ion Beam sputtering deposition chamber and the ion beam sputtering deposition system at CEMUP.

Several deposition parameters exist and are monitored prior to and during the deposition. These parameters are: the base pressure, the working pressure, the beam voltage and the discharge current. The base pressure measures how good is the vacuum of the chamber. The working pressure controls the quantity of argon in the chamber and thus the number of ions hitting the target. The discharge current controls the electron ionisation procedure and the beam voltage controls the energy of the impacting ions on the target and, ultimately, the energy of the material removed from the target to be deposited on the substrates. All these controlled parameters allow Ion Beam Deposition to be a fabrication technique producing thin films with the intended stoichiometry and good morphology. Furthermore, being a top-down technique, cheaper than other commonly used techniques, such as Molecular Beam Epitaxy, it is very accessible and industrialised.

Two different materials were deposited throughout this work: antimony telluride (Sb_2Te_3) and a permalloy of nickel and iron ($Ni_{0.15}Fe_{0.85}$). The Sb_2Te_3 target was a commercial target acquired at Semiconductor Wafer, Inc. All the targets had a size $3'' \times 3$ mm. With these materials, several thin films and heterostructures were fabricated throughout this dissertation.

The depositions occurred at room temperature in two different rigid substrates: silicon and glass (fused silica). Prior to the deposition, the substrates were rigorously cleaned [49]. The silicon substrates were cleaned by a five minutes ultrasonic bath of acetone followed by a five minutes ultrasonic bath of isopropanol. Following the baths, they were dried under nitrogen airflow and in a hot plate at 110ºC for roughly 10 minutes. The glass substrates were cleaned in a similar way: three five minutes ultrasonic baths of acetone, isopropanol and deionised water, in this order, followed by drying under nitrogen airflow. The depositions were performed at a working pressure of 1.4×10^{-4} Torr and a discharge current of 2.00 A. The base pressure prior to the depositions was always between 2×10^{-7} and 1.4×10^{-7} Torr. In Table 3.1, a list of the different beam voltages and deposition times of the several thin films fabricated is presented.

3.2 Morphological and Structural Characterisation

with the bulk and thin film samples fabricated, several characterisations were performed of their structure and morphology.

3.2.1 Thickness Measurement

The thickness of the thin films was primarily measured using the profilometer at the CEMUP clean room. The profilometer was a DektakXTTM produced by Bruker. A profilometer uses a cantilever with a diamond tip that touches and scans the structure to be analysed. By measuring the deflection of the cantilever, the relative heights of figures on the structure can be obtained. Thickness of thin films is then measured by scanning the film at its border, from a region with only substrate to substrate and thin film.

Every thin film was measured at least 8 times on different regions in order to verify uniformity and to have good statistics for a reliable measurement. The obtained values for the measured thin films are presented in 3.1.
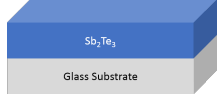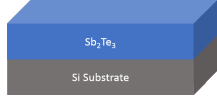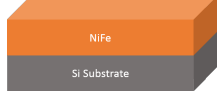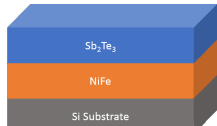
Material	Nanostructure	Substrate	Beam Voltage (V)	Intended thickness (nm)	Deposition Time (min)
Sb_2Te_3		Glass	700	10 50 100 400	1 4 8 32
		Si	700	10 50 100 400	2 4 10 32
NiFe		Glass	1000	100	33
		Si	1000	100	33
$NiFe/Sb_2Te_3$		Glass	1000/700	10/100 100/10 50/50 100/100	3/10 33/1 16.5/6 33/10
		Si	1000/700	10/100 100/10 50/50 100/100	3/10 33/1 16.5/6 33/10

TABLE 3.1: Deposition parameters of the fabricated nanostructures.

3.2.2 Scanning Electron Microscopy SEM

To obtain information about the microstructure of the thin films, Scanning Electron Microscopy (SEM) was used. The SEM system used was a PhilipsFEI/Quanta 400 at CEMUP.

SEM is a microscopy technique where the sample surface is irradiated by a beam of electrons. These electrons have a high energy of the order of 20-30KV. They are focused by a set of magnetic lenses that also allow the beam to be moved across the surface, row by row, in order to form a full image of the sample's surface. This is possible due to the high energy electron beam interaction with the sample. The electrons upon hitting the surface's sample, interact with it, and several electrons and photons are emitted by the sample. The intensity of the primary electrons at each interaction spot is used to form the full image of the sample. However, several other types of electrons are also emitted. Secondary

electrons, which are produced by the inelastic interactions with the sample's electrons, are used to form 3D images of the surface due to their low energy being intimately related to the interaction depth. The backscattered electrons are the beam electrons that experience elastic backscattering with the sample electrons or nuclei. With this, a contrast effect is formed based on the mean atomic number of the spot, which is related to the number of backscattered electrons. The larger the atomic number, the brighter the image of the spot will be [50].

SEM can yield images with a resolution of up to 50 nm. In this work, a maximum resolution of 500 nm was used.

3.2.3   Electron dispersive X-ray spectroscopy EDS

In order to obtain the chemical composition of the thin films, Electron dispersive X-ray spectroscopy (EDS) was used. The system was a EDAX Genesis X4M existing at CEMUP.

EDS is a technique that consist of irradiating the samples with a high-energy focused electron beam on a selected region of the sample surface. This electron beam removes core electrons from the atomic electronic shell, leaving a hole behind. In order to return to the ground state, electrons from upper states decay to fill the hole, emitting a photon during the process. The energy of this photon is a unique characteristic of every atom and, thus, by analysing the energy of the emitted photons and the quantity of each photon, the mass and atomic percentage of each element can be known. With this, the chemical composition of the sample is obtained. It is, specially, a powerful technique to study alloys.

3.2.4   X-Ray diffraction XRD

X-ray diffraction (XRD) measurements were performed on the bulk powder and nanostrcutures at room temperature to characterise their structure. A SmartLab Rigaku diffractometer at IFIMUP was used with a Bragg-Brentano $\theta/2\theta$ configuration, with a range of 2θ from 10º to 100º. The Cu Kα radiation with a wavelength of $\lambda = 1.540593\mathring{A}$ was used. The system operates at a 9 kW power, 45 kV and 200 mA.

3.2.5   X-Ray reflectivity XRR

To further characterise the structure of the thin films and the heterostructures, measurements of the small angle x-ray reflectivity (XRR) were performed. The system was the

SmartLab Rigaku at IFIMUP, with a parallel beam configuration. The Cu Kα was the used radiation, with a wavelength of $\lambda = 1.540593\mathring{A}$. The 2$\theta$ range was from 0º to 8º.

XRR allows to further characterise the structure of thin films and, more specially, thin films heterostructures. When an X-ray beam is incident on a sample surface at extremely small angles, it does not penetrate the film and it is totally reflected. Up to a critical angle θ_C, the detected intensity is maximum and approximately constant, being a plateau on the reflectivity curve. For angles higher than the critical angle, the x-ray beam penetrates the thin film surface and the intensity of the reflected wave decreases drastically, by what it is called Fresnel reflectivity. Due to the interference of the waves reflected at the air/thin film interface and film/substrate or film/film interfaces, several oscillations are also observed in the reflectivity spectrum. These oscillations are called the Kiessig fringes and by analysing them, the thickness of the thin film or layers of heterostructures is obtained. Figure 3.4 presents a typical spectrum of a single substrate, with the characteristic behaviour of the Fresnel reflectivity and the usual Kiessig fringes for a single thin film on the substrate. The total thickness can be obtained from equation 3.1 [51], where m is the order of the fringes, θ_m the angle of the maximum of the mth fringe and t the total thickness. By plotting the order of the fringes as a function of $\sqrt{\cos(\theta_C) - \cos(\theta_m)}$ and performing a linear fit, the total thickness can be obtained.
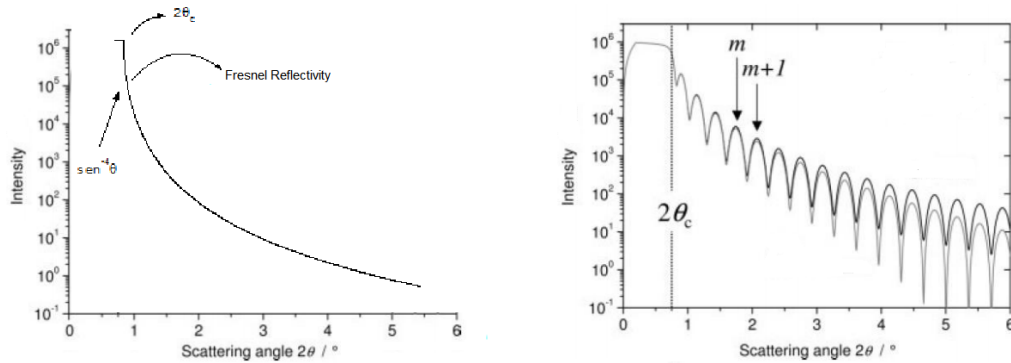
FIGURE 3.4: Example of a X-ray reflectivity curve for a substrate and for a thin film deposited on a substrate. Adapted from [52].

$$m = -\frac{1}{2} + \frac{2t}{\lambda}\sqrt{\cos(\theta_C) - \cos(\theta_m)} \qquad (3.1)$$

3.3 Transport Properties

Several transport properties of the fabricated materials were studied in this work. Besides the analysis of the surface state, they give great insights into the overall transport phenomena of these materials.

3.3.1 Electrical Resistivity

The electrical resistivity was measured as a function of temperature using a closed cycle cryostat. The maximum temperature range was $7 - 310K$. All the resistivity measurements were carried out at IFIMUP. In Figure 3.5, the experimental setup is presented, showing all the important elements for a proper electrical resistivity measurement and an assembled sample.
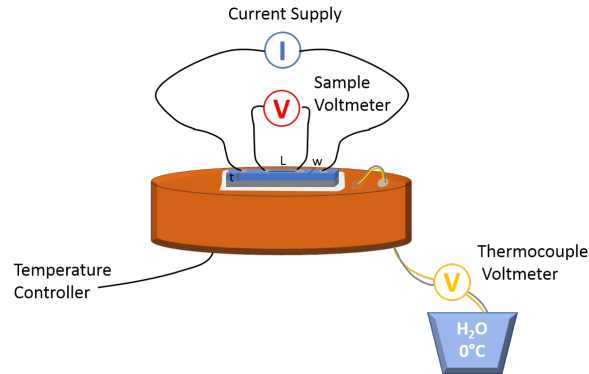
FIGURE 3.5: Experimental assembly for electrical resistivity measurements using the 4-probe technique.

To perform the measurements, a cylindrical Cu block acted as a sample holder. This block could be mounted on the cryostat. The sample is placed on its surface. In order to isolate the sample but still maintain a good thermal conductance with the cylindrical block, a thin leaf of shroud paper embedded in GE-varnish is placed between the sample and the surface of the block. The varnish is also used to glue the sample to the block.

The electrical measurements are performed with the standard 4 linear contacts. Four wires are inserted into the metallic sample holder. The two outer most wires are used to feed current (I) to the sample, while the inner most wires are used to measure the voltage (V), as shown in Figure 3.5. The electrical contact between these four wires and the sample is performed using a silver paste. In order to ensure a stable measurement throughout all temperatures, for some samples, 4 linear gold contacts were sputtered on to the surface

and then the silver ink was used to make the electrical contact between the sputtered contacts and the 4 wires.

The temperature control is performed using a Lakeshore 331 coupled with a diode sensor inserted at the cryostat. With this controller, the linear time rate of the temperature can be settled. Having defined the rate, the temperature controller automatically sets the PI parameters in order to have a linear temperature variation at the intended rate. The used rate was 0.5 K/min to ensure thermal equilibrium and to have the accuracy needed for these measurements [53].

For a reliable temperature measurement, a differential thermocouple is also placed at the sample holder block, near the sample. The voltage drop across this thermocouple, using as reference 0°C (ice), is measured with the assistance of a nanovoltmeter (Keithley 2182 or HP 314420). A prior calibration of the thermocouple curve is used to obtain the sample holder block temperature, which is considered to be the same temperature of the sample, due to the ensured good thermal conduction referred previously.

In order to perform the measurements automatically, a LabView routine was used. The temperature was controlled and the measured data could be monitored graphically in real time. The resistivity was calculated using equation 3.2, where R is the measured resistance, given by $\frac{V}{I}$ with V the measured voltage and I the constant applied current, w the width of the sample, L the distance between the voltage contacts and t the thickness of the material.

$$\rho = \frac{Rwt}{L} = \frac{V}{I}\frac{wt}{L} \tag{3.2}$$

3.3.2 MagnetoResistance

To verify the characteristic effects of the topological insulator state at high magnetic fields, the magnetoresistance was measured at Centro de Ciências e Tecnologias Nucleares (C2TN). The measurements are performed in a cryostat with 4He flow which allows a temperature range from 1.6 K up to 300 K and a magnetic field up to 18 T.

The resistance is measured using the standard 4 probe technique. Four linear gold contacts were sputtered on the sample to allow for the current supply and voltage measurement to be performed.

The magnetoresistance was measured at 4 different low temperatures, 2, 4.2, 10 and 20 K and for positive fields up to 16 T. Using a rotating sample holder fabricated at the Nuclear and Technological Campus (CTN), measurements in a longitudinal, with the magnetic field applied in the direction of the applied current, and a transversal configuration, with the magnetic field perpendicular to the thin film, were performed.

3.3.3   Seebeck

To measure the Seebeck coefficient at room temperature a homemade setup was used. A schematic diagram of the setup is presented in Figure 3.6. Two isolated Cu support towers constitute the setup. One tower is connected to a temperature controller (Lakeshore 331) that acts as the heat source, while the other tower is maintained at room temperature. With this, a temperature difference is applied to the samples. In order to obtain the temperature difference, a differential thermocouple of type K is connected to the towers and to the temperature controller.
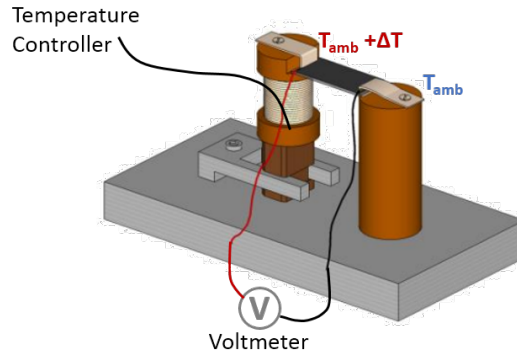
FIGURE 3.6: Experimental setup for measurements of the Seebeck coefficient at room temperature. Adapted from [54]

By varying the temperature difference ΔT and measuring the voltage across the thin film ΔV, the value of the Seebeck coefficient can be calculated using equation 3.3.

$$\Delta V = -S\Delta T \tag{3.3}$$

3.3.4   Magnetic Susceptibility

Magnetic susceptibility measurements were performed using a Magnetic Properties Multiphysics System (MPMS) also known as Quantum Design Superconducting Quantum Interference Device (SQUID) magnetometer at IFIMUP.

The magnetometer has a 10^{-7} emu sensitivity which can be increased by a factor of 100 since it possesses the Reciprocating Sample Option (RSO). The maximum field is 5.5T . The SQUID is constituted by a superconducting magnet in a helium bath and a magnet control system. Magnetisation measurements can be performed for temperatures within 1.7 and 380 K.

The magnetisation as a function of temperature M vs.T was obtained for low applied magnetic fields (1000 Oe) and temperatures between 5 and 370 K. From this measurement, the magnetic susceptibility was obtained following equation 3.4. Furthermore, the magnetisation as a function of the applied fields M vs.H at constant temperatures was also measured at 5 K and 300 K. This allowed to verify the type of magnetism of the samples.

$$\chi(m^3/mol) = \frac{4\pi10^{-3}}{10^3} \frac{M(emu)}{H(Oe)} \frac{M(g/mol)}{m(g)} \tag{3.4}$$

Chapter 4

First Principle Calculations

First principle calculations are a key tool in the study of solids. Analytical methods are not feasible but a deep knowledge of a certain materials electronic properties is still required. With this, various physicists work on developing new software packages based on several approximations.

A solid is made of nuclei, which are positively charged particles, and electrons, which as we know are negative charged particles. They can be described by the simple Hamiltonian given by equation 4.1, where the sum is over all the nuclei and electrons in the solid, which amounts to $N + ZN$ particles, with P the momentum, M the mass, q the charge and $\mathbf{R}$ the position. Although it can be written in a very simple manner, it is not possible to solve this Hamiltonian exactly for real solids. Due to this, numerical methods and several approximations must be used such as the Born-Oppenheimer approximation and Density Functional Theory (DFT).

$$H = \sum_i \frac{P_i^2}{2M_i} + \frac{1}{2}\sum_{i \neq j} \frac{q_i q_j}{|\mathbf{R}_i - \mathbf{R}_j|} \tag{4.1}$$

4.1 The Born-Oppenheimer approximation

The Hamiltonian presented in equation 4.1 can be rewritten as equation 4.2 where the nuclei are at position $\mathbf{R}_i$ and have mass M_i and the electrons are at $\mathbf{r}_i$ and have mass m_i. The first term corresponds to the kinetic energy of the nuclei and the second to the kinetic energy of the electrons. The other terms are the Coulomb interactions between electrons and nuclei, electrons and other electrons and between nuclei.

$$H = -\frac{\hbar^2}{2}\sum_i\frac{\nabla^2_{R_i}}{2M_i} - \frac{\hbar^2}{2}\sum_i\frac{\nabla^2_{r_i}}{m_e} - \frac{1}{4\pi\epsilon_0}\sum_{i,j}\frac{e^2Z_i}{|\mathbf{R}_i-\mathbf{r}_j|} + \frac{1}{8\pi\epsilon_0}\sum_{i,j}\frac{e^2Z_iZ_j}{|\mathbf{R}_i-\mathbf{R}_j| + \frac{1}{8\pi\epsilon_0}\sum_{i,j}\frac{e^2}{|\mathbf{r}_i-\mathbf{r}_j|}}$$

(4.2)

The mass of the nuclei is much higher than the electron mass and due to this, the nuclei move much slower. The first approximation we can make is to assume that the nuclei are fixed in their positions and that the electrons are the only particles that move. With this, we reduce the problem to a collection of ZN particles moving in the potential of the positive nuclei. The first term in the Hamiltonian of equation 4.2 is reduced to zero and the last one becomes a constant, which simply shifts the energy.

Having done this approximation, we have thus reduced the Hamiltonian to three terms presented in equation 4.3: the kinetic energy of the electrons T, the electron-electron interaction V, which only depends on the electrons themselves and not the system being studied, and the electron-nuclei interaction term V_{ext}, which is specific of the system being dealt with.

$$H = T + V + V_{ext}$$

(4.3)

4.2 Density Functional Theory

The approximation performed in the previous section simplifies the problem but not enough to be easily solved. However, several methods have been developed to approximate the Hamiltonian to something more soluble, such as the Hartree-Fock method [55] and the more powerful and widely used for electronic systems, Density Functional theory.

We start by two theorems of Hohenberg and Kohn [56], which state:

1. There is a one-to-one correspondence of the electronic ground-state density and the potential due to the coulomb interaction between the electrons and the nuclei, V_{ext}. This implies that any observable is a functional of the ground-state density.

2. The energy functional is given by equation 4.4 where the first term is the Hohenberg-Kohn density functional, which is present in every electronic system, and the second term has its minimum at the density that corresponds to the external potential V_{ext}.

$$E_{V_{ext}}[\rho] = <\Psi|T + V|\Psi> + <\Psi|V_{ext}|\Psi> = F_{HK}[\rho] + \int\rho(\mathbf{r})V_{ext}(\mathbf{r})d\mathbf{r}$$

(4.4)

These theorems allow for the systematic calculation of the properties of solids. However, some care must be taken when dealing with the energy functional. For the ground-state potential, the energy functional is the ground-state energy. Although some other densities can be extremes of the functional, they do not correspond to the ground state energy but to some excited state. However, not every excited state densities are an extreme of the energy functional.

One important detail to attain is that, now, all the information of the system is in the electronic density. Having the density, we can calculate all the solid's properties. Thus, a self-consistent and easy to implement method to calculate the density must be found. This is based on the Kohn-Sham equations and Hamiltonian.

The energy functional [57] can be expressed as a sum of terms, presented in equation 4.5, where T_0 is the kinetic energy of a non-interacting electron gas functional, V_H is the Hartree-Fock functional, V_{xc} is the Exchange-correlation energy functional and V_{ext} is the Nuclei-electron Coulomb interaction functional.

$$E_{V_{ext}}[\rho] = T_0[\rho] + V_H[\rho] + V_{xc}[\rho] + V_{ext}[\rho] \tag{4.5}$$

The second Hohenberg and Kohn theorem could now be used to minimize this functional and thus find the ground state density. However, this would not be efficient, since the calculation of the ground density would still be too complex. The solution to this problem is to consider this functional as a functional of a non-interacting electron gas, under three different potentials: the Hartree-Fock potential, the exchange-correlation potential and the potential due to the nuclei V_{ext}. The Hamiltonian is thus given by equation 4.6.

$$H_{HK} = T_0 + V_H + V_{xc} + V_{ext} = -\frac{\hbar^2}{2m_e}\nabla_i^2 + \frac{e^2}{4\pi\epsilon_0}\int\frac{\rho(\mathbf{r})}{|\mathbf{r}' - \mathbf{r}''|}d\mathbf{r}' + V_{xc} + V_{ext} \tag{4.6}$$

With this, the ground-state density can be calculated using the wave functions that are solution to the Kohn-Sham equation (equation 4.6). By solving a simple Schrödinger equation (equation 4.7), we can obtain all the information of the system, through the calculation of the ground-state density. The obtained wave functions and the single-particle energies from this methods do not have any physical meaning, being just tools to calculate the ground-state energy.

$$H_{HK}\phi_i = \varepsilon_i\phi_i; \rho(\mathbf{r}) = \sum_{i=1}^{N}\phi_i(\mathbf{r})^*\phi_i(\mathbf{r}) \tag{4.7}$$

At this point, the effective potentials depend on the density but the density is only calculated with the potentials and a paradox is reached. The problem is only solved using a self-consistent algorithm. First, a guess of the density is made, ϕ_0. All the potentials are calculated using this density and then inserted into the Kohn-Sham equation. The new calculated wave functions are then used to calculate a new density and the process is repeated. When a certain density is obtained that generates the same density, the algorithm has converged and the final density is consistent and possibly the sought solution.

Two problems remain: the form of the exchange-correlation potential and the choice of the wave function basis ϕ. To solve these problems, several approximations are used. These are covered in the next subsections.

4.2.1   Exchange-correlation potential

Two approximations are widely used: Local Density Approximation (LDA) and the Generalized Gradient Approximation (GGA).

In LDA, the system is divided into infinitesimal volumes, where the electronic density is assumed to be constant. Each volume contributes to the exchange correlation energy by an amount equal to the exchange-correlation energy of a homogeneous electron gas, E_{xc}^{LDA}, which is a function. The exchange-correlation functional is thus given by equation 4.8 The exchange-correlation energy is obtained from the Thomas-Fermi theory, which gives the result also presented in equation 4.8.

$$E_{xc}^{LDA}[n(\mathbf{r})] = \int d\mathbf{r} n(\mathbf{r}) \varepsilon_{xc}(n(\mathbf{r})) = -\frac{3e^2}{4}(\frac{3}{\pi})^{1/3} \int d\mathbf{r} n(\mathbf{r})^{4/3} \tag{4.8}$$

This approximation is only expected to give reasonable results for systems with slowly varying densities, sometimes performing well for other systems. For spin-polarized systems, the LDA can be improved by using a Local Spin Density Approximation (LSDA). Since many magnetic systems are collinear or can easily be approximated as such, the solution passes by developing the kinetic and the exchange-correlation functional in terms of the density of spin up and spin down. The functional has thus the form presented in equation 4.8, where $n_\downarrow$ and $n_\uparrow$ are the spin down and up densities [58].

$$E_{xc}^{LDA}[n_\uparrow(\mathbf{r}), n_\downarrow(\mathbf{r})] = \int d\mathbf{r} n(\mathbf{r}) \varepsilon_{xc}(n_\uparrow(\mathbf{r}), n_\downarrow(\mathbf{r})) \tag{4.9}$$

The GGA transforms the dependence of the infinitesimal volumes on its density of the LDA into a dependence on also the neighbouring volumes. This implies that the functional also depends on the gradient of the density, being described by equation 4.9. The results using GGA are usually better, especially in weakly bonded systems.

$$E_{xc}^{GGA}[n_\uparrow(\mathbf{r}), n_\downarrow(\mathbf{r})] = \int d\mathbf{r} n(\mathbf{r}) \varepsilon_{xc}(n_\uparrow(\mathbf{r}), n_\downarrow(\mathbf{r}), \nabla n_\uparrow(\mathbf{r}), \nabla n_\downarrow(\mathbf{r})) \qquad (4.10)$$

4.2.2 Basis of wave functions

Having the form of the full Hamiltonian, with all the potentials obtained, the calculations can be performed. The problem that remains is what wave function basis should be used. With the wave functions the matrix element of the Hamiltonian is calculated and thus the simple eigenvalue problem of single particles is solved. Several methods have been developed to tackle this problem.

4.2.2.1 Pseudopotential

The first one is the pseudopotential method. Since the plane wave basis is mathematically simple, the pseudopotential uses them as the first option. Due to the basis having to be finite, the set of K values is restricted to $K \ll K_{max}$, which implies that all possible K of the basis set are inside a sphere of radius K_{max} centred at the origin. The value of K_{max} is usually chosen instead from the cut-off energy of the system. The wave functions thus have the form presented in equation 4.11.

$$\phi_{\mathbf{k}}^n(\mathbf{r}) = \sum_{\mathbf{K}} n_{\mathbf{K}}^{n,\mathbf{k}} \exp^{\imath(\mathbf{k}+\mathbf{K})\cdot\mathbf{r}} \qquad (4.11)$$

A problem that arises is that the wave function near the nucleus has a rapid and large variation. Due to this, the number of plane waves required to have a good description is immense, requiring a lot of computational effort. The solution is to introduce a pseudopotential in the inner regions close to the nuclei that makes the wave functions have a slow variation and thus able to be described by a smaller number of wave functions. In the outer regions, the pseudopotentials are close to the real potential. This first approximation allows for the dimension of the basis to be workable but still to have strong results.

4.2.2.2 APW

The pseudopotential describes well the system, if the goal was to study the outer regions. If one needs to have a deep knowledge of the inner regions, like a study of the core level excitations, a new basis must be used. Therefore, the Augmented Plane Waves (APW) basis appeared. It considers that the electrons behave as free particles away from the nucleus, and thus it uses plane waves in these regions. Close to the nucleus, the free atom approximation is considered and the atomic functions are used. The space is thus divided into two different regions depicted in Figure 4.1: the interstitial region (I), between the inner region of different nuclei, and the muffin tin regions (S_α) made up of muffin tin spheres around each atom with a radius R_α. The basis function has the form of equation 4.12, where V is the volume of the unit cell, $\mathbf{r}$, $\mathbf{k}$ and $\mathbf{K}$ the same meaning as in the pseudopotential, $r' = r - r_\alpha$ the position relative to the centre of the atom at r_α, Y_m^l the spherical harmonics, u_l^α the radial part of the Schrödinger equation solution for the alpha atom, E its energy and $A_{lm}^{\alpha,\mathbf{k}+\mathbf{K}}$ the coefficients to be determined.

$$\phi_{\mathbf{K}}^{\mathbf{k}} = \begin{cases} \frac{1}{\sqrt{V}} e^{\iota(\mathbf{k}+\mathbf{K})\cdot\mathbf{r}}, & \mathbf{r} \in \mathbf{I} \\ \sum_{l,m} A_{lm}^{\alpha,\mathbf{k}+\mathbf{K}} u_l^\alpha(r',E) Y_m^l(r'), & \mathbf{r} \in \mathbf{S_{ff}} \end{cases} \tag{4.12}$$
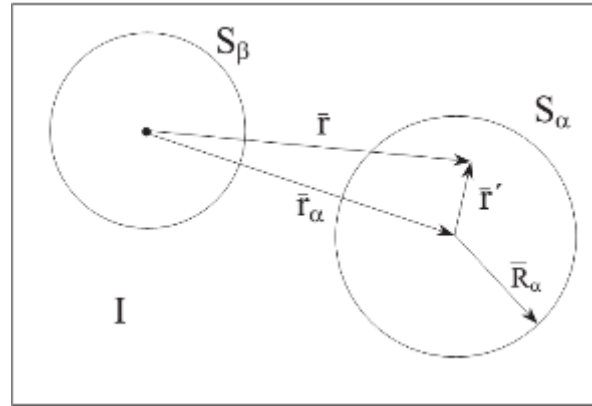
FIGURE 4.1: Division of the unit cell into the muffin tin regions and the interstitial region for a case with two atoms. Adapted from [57]

For the kinetic energy to be defined at the boundary between the two regions, the plane wave must be equal to the spherical harmonic. This gives a condition on the coefficients $A_{lm}^{\alpha,\mathbf{k}+\mathbf{K}}$, expressed in equation 4.13, where j_l is the Bessel function of order l and $R_\alpha = r'$. The coefficients are truncated at a certain value of l, l_{max}, given by the condition $l_{max} = \mathbf{R}_\alpha \mathbf{K}_{max}$. There is no interest in making l_{max} higher than its definition, since it would lead to unstable behaviour at the boundary. Furthermore, the muffin tin radius

must not vary between different atoms, because that would result in a wide range of different values for l_{max}.

$$A_{lm}^{\alpha,\mathbf{k}+\mathbf{K}} = \frac{4\pi\iota^l e^{\iota(\mathbf{k}+\mathbf{K})\cdot\mathbf{r}_\alpha}}{\sqrt{V}u_l^\alpha(\mathbf{R}_\alpha,E)}j_l(|\mathbf{k}+\mathbf{K}|R_\alpha)Y_m^{l*}(\mathbf{k}+\mathbf{K}) \tag{4.13}$$

Having all this, to obtain the wave functions coefficients of its expansion in this basis, a guess for the single-particle energy is made, E replaced by this value and the calculations performed until a new value of the single-particle energy is obtained. When the iteration has converged, both the single-particle energies and wave functions are obtained.

4.2.2.3 LAPW

APW would be a good approach to this problem, except that the calculation of $u_l^\alpha(r',E)$ from an unknown parameter E is too costly and long. Linearised Augmented Plane Wave (LAPW) method appeared to solve this issue. The functions $u_l^\alpha(r',E)$ are not calculated at every step, but are instead approximated by a Taylor expansion around a certain energy E_0, as seen in equation 4.14.

$$u_l^\alpha(r',\varepsilon_\mathbf{k}^n) = u_l^\alpha(r',E_0) + (E_0 - \varepsilon_\mathbf{k}^n)\frac{\partial u_l^\alpha(r',E)}{\partial E}|_{E=E_0} + O(E_0 - \varepsilon_\mathbf{k}^n)^2 \tag{4.14}$$

Having the expansion, the first two terms can be inserted into equation 4.12, giving equation 4.15, where $B_{lm}^{\alpha,\mathbf{k}+\mathbf{K}}$ are a second set of coefficients to be determined, in a similar manner to $A_{lm}^{\alpha,\mathbf{k}+\mathbf{K}}$, by the requirement that the wave function and its derivative at the boundary of the muffin tin spheres must be continuous.

$$\phi_\mathbf{K}^\mathbf{k} = \begin{cases} \frac{1}{\sqrt{V}}e^{\iota(\mathbf{k}+\mathbf{K})\cdot\mathbf{r}}, & \mathbf{r}\in\mathbf{I} \\ \sum_{l,m}[A_{lm}^{\alpha,\mathbf{k}+\mathbf{K}}u_l^\alpha(r',E_0) + B_{lm}^{\alpha,\mathbf{k}+\mathbf{K}}\dot{u}_l^\alpha(r',E_0)]Y_m^l(r'), & \mathbf{r}\in\mathbf{S_{ff}} \end{cases} \tag{4.15}$$

The question that remains is what value of E_0 must be chosen. This question is answered by looking at what kind of state we need to describe. If a state has a p-character, the $B_{lm}^{\alpha,\mathbf{k}+\mathbf{K}}$ coefficients should be small, whereas $A_{lm}^{\alpha,\mathbf{k}+\mathbf{K}}$ coefficients ought to be large. Thus, E_0 should be chosen close to the centre of the p-band. The same argument applies to other types of eigenfunctions with different l values. Due to this, it is not good to choose an universal value for E_0 but a set of values depending on l: $E_{1,l}^\alpha$ with l from 0 to 3. With this, the error is reduced and the basis function can be written as equation 4.16.

$$\phi_{\mathbf{K}}^{\mathbf{k}} = \begin{cases} \frac{1}{\sqrt{V}} e^{i(\mathbf{k}+\mathbf{K})\cdot\mathbf{r}}, & \mathbf{r} \in \mathbf{I} \\ \sum_{l,m} [A_{lm}^{\alpha,\mathbf{k}+\mathbf{K}} u_l^\alpha(r', E_{1,l}^\alpha) + B_{lm}^{\alpha,\mathbf{k}+\mathbf{K}} \dot{u}_l^\alpha(r', E_{1,l}^\alpha)] Y_m^l(r'), & \mathbf{r} \in \mathbf{S_{ff}} \end{cases} \quad (4.16)$$

The accuracy is defined, as it was in APW, by l_{max}. Care must be taken when choosing the K_{max} and the R_α: a high R_α implies a smaller K_{max}, which reduces the dimension of the basis and thus the computational cost, but it can become inappropriate since a description of states far from the nucleus with spherical harmonics is not adequate.

4.2.2.4   APW+lo

Beside the LAPW, another method was developed to improve the APW method. It uses local orbitals (APW+lo), in which, besides the usual basis of equation 4.12 with $E = E_{1,l}^\alpha$ defined previously, another basis called local orbitals is added, having the form of equation 4.17.

$$\phi_{\alpha,lo}^{lm} = \begin{cases} 0, & \mathbf{r} \in \mathbf{I} \\ [A_{lm}^{\alpha,lo} u_l^\alpha(r', E_{1,l}^\alpha) + B_{lm}^{\alpha,lo} \dot{u}_l^\alpha(r', E_{1,l}^\alpha)] Y_m^l(r'), & \mathbf{r} \in \mathbf{S_{ff}} \end{cases} \quad (4.17)$$

The local orbitals are defined for a specific l, m and for atom α. The same set of energies $E_{1,l}^\alpha$ can be used, although not a mandatory condition. The two $A_{lm}^{\alpha,\mathbf{k}+\mathbf{K}}$ and $B_{lm}^{\alpha,\mathbf{k}+\mathbf{K}}$ coefficients are determined from normalization and by the condition that at the muffin tin boundary, the value of the wave function is zero. Both the APW and the lo function are continuous at the sphere boundary whereas their derivative is not. With this basis, besides the dimension being kept small with a good computational cost, states that are not a core or a valence state are well described.

4.3   First principle calculations of Topological Insulators with WIEN2k

To make DFT calculations, several program packages have been developed. One of these packages that is based on full-potential (linearized) augmented plane-wave ((L)APW) + local orbitals (lo) method is WIEN2k. It was developed by P. Blaha, K. Schwarz, G. Madsen, D. Kvasnicka and J. Luitz at the Institute of Materials Chemistry, TU Vienna. Simulations will be performed to compute the band structure and the density of states to have a comparison and support to the experimental results.

The preparation of the simulation starts by generating the structure of the material based on its lattice parameters, atomic positions and space group. After this step, the type of approximation to the exchange-correlation potential must be chosen. The best approach is to use the generalized gradient approximation of Perdew, Burke and Ernzerhof. To simulate the topological insulator properties of thin films, a supercell geometry must be used. Furthermore, Spin-orbit coupling (SOC) must be included has a second variational step using scalar-relativistic eigenfunctions as basis after the initial calculation converges.

Several works have been published using WIEN2k to obtain a theoretical verification of the experimental results or to study what could be the behaviour of a variety of topological insulators.

In [59], Bi_2Se_3, a material of the same family of Bi_2Te_3, was studied in two ways. ARPES was used to observe the single Dirac cone of the surface of this family of materials. WIEN2k was used to support the results of the ARPES study. In Figure 4.2, the obtained band structure along two different directions is presented as well as the theoretical calculations. These Figures show the excellent agreement between the theoretical and experimental results.
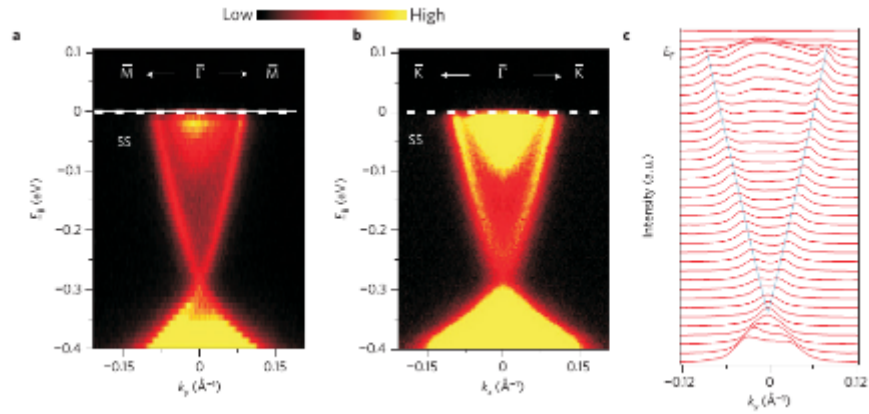
FIGURE 4.2: a)-b) High-resolution ARPES measurement of the surface band structure of Bi_2Se_3 (111), measured with an incident photon energy of 22 eV. c) WIEN2k calculated band structure along the same path as in a). Adapted from [59]

4.4   Boltzmann Transport Properties

From Density Functional Theory calculations, the electronic properties, namely the band structure, of solids are obtained. Several properties of a solid are extremely well described

within the Boltzmann theory, specially its transport properties. Boltzmann transport theory calculates the solid's properties from the energy bands and their derivatives [**?**]. Thus, from the results of a DFT calculation, the transport properties could be obtained.

BoltzTraP is a code that calculates the transport properties of solids from the output of a WIEN2k calculation, based on the Boltzmann Transport Theory [60]. The code relies on the Fourier expansion of the band energies, while keeping the group symmetry by using star functions in the Fourier expansions.

The Fourier expansions of the energy bands are given by equation 4.18, where $\mathbf{R}$ is the lattice vector and $\{\Lambda\}$ are the n point group rotations. In order to have an appropriate description of the energy bands, more star functions are used than energy bands, while imposing a constrain to the fit ε_i^* to be exactly equal to the original band energies, ε_i. With the additional freedom, a roughness function is minimised. The choice of the roughness function is important for suppressing oscillations between data-points and a discussion about this function can be found elsewhere [61–63]. Furthermore, to ensure that the fitted energies are equal to the calculated band energies and also to have a minimised roughness function, the number of plane-waves must be larger than the number of band energies. Following these constraints, the coefficients $c_{\mathbf{R}_i}$ are calculated and the energy bands are successfully expanded.

Having the energy bands expanded, it is a matter of calculating their derivatives to obtain properties of the solid. Several properties are obtained at the end of a successfull calculation, specially the conductivity times the relaxation time, the seebeck coefficient and the pauli magnetism. All these properties can be obtained as a function of temperature, for a pre-defined temperature range, as well as as a function of the chemical potential for a constant temperature.

$$\varepsilon_i^* = \sum_{\mathbf{R}} c_{\mathbf{R}_i} S_{\mathbf{R}}(\mathbf{k}); S_{\mathbf{R}}(\mathbf{k}) = \frac{1}{n} \sum_{\{\Lambda\}} e^{i\mathbf{k}\cdot\Lambda\mathbf{R}} \tag{4.18}$$

4.5 Performed Calculations

Calculations using WIEN2k of Bi_2Te_3 and Sb_2Te_3 materials were performed for the bulk materials and for Sb_2Te_3 $1 \times 1 \times 1$ supercell. The density of states and band structure was obtained. Inserting the output of the calculations into the BoltrzTrap code, the conductivity times the relaxation time, the seebeck coefficient and the Pauli magnetic susceptibility were calculated.

4.5.1 Initialisation

The initialisation of the calculations was made by introducing the lattice parameters, atomic positions and space groups of the bulk materials and generating the structure. In order to produce the supercell structure, the x supercell command of WIEN2k was used.

The remaining initialisation parameters were the default ones. The exchange correlation potential was the generalised gradient approximation of Perdew, Burke and Ernxerhof.

4.5.2 RmtKmax and k-mesh

Several k-points for both bulk materials were tested in order to verify the number of k-points needed to have a good description of the materials. The energy of the bulk materials was the chosen parameter to be evaluated. In Figure 4.3, the energy as a function of the number of k-points is represented for Bi_2Te_3 and Sb_2Te_3.

For Bulk Bi_2Te_3, it is observed that the energy starts to be constant for both when SOC is considered or not for 1000 k-points. The same behaviour is observed for bulk Sb_2Te_3.
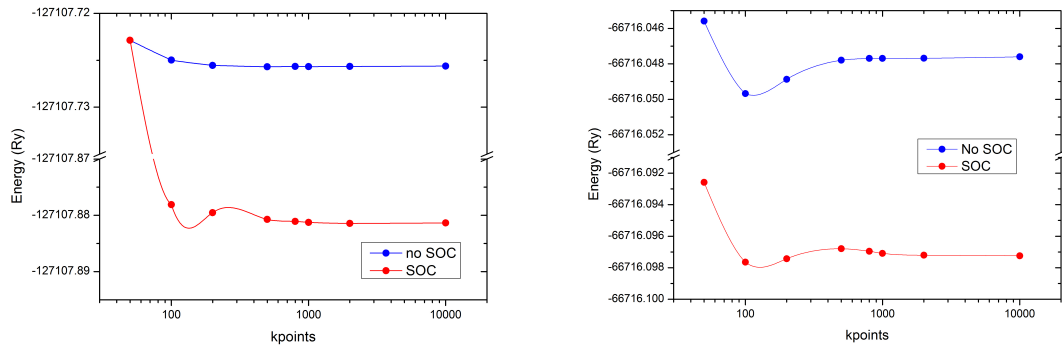
FIGURE 4.3: Energy of bulk Bi_2Te_3 and Sb_2Te_3 as a function of the number of k points.

The $R_{mt}K_{max}$ parameter was chosen following the recommendation presented on the WIEN2k website [64].

To calculate the transport properties, 1000 k-points were used for bulk Sb_2Te_3. For Bi_2Te_3, the procedure of [65] was used.

For the Sb_2Te_3 supercell, following the recommendation of [57], 80 k-points were used.

4.5.3 Volume optimisation

In order to have a correct calculation of the material's properties, volume optimisation was performed. The optimal unit cell parameters were obtained for the bulk materials. The volume optimisation was performed considering Spin Orbit Coupling.

Since both Sb_2Te_3 and Bi_2Te_3 belong to the R-3m structure group, it was defined that the b unit cell parameter was equal to a and that the γ angle was 120º. The optimised unit cell results are presented in Table 4.1. A comparison with obtained experimental parameters is presented. The optimized unit cell parameters of Sb_2Te_3 were used for the supercell structure.

Material	Optimised Parameters Å		Experimental Parameters Å[66, 67]	
	a	c	a	c
Bi_2Te_3	4.1385	28.861505	4.388	30.46
Sb_2Te_3	4.0289	28.77865	4.2648	30.45

TABLE 4.1: Optimised Unit cell Parameters of Bi_2Te_3 and Sb_2Te_3 and a comparison with experimental results [66, 67]

Chapter 5

Bi$_2$Te$_3$ bulk

Bi$_2$Te$_3$ is a recently discovered topological insulator material that is being the focus of several TI properties studies, specially of its transport properties. This chapter is devoted to the study of bulk Bi$_2$Te$_3$. Analysis from sample preparation until measurements of its transport and magnetic properties, namely the resistivity, Seebeck coefficient and magnetic susceptibility, are presented. They are compared with numerical results obtained using the WIEN2k software package and BoltzTraP code, allwoing for an explanation of the obtained results to be made.

5.1 Structural and Morphological Properties

5.1.1 SEM

The morphology of the Bi$_2$Te$_3$ fabricated powders was assessed using SEM. Figure 5.1 shows a SEM image of the Bi$_2$Te$_3$ powder wth a high degree of non homogenous granularity. Granules with sizes ranging from 3 μm to 150 μm are observed.
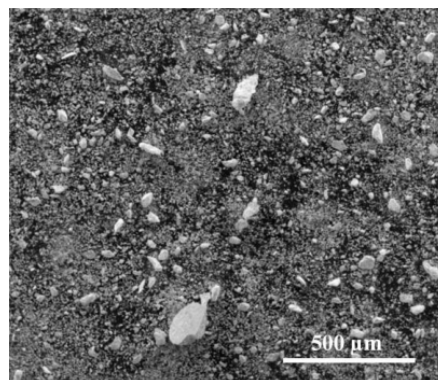
FIGURE 5.1: SEM image of Bi$_2$Te$_3$ powder.

5.1.2   EDS

To verify the stoichiometry of the fabricated Bi_2Te_3 powder, EDS studies were performed. It was demonstrated that the Bi_2Te_3 powder is constituted by an 38.72% of Bi and 61.28% of Te. The obtained results are in great accordance with the expected values of 40% of Bi and 60% of Te.

5.1.3   XRD

X-ray diffraction was performed on the Bi_2Te_3 powder. The obtained XRD pattern is presented in Figure 5.2. Superimposed on Figure 5.2 is also the reference powder diffraction pattern of Bi_2Te_3 [66]. From the comparison between the two patterns, almost all the obtained diffraction peaks are identified to correspond to the Bi_2Te_3 phase, having a rhombohedral crystal geometry and belonging to the R-3m space group. However, some small peaks are not identified as belonging to the Bi_2Te_3 phase. These probably belong to the Bi_2O_3 phase that tipically appears at the granular surface.
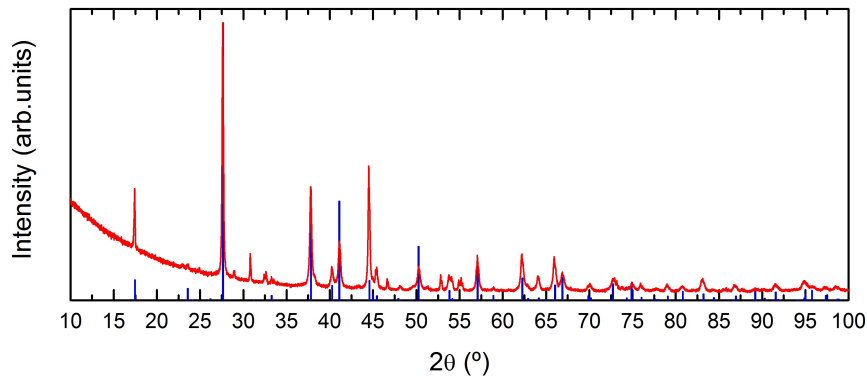
FIGURE 5.2: XRD pattern of the fabricated Bi_2Te_3 powder and the reference pattern from [66].

5.2   Electronic and Magnetic Properties

5.2.1   Density of States

The total density of states was obtained for bulk Bi_2Te_3 as described in Chapter 4.

Figure 5.3 presents the total density of states of bulk Bi_2Te_3 without considering SOC and with the inclusion of SOC. The density of states has roughly the same behaviour when considering SOC or not. The most striking difference occurs at the band gap. It decreases

with the consideration of SOC, from 190 meV to 54 meV. The value considering SOC is in great accordance with previously reported values [29, 68].
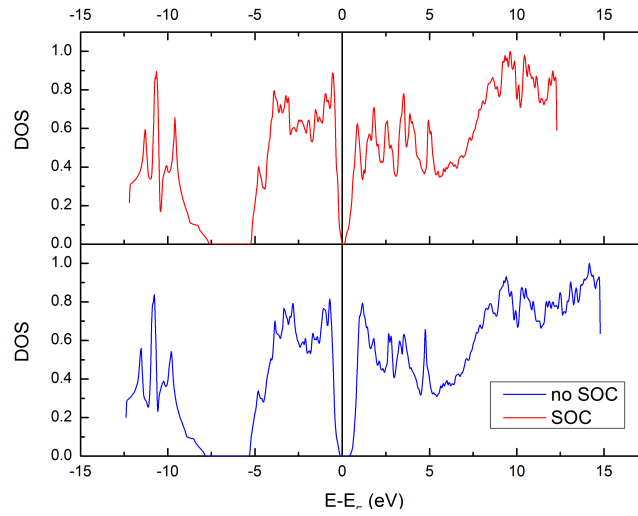
FIGURE 5.3: Total density of states of bulk Bi$_2$Te$_3$, with and without the inclusion of SOC.

5.2.2 Band Structure

The band structure of bulk Bi$_2$Te$_3$ was calculated following Chapter 4.

Figure 5.4 presents the bulk band structure with and without the inclusion of SOC. Both considerations have an extremely similar behaviour specially for energies away form the band gap, where some degeneracies are lifted with SOC included. However, near the band gap, the inclusion of SOC changes the band structure. The Fermi level is moved closer to the conduction band, which is indicative of n type behaviour, as expected for BiTe3. Furthermore, the indirect band gap observed when SOC is not included becomes indirect with SOC. This is the behaviour reported [68] and thus it shows the importance of the inclusion of SOC as a second variational parameter.

5.2.3 Resistivity

The resistivity of the Bi$_2$Te$_3$ bulk pellet was measured as described in Chapter 3. The resistivity as a function of temperature of the bulk Bi$_2$Te$_3$ is presented in Figure 5.5, for temperatures between 7 and 300K.

It is observed that the resistivity is approximately $2.4 \times 10^{-4} \Omega m$ at room temperature, keeping the same order of magnitude for all the range of temperatures studied. Three distinct regions can be identified. For temperatures between, approximately, 25 and 180
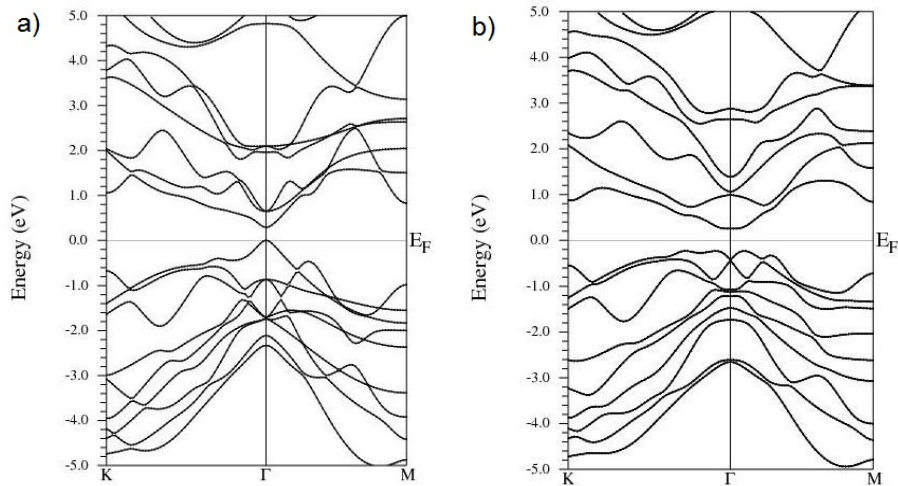
FIGURE 5.4: Band structures of bulk Bi_2Te_3 a) without the consideration of SOC and b) with SOC included.

K, the resistivity slowly increases with a temperature increase. However, when the temperature is cooled down from 25 K, the resistivity has an abrupt increase, reaching similar resistivity values of those at 100 K. In the third region, at temperatures higher than 180K, the resistivity decreases with temperature, reaching its lowest value at 300 K.
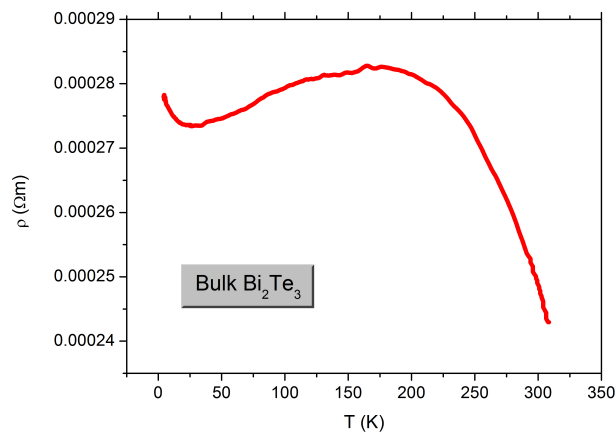
FIGURE 5.5: Resistivity of bulk Bi_2Te_3 as a function of temperature for temperatures between 7 and 300 K.

In order to compare the theoretical calculations with the experimental results, the resistivity times the relaxation time as a function of temperature is calculated using the BoltzTraP code described in Chapter 4, for temperatures between 50 and 300 K. The obtained results are represented in Figure 5.6.

The three distinct resistivity behaviour regions are observed as in the resistivity of the fabricated bulk Bi_2Te_3. This indicates that the calculations and the experimental reults

are having the same trends. However, the temperature limits of the different regions are different of the observed experimental results. In Figure 5.6 one sees that the first region occurs for temperatures lower than 100 K and that the third region starts at approximately 250K. Being Bi$_2$Te$_3$ a semicodunductor material, even a small number of impurities or excess donor or acceptor atoms, changes its transport properties. The fabricated bulk material can have impurities and small oxidation as observed in subsection 5.1.3. It can then be concluded that the experimental and theoretical results are in great accordance, which shows the potentiality of WIEN2k and BoltzTraP to describe Bi$_2$Te$_3$.
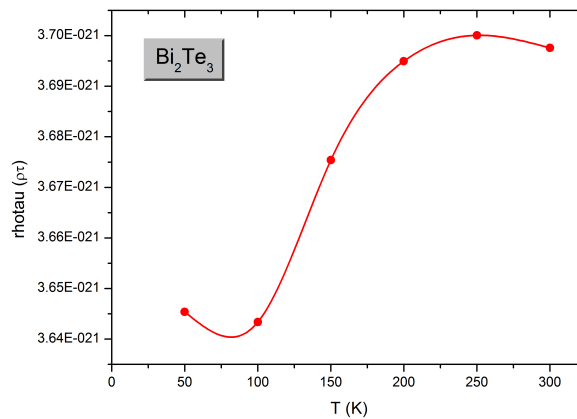
FIGURE 5.6: Resistivity of bulk Bi$_2$Te$_3$ calculated using the BoltzTraP as a function of temperature for temperatures between 10 and 300 K.

5.2.4 Seebeck Coefficient

The Seebeck coefficient of the bulk Bi$_2$Te$_3$ was obtained using the setup described in Chapter 3. The voltage drop as a function of the temperature difference is plotted in Figure 5.7. The voltage behaves linearly with the temperature difference, increasing with an increase in the temperature difference. By performing a linear fit and using equation 3.3, the Seebeck coefficient was calculated.

The Seebeck coefficient of the fabricated Bi$_2$Te$_3$ pellet is -153 μV/K. The negative value indicates that the bulk material has the expected n type behaviour. Furthermore, it is in accordance with previously obtained values for bulk materials [35].

The Seebeck coefficient of bulk Bi$_2$Te$_3$ as a function of temperature is also calculated as described in Chapter 4 for temperatures in the range of 50 K to 300 K. The results are presented in Figure 5.8. The Seebeck coefficient is negative for the full range of temperatures
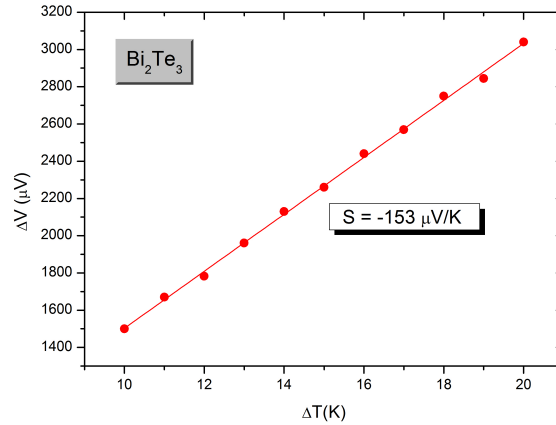
FIGURE 5.7: Voltage drop as a function of the temperature difference for bulk Bi_2Te_3 at room temperature. The Seebeck Coefficient is obtained from the slope of the linear fit.

studied, suggesting as stated before, the Bi_2Te_3 is a n type semiconductor. Furthermore, its magnitude smoothly increases with temperature.
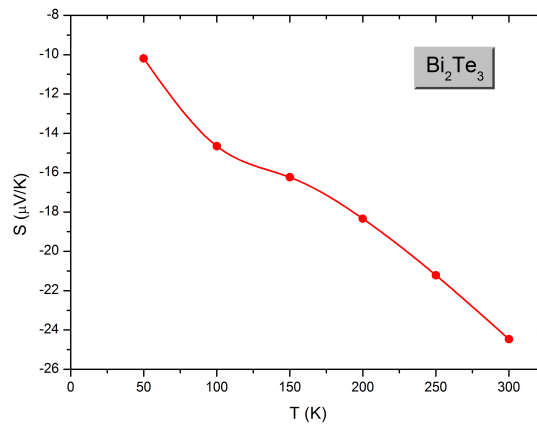
FIGURE 5.8: Seebeck coefficient of bulk Bi_2Te_3 as a function of temperature obtained using the BoltzTraP code.

Comparing the experimental with the theoretical results for 300 K, it is observed that the Seebeck coefficient of the fabricated Bi_2Te_3 is 6 times larger than the predict theoretically. This indicates that the calculations should be performed with an higher number of k-points or with a different number of carrier concentration. In fact, Shi et al. [69] showed that carrier concentration plays an enormous role in the value of the Seebeck coefficient. In this calculation, $4 \times 10^{+21}$ carriers/cm^3 were used and by comparing with the obtained theoretical value, it is in great accordance with their predictions.

5.2.5 Magnetic susceptibility

The magnetic susceptibility as a function of temperature of the synthesised bulk Bi_2Te_3 material was measured using SQUID magnetometer as described in Chapter 3.

In Figure 5.9, the absolute value of the magnetic susceptibility as a function of temperature is presented for temperatures within the range of 5 and 370 K, with an inset of the M vs. H curve at 300 K. An anomaly is observed in the range 40 to 75 K which is related with the magnetic oxygen contamination inside the SQUID magnetometer. From the inset, it is concluded that Bi_2Te_3 is a diamagnetic material, since the magnetisation increases in magnitude with the applied magnetic field, but has the opposite direction of the field. Furthermore, the magnetic susceptibility is extremely small, having, approximately, a maximum value of $5 \times 10^{-12} m^3/mol$ at 320 K , which is also indicative of the diamagnetic behaviour.

Focusing on the susceptibility as a function of temperature, it is verified that, for temperatures lower than approximately 20K, the susceptibility increases rapidly. For temperature higher than 20 K, the susceptibility still increases with temperature, but at a slower rate than for lower temperatures. It reaches a maximum at approximately 320K, where with an increase in temperature, the susceptibility decreases.

FIGURE 5.9: Absolute value of the magnetic susceptibility of the fabricated bulk Bi_2Te_3 as a function of temperature, for temperature within 5 and 370K. The inset shows the M vs. H curve at 300K, indicative of diamagnetic behaviour.

The susceptibility of bulk Bi_2Te_3 is also calculated using the BoltzTraP code as presented in Chapter 4. The absolute value of the susceptibility for bulk Bi_2Te_3 is represented in Figure 5.10 as a function of temperature, for the temperature range of 50 and 400 K. The maximum value of the calculated susceptibility is approximately $1.19 \times 10^{-9} m^3/mol$.

This value is approximately 200 times larger than the value obtained experimentally. As discussed before, the BoltzTraP calculations of Bi_2Te_3 were performed with an high concentration of carriers. Since the diamagnetism susceptibility increases with the density of carriers n, $|\chi| \propto Z_{eff} r^2 n$, high theoretical susceptibility values are obtained. Furthermore, for the calculation of the experimental susceptibility, the pure molar mass of Bi_2Te_3 was used, assuming the synthesised material has the theoretical density. However, since the bulk Bi_2Te_3 pellets are compressed, the density might have a different value, which can alter the molar mass of the bulk material.

In spite of the difference in susceptibility value, the theoretical curve presented in Figure 5.10 has an extremely similar behaviour as the experimentally obtained susceptibility curve. It increases with temperature for temperatures up to approximately 320 K, where the maximum in susceptibility occurs. For temperatures lower than 100 K, the variation rate appears to be slightly higher, as observed experimentally for temperatures close to these values. For temperatures higher than 320 K, the susceptibility decreases, as once again it is observed for the experimental behaviour of the synthesised bulk Bi_2Te_3. It is thus verified that WIEN2k and the BoltzTraP code can describe the Bi_2Te_3 material extremely well.
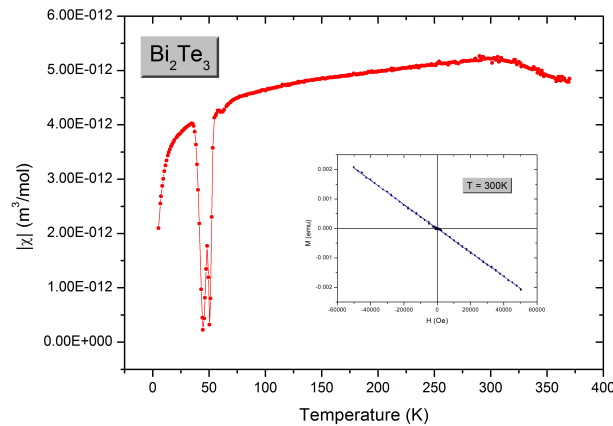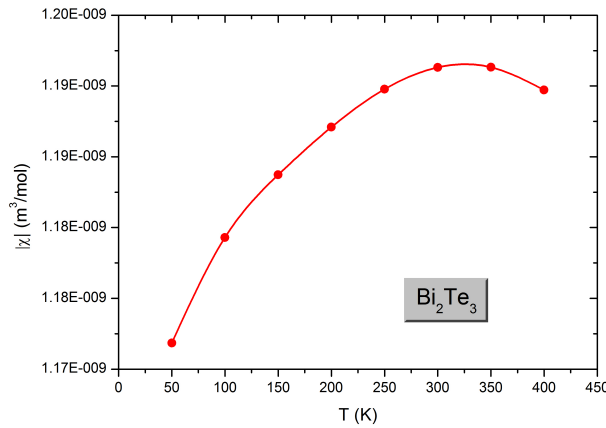

FIGURE 5.10: Absolute value of the magnetic susceptibility of the bulk Bi_2Te_3 as a function of temperature, for temperature within 5 and 370K, calculated using the BoltzTraP code.

Chapter 6

Sb_2Te_3 thin films

Antimony telluride Sb_2Te_3, belonging to the Bi_2Se_3 and Bi_2Te_3 family of semiconductors, shares various properties with them, thus, also potentially being a 3D topological insulator material. However, due to its band structure, namely the location of the Fermi level and the shape deviation of the perfect Dirac cone, it has not been of interest and the detailed study of its properties has not been properly addressed, due to its complexity. Thus, thorough studies of their electronic and transport properties are of the utmost importance.

This Chapter is devoted to the fabrication of Sb_2Te_3 thin film. Morphological and structural properties combined with a deep insight into their electronic and magnetic properties is presented. The experimental results will be supported by theoretical first principle calculations.

6.1 Structural and Morphological Properties

6.1.1 SEM

Scanning Electron Microscopy was used to study the morphology of the thin films. Figure 6.1 displays SEM images of the 10 nm Sb_2Te_3 thin film on Si and the 100nm thin film glass substrate. From the images, it can be concluded that the 100 nm thin film presents a high degree of uniformity. However, on the 10 nm thin film, some regions with less material are visible, which is explained by the extremely small deposition time, thus, preventing covering of the full substrate. The various substrates defects, specially existing in glass, are clearly visible in Figure 6.1.
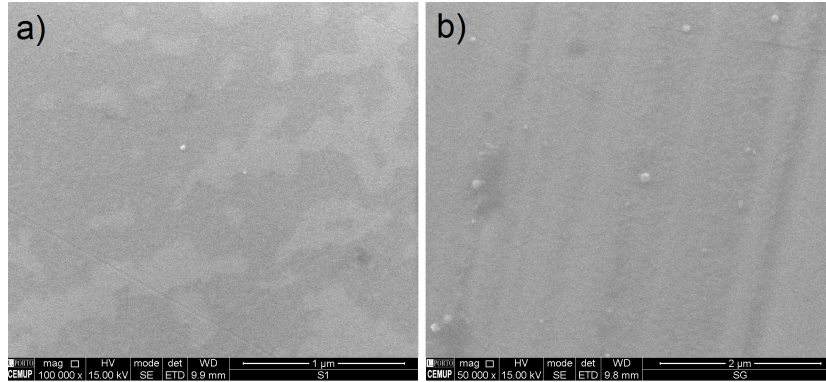
FIGURE 6.1: SEM top images of the Sb_2Te_3 thin films: a) 10 nm thin film on Si, b) 100 nm thin film on Glass.

Cross-section SEM profiles were also obtained to study thin films thickness and the interfaces. Figure 6.2 shows the cross-section image of the 100 nm Sb_2Te_3 thin film deposited on glass, as example. From this image, it is observed that the thickness profile is homogeneous, obtaining approximately 83 nm for the thin film thickness. The value is still in great agreement with the nominal value of 100 nm, since there were some issues to stabilise the electron beam when performing this measurement. By breaking the thin film in two halves to study its cross section, deformations might have also occurred which can change the thickness at the cut edge.
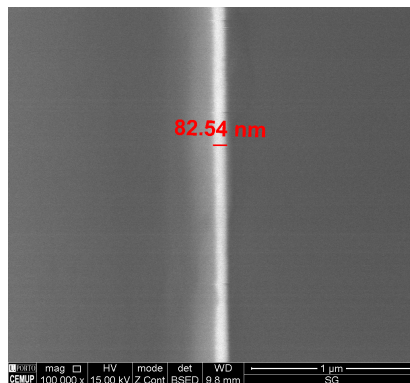
FIGURE 6.2: SEM cross-section images of the Sb_2Te_3 100 nm thin film deposited on Glass.

6.1.2 XRR

XRR was performed to compliment the measurement of the thickness of the thin films.

Figure 6.3.a) shows the reflectivity of the Sb_2Te_3 thin film deposited to be 100 nm in Si. The Fresnel decrease of reflectivity is observed as well as the Kiessig fringes. From this plot, the angle of the maximum of each fringe was obtained. Using equation 3.1, a linear

fit was performed of the obtained fringe's data and it is presented in Figure 6.3.b). The expected linear behaviour is observed. From the slope, the thickness was obtained to be 105.5 nm, which is in agreement with the intended nominal value. Comparing with SEM images (Figure 6.2), it a considerable imprecision can be observed, reaching more than 17%. Nevertheless, since the fabricated thin films have a wide range of thicknesses (10, 50, 100 and 400 nm), following the SEM and XRR results, the nominal thicknesses will be used to understand the physics behind the observed phenomena.
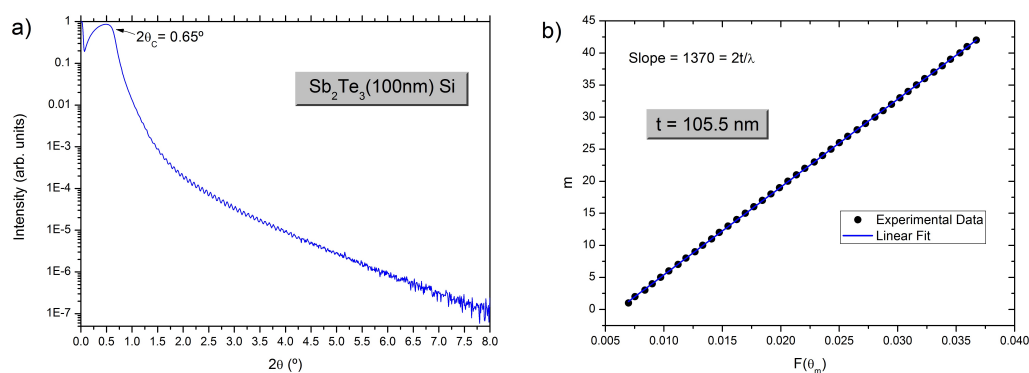
FIGURE 6.3: XRR analysis of the Sb₂Te₃ 100 thin film deposited on a Si substrate: a) reflectivity curve; b) order of the fringes as a function of the theta function $F(\theta_m)$, from which the thickness is obtained.

6.1.3 EDS

To obtain the stoichiometry of the thin films, EDS analysis was performed. Figure 6.4 shows the atomic percentage of each element as a function of the thickness for the thin films deposited in Si, which present a very similar behaviour to the glass substrate. The obtained results unveil that slightly changes of the stoichiometry are seen for thin films that were fabricated from the commercial target with values of 60% Te and 40% Sb, as observed by EDS results. A mean value of 55% of Te content is obtained. This difference arise probably during the top down fabrication process, when the target is bombarded by an argon ion beam, heating it and removing and ejecting material into the chamber. Due to the higher vapor pressure of Te when compared to Sb and with the heating of the target, it is expected more Te is spread through the chamber, instead of being deposited on the substrate. This increases the percentage of Sb at a cost of the Te percentage, thus explaining the observed results.

From Figure 6.4, it is also observed that the percentage is constant for all the thicknesses except the 10 nm thin film. This reinforces the above given explanation. The deposition time of the 10 nm thin film is much lower, which corresponds to a decrease in the target temperature, which reduces the amount of Te evaporated to the chamber. Also, remark that, being an extremely small thickness thin film, the error in the EDS measurement increases, which should be taken into account to explain the observed deviation.
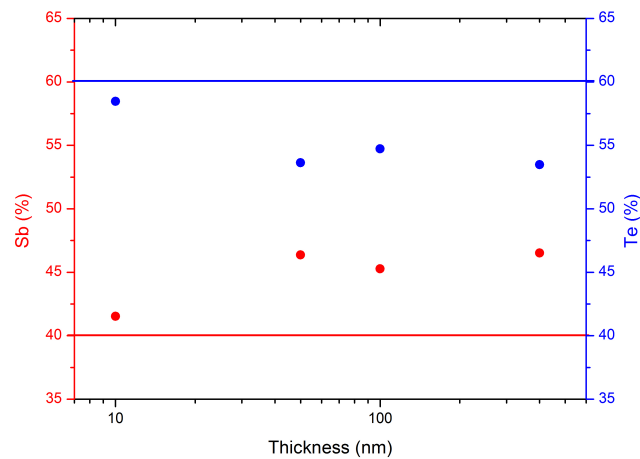
FIGURE 6.4: EDS analysis of the Sb_2Te_3 thin films on Si.

6.1.4 XRD

X-ray diffraction patterns of the thin films were obtained as described in Chapter 3 to study the crystallography of the thin films. Figure 6.5 shows the diffraction patterns obtained for the Sb_2Te_3 thin films deposited in Glass and Si.

From these results, two reflections can be observed at 25.1º and 52º, which can be indexed by the planes (0 0 6) and (2 0 5), respectively [67]. These correspond to the Sb_2Te_3 phase, with a rhombohedral crystal geometry (space group R-3m). Notice that these reflections are presented in almost all the thin films produced showing that thickness is not playing a major role on the degree of freedom of its crystallinity. Moreover, this can be extended to both substrates, since the profile of the two peaks is similar, which allows the conclusion that the substrate did not influence the growth of the crystallographic phase. The broadness of the reflections brings out that the samples are constituted by small nanocrystallites. The main difference between the obtained patterns is present in the XRD pattern of the 10 nm thin films, where only the (2 0 5) peak is observed, having

an extremely small intensity. Since these films are extremely small, their XRD signal is also lower, with an increase contribution to the XRD signal coming from the substrate and/or sample holder. Furthermore, these XRD patterns are in great accordance with the SEM images, since the 10 nm thin films did not have a uniform growth on the surface of the substrate, with certain regions being covered with more material than others. Due to this, the crystallinity of the different regions is not identical, reducing the signal of the observed peak and making the first peak completely disappear.

Focusing on the diffraction pattern of the thin films deposited on glass substrate, pictured in Figure 6.5.a), the typical extremely broad peak characteristic of fused silica glass is observed for all thin films. For the 10 nm thin film XRD pattern, peaks of the sample holder are also observed.

For the thin films deposited in Si, a similar situation as in glass occurred and it is depicted in Figure 6.5.b). The Si substrate peaks are detected for all the thin films, as well as, sample holder peaks, in the 10 and 400 nm thin films. This is is expected for the 10 nm thin film, due to its extremely small thickness, being also observed for the glass thin film. With the thickness increase to 400 nm, the sample holder peaks should not be present, since with an increase in thickness, their contribution should decrease. Moreover, an intensity reduction of the substrates peaks with an increase in the thickness is observed. A possible explanation for the observed sample holder peaks is that during the measurement, the sample was not correctly centred. This causes the x-ray beam to be also incident on the sample holder, which, by not being an amorphous material, also produces some reflections. In spite of these peaks, the Sb₂Te₃ phase could be successfully and clearly identified and compared with literature for this type of thin films [70–72].
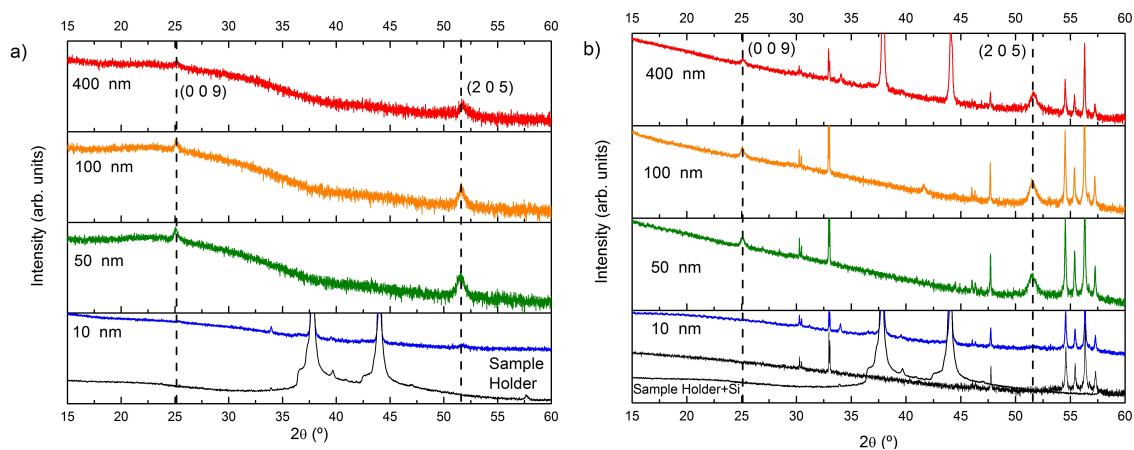
FIGURE 6.5: XRD pattern of the Sb₂Te₃ thin films deposited in a) Glass and b) Si.

6.2 Electronic and Magnetic Properties

6.2.1 Density of States

Similar to previous performed calculations of Bi_2Te_3 in Chapter 5, the total density of states was obtained for the bulk materials and the thin films using WIEN2k and the parameters as described in Chapter 4.

The density of states of bulk Sb_2Te_3 is presented in Figure 6.6, with and without SOC being considered. Both DOS have a similar behaviour, with the main difference being the position of the Fermi energy regarding the band gap and the value of the band gap. The band gap decreases when SOC is included, from 218 meV to 92 meV. With SOC being considered, there is a shift of the Fermi level towards the valence band. This is indicative of p type behaviour, which is consistent with the observed behaviour of Sb_2Te_3.
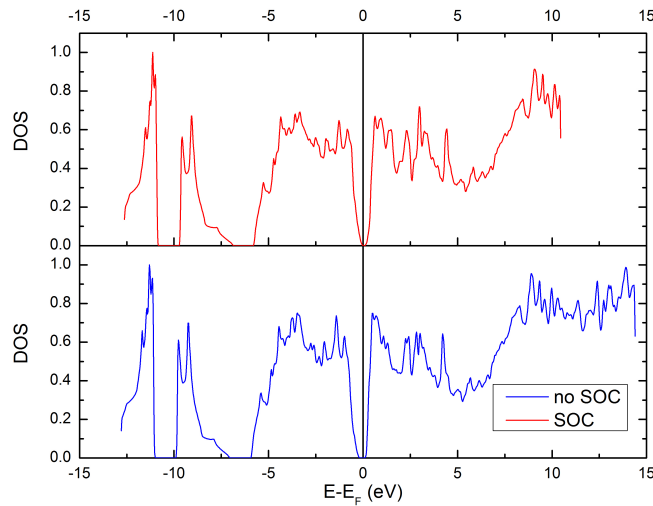
FIGURE 6.6: Total Density of States of bulk Sb_2Te_3 with and without the inclusion of SOC.

The DOS was also obtained for the 1x1x1 supercell structure, corresponding to a 3 nm thin film in vacuum. It is represented in Figure 6.7. It has an overall similar behaviour to the bulk DOS, with two main differences: 1) the bulk band gap is closed. When not considering SOC, the gap is shifted to an higher $E - E_F$ value. However, when considering SOC, any band gap ceases to exist; 2) a sharp DOS peak occurs at an energy inside the bulk band gap, which was not visible when not considering SOC. This is indicative of a new state appearing inside the bulk band gap, which is consistent with the topological surface state.
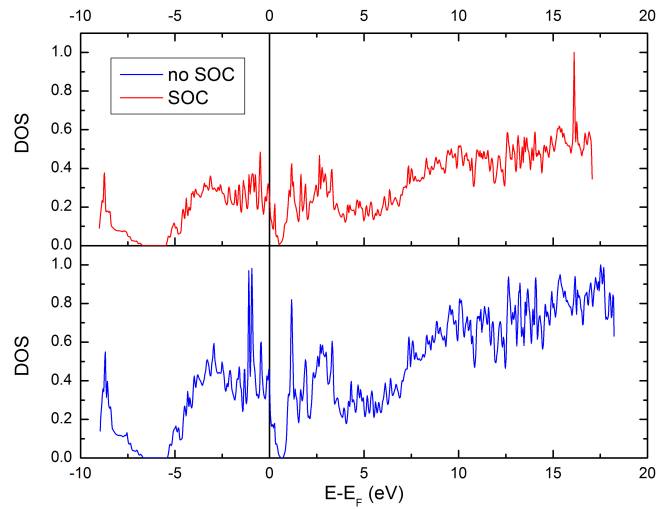
FIGURE 6.7: Total Density of States of 1x1x1 Sb₂Te₃ supercell, corresponding to a 3 nm thin film in vacuum, with and without the inclusion of SOC.

6.2.2 Band Structure

The Band Structure of the surface of the Sb₂Te₃ bulk and thin film was also calculated following Chapter 4.

In Figure 6.8 the bulk band structures are presented, with and without the consideration of SOC. Both have an extremely similar behaviour, with some degeneracies being lifted when SOC was included. Without the consideration of SOC (Figure 6.8.a)), the band gap at the Γ point is smaller than the band gap at the Γ point with SOC (Figure 6.8.b)). This appears to be contradictory to the results obtained in 6.2.1. The DOS showed that the band gap decreases with the inclusion of SOC. However, the results presented here correspond to the surface band structure. The total DOS corresponds to the whole material, including the bulk contribution. Thus, the band gap observed here is the surface band gap, whereas the one presented in subsecion 6.2.1 is the bulk band gap of the calculated structures.

The band structure of the Sb₂Te₃ 1x1x1 supercell is represented in Figure 6.9. The overall behaviour is similar when SOC was considered or not. Furthermore, although some similarities to the bulk band structure are detected, the band structure presentes an higher density in the thin film form. In Figure 6.9.a), it is still observed a band gap when SOC was not considered. This is in great accordance with the results of the previous subsection. However, when SOC is considered (6.9.b)), the band gap no longer exists. Moreover, at 0.2 eV the characteristic Dirac point and cone of the topological surface state is observed. This is inside the bulk band gap at the Γ point presented in Figure 6.8.b).
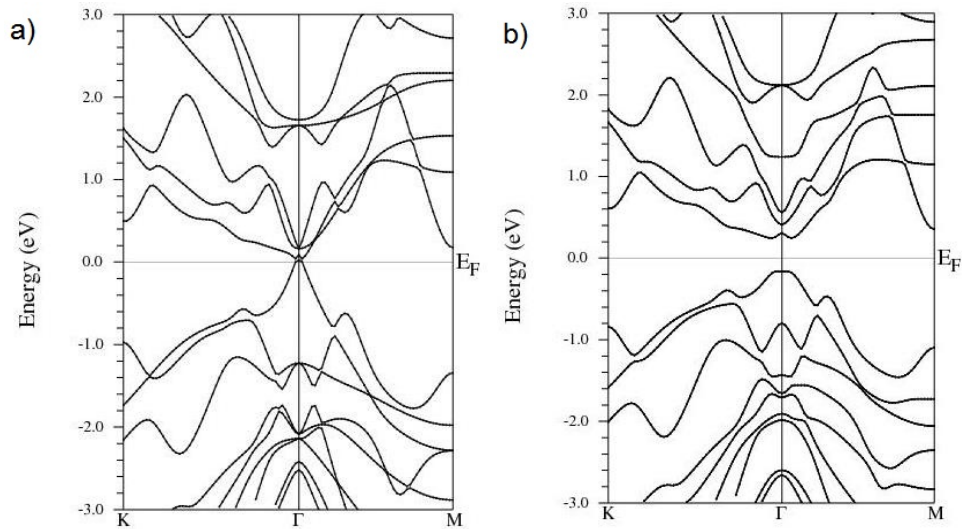
FIGURE 6.8: Band structure of bulk Sb_2Te_3 for energies between -3.0 eV and 3.0 eV around the Fermi energy, for the surface k-path K-Γ-M.

From this, it can be concluded that a 3 nm Sb_2Te_3 thin film already exhibits the topological surface state.
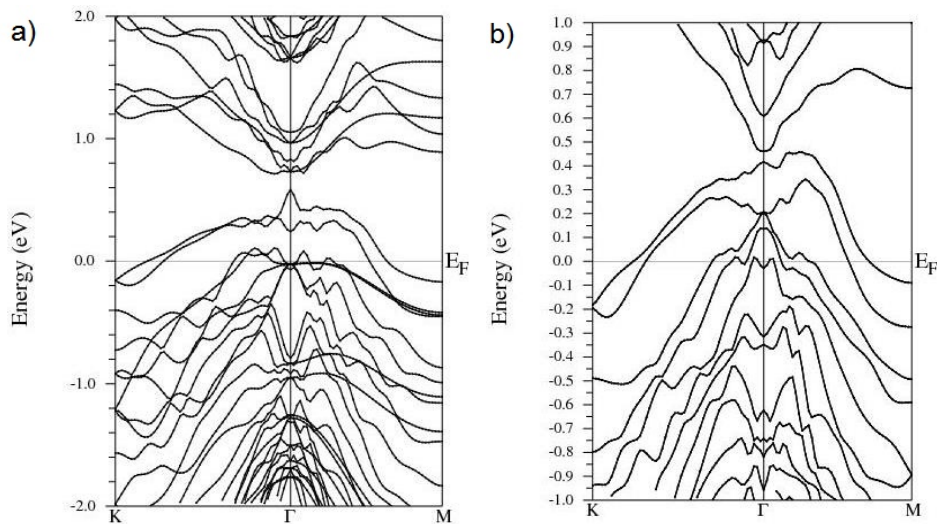
FIGURE 6.9: Band structure of the Sb_2Te_3 1x1x1 supercell, corresponding to the 3nm thin film in vacuum, for energies between -2.0 eV and 2.0 eV around the Fermi energy, when SOC was not included and -1.0 eV and 1.0 eV around the Fermi Energy, when SOC was included, for the surface k-path K-Γ-M.

6.2.3 Resistivity

The resistivity of the thin films was measured as described in Chapter 3. Figure 6.10 shows the resistivity of the thin films deposited in Glass and in Si as a function of temperature.
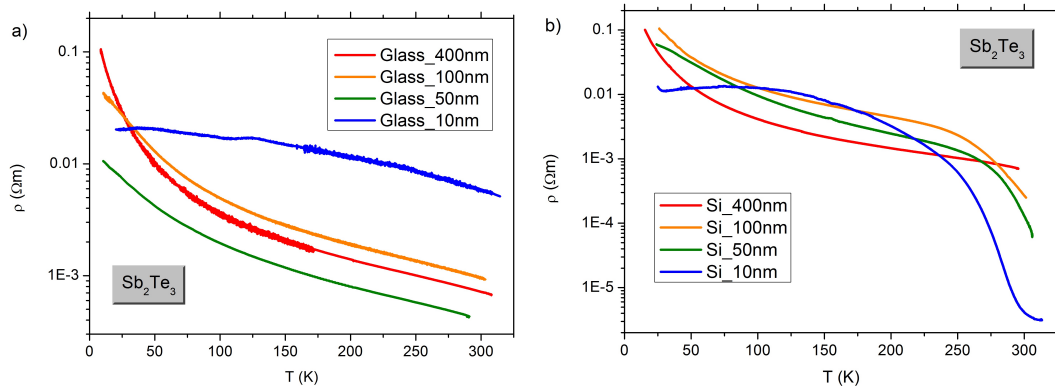
FIGURE 6.10: Resistivity as a function of temperature for the Sb_2Te_3 thin films deposited in a) Glass and b) Si for temperatures between 10K and 310K.

The resistivity decreases with an increase of temperature for all the thin films. This is the characteristic transport of a semiconductor. The 400 nm thin films deposited in Glass and in Si have exactly the same behaviour with temperature. The resistivity decreases from approximately 0.1 Ωm at 10 K to $1 \times 10^{-3} \Omega m$ at 300 K. From this, it can be concluded that there is no substrate influence on the 400 nm thin films, as also already observed from, for example, XRD results.

Observing the 100 nm and the 50 nm thin films deposited in Glass, the resistivity has the same behaviour with temperature as the 400 nm thin films. The 100 nm resistivity spawns similar values of resistivity as the 400 nm thin films. For the 50 nm thin film, the resistivity only varies between 0.01 Ωm at 10 K and $1 \times 10^{-3} \Omega m$ at 300 K. Considering the same thin films on Si substrate, the resistivity is similar for low temperatures. At high temperatures, close to room temperature, a more abrupt decrease in the resistivity occurs. It starts decreasing more abruptly at around 250 K, reaching values of approximately $1 \times 10^{-4} \Omega m$. Thus, for these thin films, with a much smaller thickness, the Si substrate influences hugely the electric conduction, as opposed to the 400 nm thin film.

Focusing on the 10 nm thin films, the resistivity behaves in a completely different way when comparing with the other thin films. For the 10 nm thin film deposited in Glass, it still decreases with an increase in temperature. However, the variation is not so abrupt as for the other thin films, with values between 0.02 Ωm at 10 K and $5 \times 10^{-3} \Omega m$. With an Si substrate, the situation is completely different. At high temperatures, despite the situation being close to the 50 and 100 nm thin films on Si, the resistivity reaches a much smaller value $3 \times 10^{-6} \Omega m$. It also has a small inversion at 300 K, appearing to reduce the rate of

variation of the resistivity once again. For lower temperatures, another inversion occurs. The resistivity slightly decreases on cooling, for temperatures between 125 K and 25 K approximately. At temperatures lower than 25 K, the resistivity starts increasing again. These behaviours are observed for several reasons. Glass has a negligible conductivity, which ensures that all the contribution to the resistivity come from carriers of the thin films. However, this is not the case for an Si substrate, due to its semiconductor nature and much higher conductivity. The 10 nm thin films are extremely small when compared to the others and their growth is not as uniform as the other thin films, as evidenced by the SEM results presented in 6.1.1. With this, a substrate contribution is expected and it is indeed observed for the 10 nm thin films. This shows the substrate plays an enormous role in the electric transport properties, since it changes the nature of the transport at low and high temperatures for the 10 nm thin films and at high temperatures for the other films, whereas for 400 nm thin film no substrate contribution is observed.

A deeper analysis to the nature of the electric resistivity was performed based on the electrical transport of extrinsic semiconductors [73]. The conductivity of a semiconductor is given by equation 6.1, where q is the carrier charge, n and p are the electron and hole concentrations, respectively, and μ_n and μ_p are the mobilities of each carrier.

$$\sigma = q(n\mu_n + p\mu_p); \rho = \frac{1}{\sigma} = \frac{1}{q(n\mu_n + p\mu_p)} \tag{6.1}$$

At low temperatures, most of the intrinsic carriers of a semiconductor are frozen in their atomic positions, due to the small vibrational energy. Because of this, the conductivity is extremely low, whereas the resistivity is very high, as observed in Figure 6.10. Most of the conduction comes from impurity and donor or acceptor atoms in the semiconductor, starting to move out of their atomic positions. The electron concentration at low temperatures is proportional to $exp\left(-\frac{\Delta E}{2k_B T}\right)$, where $\Delta E = E_c - E_d$ is the energy difference between the bottom of the conduction band and a dopant level. Thus, by plotting the logarithm of the resistivity as a function of the inverse of the temperature, this energy difference can be obtained for an extrinsic semiconductor. The other component of the resistivity is the mobility. At low temperatures, the scattering of electrons with lattice vibrations (electron-phonon scattering) is small. The most important scattering occurs between the electrons and the ionized impurities. This type of scattering leads to a mobility proportional to a power of the temperature $T^{3/2}$.

At high temperatures, all the intrinsic carriers of the semiconductor contribute to the conduction and the impurity effects are decreased. The concentration of carriers is thus proportional to the exponential factor $exp\left(-\frac{E_g}{2k_BT}\right)$, where E_g is the band gap of the semiconductor. As it happens at the low temperature regime, by plotting the logarithm of the resistivity as function of the inverse of temperature, the band gap can be obtained. At high temperatures, the main type of scattering becomes electron-phonon, due to the increase of the vibrations with temperature. Due to this, the mobility is again proportional to a power of the temperature, but in this regime, proportional to $T^{-3/2}$. Thus, plotting the logarithm of the resistivity as a function of the logarithm of the temperature, also gives an insight into the main scattering type.

Figure 6.11 shows one set of the above mentioned plots performed for the Sb$_2$Te$_3$ 100 nm thin film deposited on Glass. These analysis were also performed to the 400 nm and 50 nm thin films deposited in Glass and to the 400 nm, 100 nm and 50 nm deposited in Si substrates. The results are presented in 6.1. It was considered that these analyses were of no interest to the 10 nm thin film. An estimative of the thin film band gap, donor level and type of scattering can be obtained from the thin films deposited in Glass as well as the 400 nm thin film deposited in Si, since no substrate influence exists.
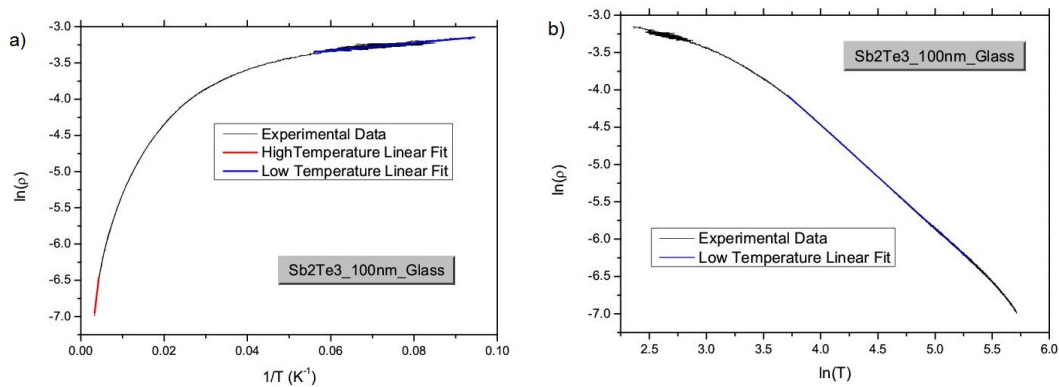
FIGURE 6.11: Analysis of the resistivity of the Sb$_2$Te$_3$ 100 nm thin film on Glass. a) Logarithm of the resistivity as a function of the inverse of temperature and b) Logarithm of the resistivity as a function of the logarithm of temperature.

The results of the band gap as a function of the thickness are presented in Figure 6.12. The band gap increases with thickness. Although there is no definite band gap value for Sb$_2$Te$_3$ since various experimental [74–76] and theoretical [77–79] studies present different values in the range of 90 to 220 meV, a comparison with some reported values as well as the previously calculated value in subsection 6.2.1 is also shown. The thin film band gap

Thin Films		$\Delta E(meV)$	$E_g(meV)$	α
Glass	400 nm	2.03	110	-1.47
	100 nm	0.896	84	-1.38
	50 nm	0.72	62	-1.521
Si	400 nm	4.66	120	-1.63
	100 nm	0.076	624.9	-1.55
	50 nm	0.109	1284	-1.84

TABLE 6.1: Band gap of the Sb_2Te_3 thin films from the electric resistivity.

tends to previous bulk band gap results. This shows that for thicknesses higher than, approximately, 100 nm, the thin films start to behave as a bulk material. On the other hand, previously calculated 3 nm thin films band gap is much lower, being approximately 60 meV [80]. The obtained values for the fabricated thin films also show this tendency, since for the 50 nm thin film, the band gap is already 62 meV. This demonstrates that the band gap estimate from the resistivity gives a good insight into the electronic properties of the thin films. However, it must be taken into consideration that these band gaps correspond to the bulk band gaps of the thin films or calculated structures, and not the surface band gap. From a resistivity measurement, due to the enormous contribution from the bulk of the thin films, the surface band gap and conduction cannot be probed.

For the 100 and 50 nm thin films deposited in Si, the obtained results cannot be considered as giving a good estimate of the Sb_2Te_3 thin film band gap, due to the immense substrate influence. However, an estimative of the Si substrate band gap can be obtained. The band gap of pure Si is approximately 1.2 eV at room temperature [REF]. With a decrease in the thickness from 100 nm to 50 nm, accompanied by an increase of substrate contribution to the conduction, the obtained value is approximately equal to the expected Si band gap value. This demonstrates once again that the substrates influences immensely the transport properties of the Sb_2Te_3 thin films, specially the ones with lower thickness, and proves that the observed behaviour at high temperatures comes from Si conduction.

Focusing on the estimated values for the ΔE distance between the conduction band and a dopant level, it is observed that for the thin films without substrate influence (400 nm thin films and the 100 and 50 nm thin films deposited in Glass), it increases with thickness of the film. This behaviour is characteristic of an extrinsic semiconductor. Taking in consideration the composition results obtained by EDS in subsection 6.1.3, two phenomena can explain the estimated distance values and their increase with thickness. The amount of telluride appears to decrease with relation to the amount of antimony with
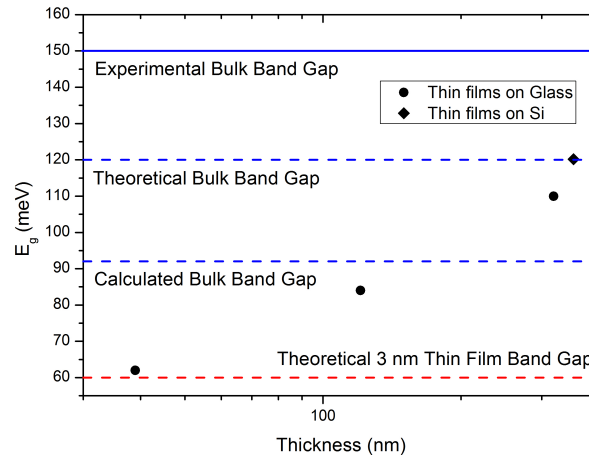
FIGURE 6.12: Sb₂Te₃ thin film Band Gap as a function of the thin film thickness.

an increase in the thickness. This can lead to vacancies in the thin film structure or to substitution of Te sites to Sb sites, becoming acceptors sites. These phenomena lead to either a decrease in the number of negative carriers, namely electrons, or to an increase of positive carriers (holes). This explains the observed characteristic extrinsic semiconductor behaviour and the estimation of the existence of an dopant level in the band gap.

Analysing the temperature power factor α of the resistivity presented in Table 6.1, one observes that the estimated values are close to -3/2. This is indicative of scattering of the carriers with the ionised impurities. However, it was expected that for temperatures close to room temperature, the most significant type of scattering was lattice scattering, with the power factor becoming 3/2. Due to the high impurities and dopant concentrations observed by the EDS results of subsection 6.1.3 and estimated from the previous analysis, the major contribution to the scattering continues to come from impurities, even at high temperatures. Lattice scattering might be observed for temperatures higher than room temperature, but no evidence of this can be obtained from these results.

The resistivity times relaxation time of the bulk and supercell was obtained using the code BoltzTraP as described in Chapter 4. The results are represented in Figure 6.13, where calculations performed considering or not SOC are presented for both the bulk and supercell calculation. From the results, it is observed that the transport properties are intrinsically different whether SOC is considered or not. By comparing with the experimental measurements of the resistivity, it can be concluded that the inclusion of SOC is of the upmost importance to have a valid result. The resistivity decreases with temperature

when SOC is included, both in the bulk materials and the thin films. For the thin films, it is also observed that the resistivity varies one order of magnitude with temperature. This behaviour is similar to the thin film resistivity measurements presented in Figure 6.10. Thus, it can be concluded that there is great agreement between the experimental measurements and the performed theoretical calculations using WIEN2k and BoltzTraP.
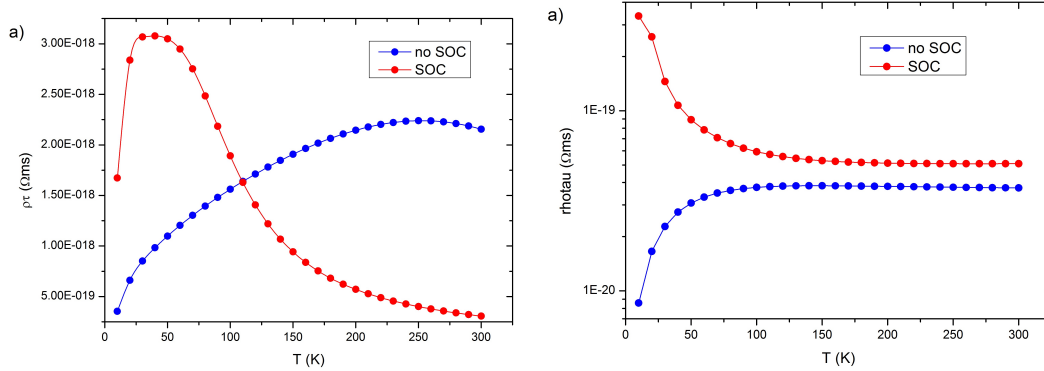
FIGURE 6.13: Resistivity times relaxation time of the bulk and 1x1x1 supercell as a function of temperature, ranging between 10 and 300 K.

6.2.4   Seebeck Coefficient

The Seebeck coefficient of the thin films was measured at room temperature following Chapter 3. Figure 6.14.a) and b) present the voltage drop as a function of the temperature difference across the thin films deposited in glass substrates and Si substrates, respectively. The expected linear behaviour was obtained for all the thin film structures. Furthermore, the voltage across the thin films is negative and decreases with an increase in the temperature difference. From the linear fits of these curves, the Seebeck coefficient was obtained following equation 3.3. The results are summarised in Table 6.2.

Thickness	Glass	Si
400 nm	20 $\mu V/K$	81 $\mu V/K$
100 nm	41 $\mu V/K$	253 $\mu V/K$
50 nm	41 $\mu V/K$	-
10 nm	-	801 $\mu V/K$

TABLE 6.2: Seebeck Coefficient of the Sb_2Te_3 thin films.

Considering only the glass substrate thin films, it is observed that the value of the Seebeck coefficient depends on the thickness of the thin films, approximately increasing
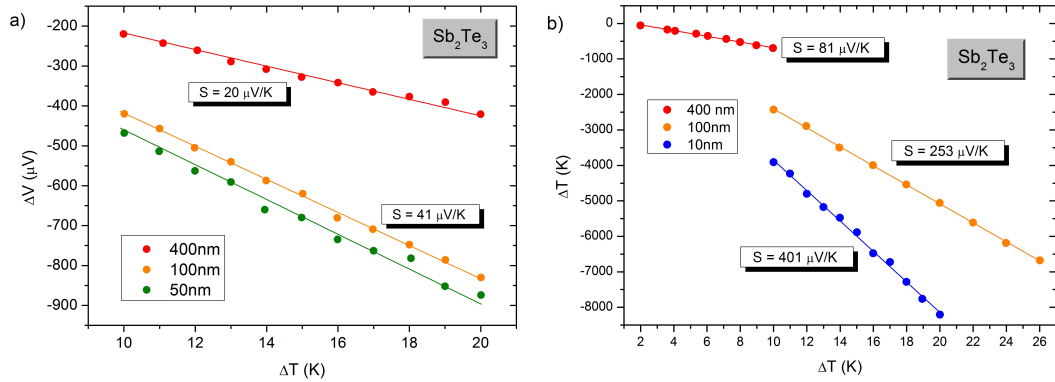
FIGURE 6.14: Seebeck coefficient of the Sb₂Te₃ thin films a) deposited in Glass and b)deposited in Si.

with a decreasing thickness. This measurement could not be performed on the 10 nm thin film due the high resistance values coming from the glass substrate.

Analysing the thin films deposited on Si substrate, an increase of the Seebeck coefficient with a decrease in thin film thickness is also observed. However, the values are much higher than the ones obtained for the thin films deposited in glass, specially for the 10 nm thin film. From the resistivity results of subsection 6.2.3, it is concluded that there is an huge substrate influence on the electronic transport. Furthermore, previous measurements show that the Seebeck coefficient of Si can be close to 800 $\mu V/K$. Thus, the measured Seebeck coefficient of the 10 nm thin film corresponds to the Si substrate. However, the extremely high Seebeck coefficient of the Si substrates also influences the measurement of the coefficient of higher thickness thin films. From the resistivity results of the 50 and 100 nm thin film deposited in Si, it is already known that the substrate influences the transport properties. In spite of the substrate having no influence on the resistivity of the 400 nm thin film, it influences greatly the Seebeck coefficient of this thin film, by increasing it to 4 times the corresponding Seebeck coefficient of the thin film deposited in glass.

The Seebeck coefficient as a function of temperature was calculated using the BoltzTaP code as presented in Chapter 4. Figure 6.15 shows the Seebeck coefficient as a function of temperature for the bulk and the studied supercell, with and without the inclusion of SOC. It is clearly visible that considering SOC is of the utmost importance since the curves have completely different behaviours whether it is considered or not.

For bulk Sb₂Te₃, it is observed that the Seebeck coefficient increases with temperature

up to, approximately, 140 K, reaching a maximum value around 263 $\mu V/K$. For temperature higher than 140 K, the Seebeck coefficient decreases with temperature until 240 $\mu V/K$ at room temperature. The Seebeck coefficient of the thin film also has a similar behaviour. It increases from 5 $\mu V/K$ at 10 K to 110 $\mu V/K$ at 25 K, decreasing monotonically for higher temperatures, until reaching the almost constant value of 30 $\mu V/K$ for temperatures between 200 and 300 K. Thus, the Seebeck coefficient decreases when the material is in thin film form.

Moreover, by comparing these results with the values obtained from the measurements of the thin films at room temperature, there is a good accordance between the values of the Seebeck coefficient of the thin films deposited in glass and the calculated thin film.
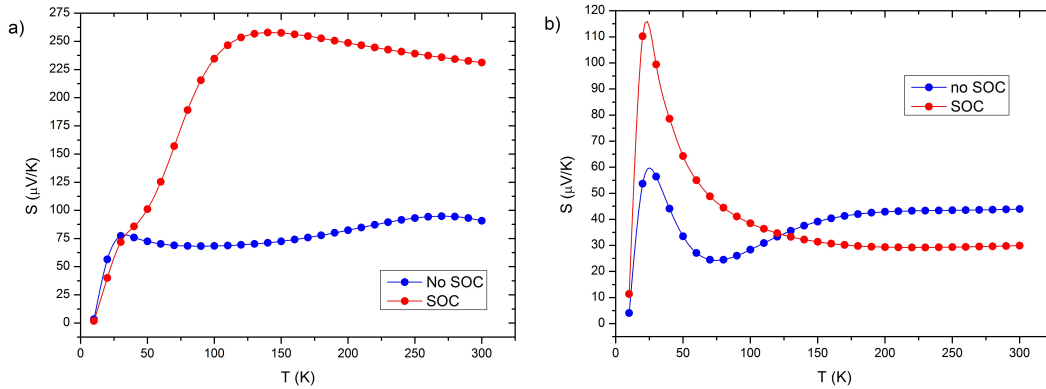
FIGURE 6.15: Seebeck coefficient as a function of temperature of Sb_2Te_3 a) bulk and b) supercells calculated using the BoltzTraP code.

6.2.5 MagnetoResistance

The Magnetoresistance (MR) of the Sb_2Te_3 100 nm thin film deposited in Glass was measured as described in Chapter 3. Figure 6.16 shows the MR as a function of the applied field in a longitudinal configuration (6.16.a)) and transversal configuration (6.16.b)) for 4 different temperatures, 2 K, 4.2 K, 10 K and 20 K.

Considering the applied longitudinal direction, it is observed that the MR for all temperatures is negative at low magnetic fields, exhibiting an approximate quadratic behaviour. It decreases with the magnitude of the magnetic field until a minimum is reached. For higher temperatures, this minimum occurs at increasing magnetic fields, from 0.8 T at 2K to 4.8 T at 20 K. Furthermore, the magnitude of the minimum increases
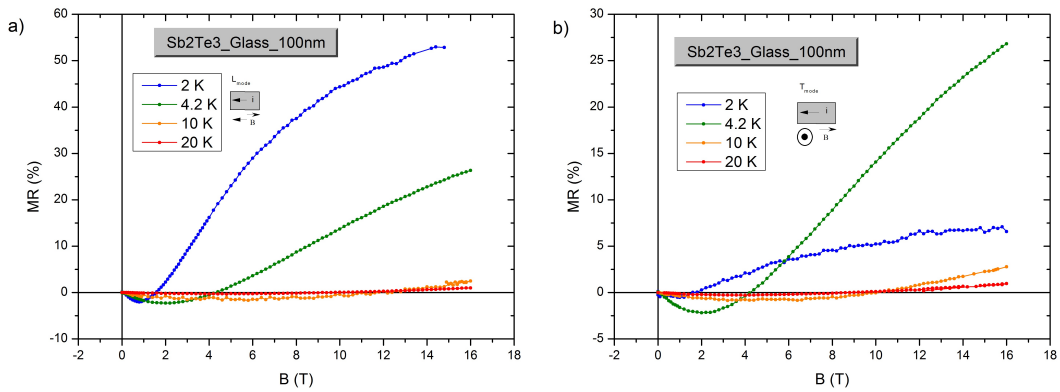
FIGURE 6.16: Magneto Resistance of the Sb₂Te₃ 100 nm thin film deposited in Glass in the a) longitudinal and b) transversal configuration for four different low temperatures.

with lower temperatures, reaching -2% at 2 K and only -0.35% at 20 K. After the minimum, an inversion of the curve is observed and the MR starts to increase with the magnetic field. For lower temperatures, it becomes positive at lower magnetic fields than the ones needed for high temperatures. The MR becomes zero again at 1.6 T at 2 K whereas only at 9.6 T at 20 K. From this, it appears as the negative MR behaves quadratically with the field. At high magnetic fields, the MR increases drastically with a decrease in temperature, reaching values as high as 50% for 2 K, with only 1% being obtained for 20 K.

When the magnetic field is applied in the transversal configuration (perpendicular to the thin film), the MR behaves in a similar manner as in the longitudinal configuration, for 4.2 K, 10K and 20K. However, at 2K, the MR behaves differently. At high magnetic fields, it is much smaller than when the field was parallel, only being 7% at 16 T. For low magnetic fields, the approximate quadratic behaviour still exists.

The behaviour at low magnetic fields is characteristic of doped semiconductors and amorphous materials [81, 82]. In these materials, some electrons are localised by the existing vacancies or defects. These electrons can be localised with a certain non-zero momentum and a definite spin. Due to energy considerations, the moving electron carriers spin must be antiparallel to the localised electrons. One of the types of scattering in these systems is by spin reversal of the carrier electrons. When a magnetic field is applied and starts aligning the various spins, this scattering mechanism no longer exists and the conduction increases when compared to its value in a zero magnetic field. The increase in conductivity based on this phenomena has a quadratic behaviour in low magnetic fields [81] and this is what is observed in Figure 6.16.

At 2 K in a transversal configuration, this effect is still observed, but for much lower values when compared to the longitudinal configuration. At 2 K, more electrons might be localised, with, as discussed, an antiparallel spin to the moving electrons. Due to magnetic anisotropy, the majority of these spins might be aligned in the direction of the thin film. When a low magnetic field is applied in this direction, it is harder to align the spins than in the longitudinal direction. Thus, the type of scattering at play is not as reduced as for a parallel magnetic field, reducing the conductivity from its longitudinal value and thus reducing the resisitvity difference between zero and low magnetic fields.

When the magnetic field is increased, all the spins start to be aligned, making this effect negligible, and the characteristic monotonic increasing and positive magnetoresistance behaviour at high fields is observed.

Focusing on the lowest temperatures at high magnetic fields, some deviations of the monotonic increasing behaviour are observed at 2 K. In Figure 6.17, the resistance normalised by the resistance at maximum field is presented as a function of the inverse of the magnetic field for hight magnetic fields between 5 T and 16 T. At 4.2 K, no deviations and noise is observed and the perfect monotonic behaviour is observed. However, the situation is rather different at 2 K. Due to the high values of the MR observed in Figure 6.16, the observed deviations are not due to noise of the measurements. Thus, it appears as oscillations with the inverse of the magnetic field are detected.
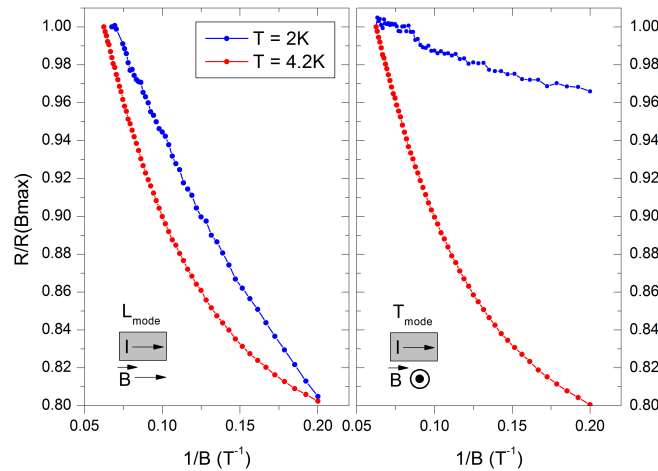
FIGURE 6.17: Normalised resistance to the maximum magnetic field value as a function of the inverse of the magnetic field, for the longitudinal and transverse configurations at 2 and 4.2 K.

The evidence of the existance of oscialltions is consistent with the Shubnikov-de Hass

oscillations reported for various topological insulator thin films at high fields. Although they appear to be extremely small and negligible, its is expected such small oscillation as [48] demonstrated for Molecular Beam Epitaxy (MBE) Sb$_2$Te$_3$ thin films. Figure 6.18 shows the results they obtained for a 13 nm thin film, where it is clearly visible the small oscillation nature of the oscillations, since practically no signal is detected in the resistance as function of magnetic field curve. Thus, it can be considered that the measured thin film has the expected topological insulator behaviour.

FIGURE 6.18: Evidence of the small Shubnikov-de Haas oscillations in MBE grown Sb$_2$Te$_3$ thin films. Adapted from [48].

Chapter 7

NiFe/Sb$_2$Te$_3$ heterostructures

With the 3D topological insulators fully charcterised, specially their electronic and transport properties, the interest lies in tuning and controlling the topological surface state. This is achieved by including magnetism, either by doping the topological insulators or fabricating thin film heterostructures with magnetic thin films.
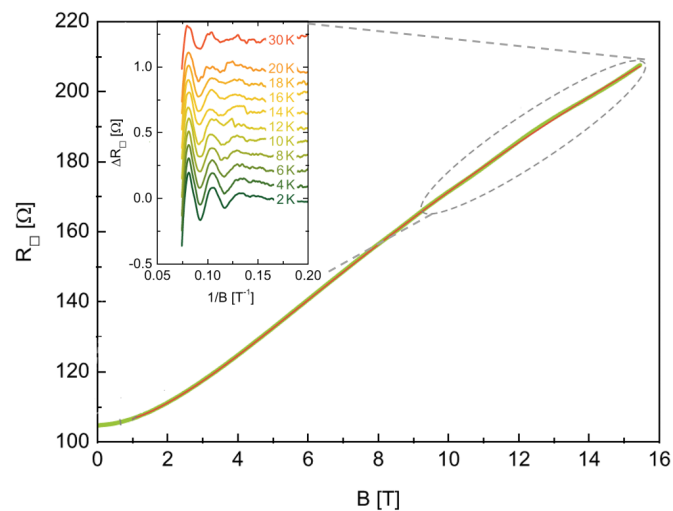
In this Chapter, one of those heterostructures is studied, namey by using NiFe (permalloy acting as the magnetic thin film and Sb$_2$Te$_3$ as the topological insulator material. A deep study into the morphological and structural properties of the NiFe thin films and the NiFe/ Sb$_2$Te$_3$ heterostructures is presented. Following these studies, the full characterisation of their transport properties is performed.

7.1 Structural and Morphological Characterisation

7.1.1 SEM

The morphology of the NiFe thin films and NiFe/Sb$_2$Te$_3$ heterostructures was studied using SEM as described in Chapter 3.

Figure 7.1 shows the SEM top image of the NiFe 100 nm thin film grown in glass. Some defects are observed that correspond to defects already existing in the glass substrate. In spite these defects, the thin film has a good uniformity throughout the substrate surface.

In Figure 7.2, the cross-section SEM images of the various NiFe / Sb$_2$Te$_3$ heterostructures deposited in Si is presented. The layer and total thickness of the NiFe(100nm) / Sb$_2$Te$_3$(100nm) and NiFe(50nm) / Sb$_2$Te$_3$(50nm) heterostructures was measured. Similar to the previous Chapter 6, there is a good accordance between the measured values and the nominal thicknesses. Furthermore, the fabricated heterostructures layers have a wide
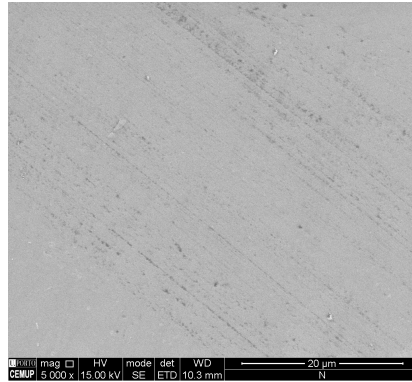
FIGURE 7.1: SEM top image of the NiFe 100nm thin film on Glass.

range of thicknesses (10, 50 and 100 nm) in order to allow the study of the different transport phenomena at different physical limits. Since the differences are smaller than 10 nm, the physical limits still uphold.

For the NiFe(100nm) / Sb_2Te_3(10nm) heterostructures only the total thickness could be measured. This was due to the impossibility of SEM measuring thin film thicknesses with values as low as 10 nm. In spite of this, the total thicknesses is in agreement with the nominal value.
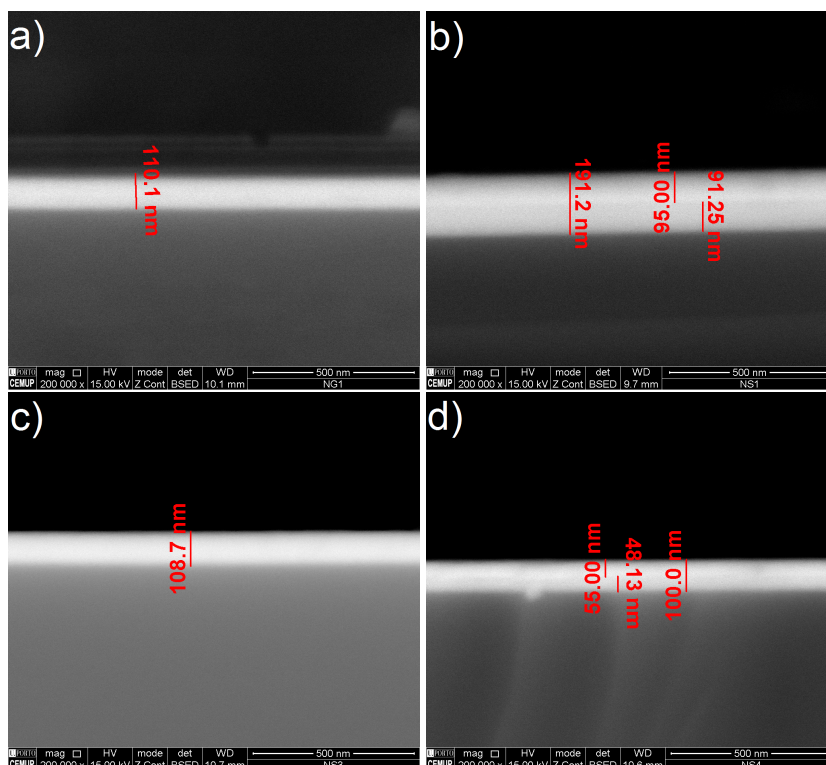
FIGURE 7.2: SEM cross-sectional images of the NiFe / Sb_2Te_3 heterostructures: a) NiFe(100nm) / Sb_2Te_3(10nm); b) NiFe(100nm) / Sb_2Te_3(100nm); c) NiFe(10nm) / Sb_2Te_3(100nm); d) NiFe(50nm) / Sb_2Te_3(50nm).

7.1.2 XRR

XRR was performed as described in Chapter 3 on the NiFe / Sb$_2$Te$_3$ heterostrcutures deposited on the Si substrate to obtain the layers thickness. Figure 7.3 shows the reflectivity curves. The Fresnel decay of the reflectivity is observed in all the structures as well as Kiessig fringes.
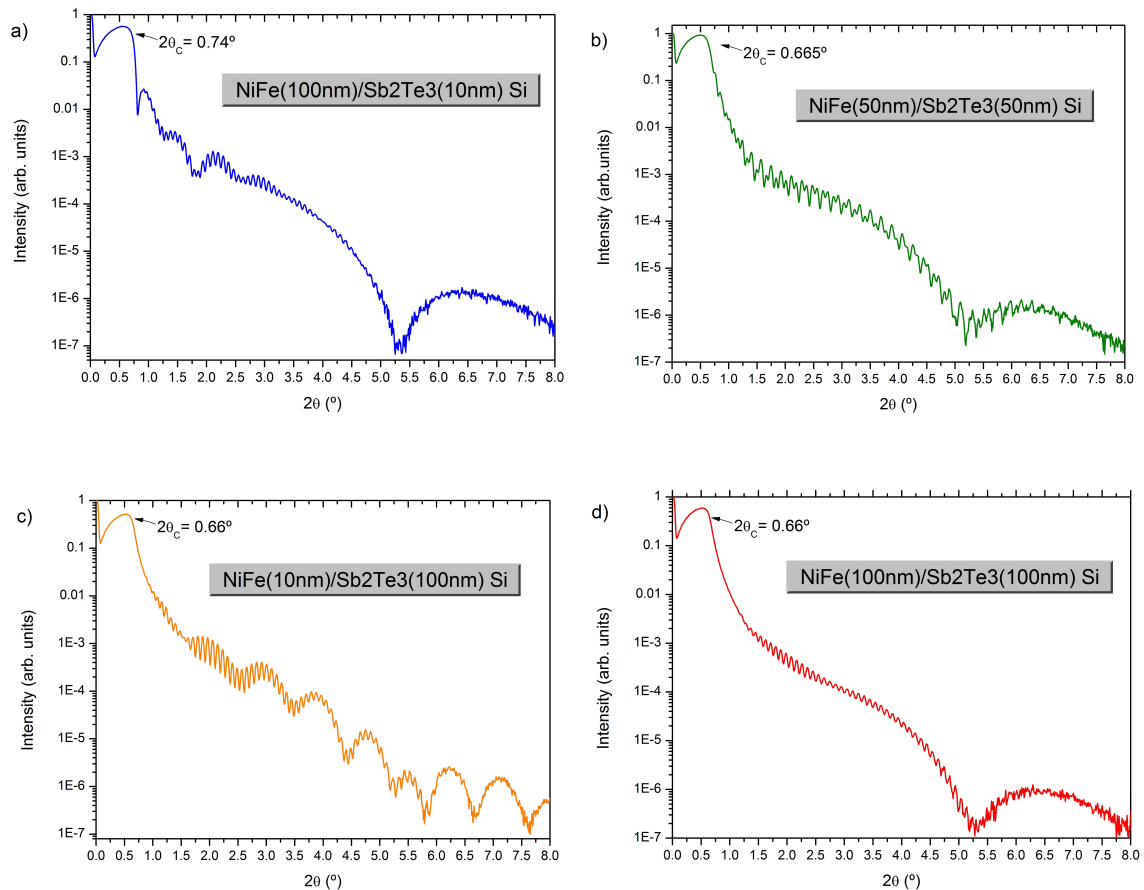
FIGURE 7.3: XRR reflectivity plots of the NiFe / Sb$_2$Te$_3$ heterostructures.

For the NiFe(100nm) / Sb$_2$Te$_3$(10nm) heterostructure, it is observed two set of Kiessig fringes, with different oscillation periods. Each set of fringes corresponds to one of the layers of the heterostructure, with the smallest oscillation period corresponding to the 100 nm NiFe layer. This situation also occurred for the NiFe(10nm) / Sb$_2$Te$_3$(100nm) heterostructure, where the smaller oscillation period corresponds to the Sb$_2$Te$_3$ 100 nm layer. Taking in consideration the reflectivity plot of the NiFe(50nm) / Sb$_2$Te$_3$(50nm), two sets of superimposed fringes are detected. Being the thickness of each layer similar, the two oscillations corresponding to each layer overlap and each fringe appears to have two

smaller fringes. With the NiFe(100nm) / Sb_2Te_3(100nm), only one set of Kiessig fringes exists.

The observed superimposed Kiessig fringes have a similar behaviour to a beating effect of two interfering sound waves. The detected wave is a superposition of the x-rays reflected at the interface between the top and the bottom layer and at the bottom of the bottom layer. These two reflections, corresponding to different layers, yield different intensities at different angles, according to their thickness. When interfered, they produce the beating pattern observed for all the heterostructures except the NiFe(100nm) / Sb_2Te_3(100nm) heterostructure. When two waves of the same period are superimposed, the intensity is identical at all angles and no beating is detected. Thus, the NiFe(100nm) / Sb_2Te_3(100nm) layers, since only one set of fringes is observed, have a practically identical thickness.

From the reflectivity plots, the thickness can be obtained following Chapter 3 and equation 3.1. In Table 7.1, the layer thicknesses for all the heterostructures are presented. These results are in great accordance with the thicknesses measured using SEM, since the observed differences are smaller than 9 nm, which is a value smaller than the SEM limit of film thickness measurement.

Heterostructure	NiFe Layer	Sb_2Te_3 Layer
NiFe(100nm) / Sb_2Te_3(10nm)	97.6 nm	12 nm
NiFe(50nm) / Sb_2Te_3(50nm)	46.19 nm	46.4 nm
NiFe(10nm) / Sb_2Te_3(100nm)	10.2 nm	98.14 nm
NiFe(100nm) / Sb_2Te_3(100nm)	88.6 nm	88.6 nm

TABLE 7.1: Layer thickness of the NiFe / Sb_2Te_3 obtained from XRR.

7.1.3 EDS

In order to verify the stoichiometry of the 100 nm NiFe thin film, EDS measurements were performed. It was obtained that the thin film is constituted by 15.37% Ni and 84.63% Fe, which corresponds to the permalloy $Ni_{0.15}Fe_{0.85}$.

7.1.4 XRD

The X-ray diffraction patterns of the NiFe thin film and of the NiFe / Sb_2Te_3 heterostructures were obtained. In Figure 7.4 the XRD pattern of the NiFe thin films deposited in Glass and in Si are presented.

On the thin film deposited in Glass, two peaks can be identified as belonging to the Ni$_{0.15}$Fe$_{0.85}$ phase, having the space group Fm-3m. This demonstrates that the substrate did not influenced the growth of a crystallographic phase. At 44°, the (1 1 1) peak is observed. The other detected peak is at approximately, 91°, corresponding to the (3 1 1) peak [83]. This shows that the thin film had a (*x* 1 1) directional growth. Furthermore, it is verified that the intensity of the (1 1 1) peak is much larger than the intensity of the (3 1 1) peak.

For the thin film deposited in Si substrate, peaks corresponding to the Si substrate are observed as well as peaks corresponding to the sample holder. The two peaks observed in the thin film deposited in glass are also detected. However, for this thin film, the (1 1 1) peak appears superimposed with the peak of the sample holder at 43.7°. The peak is still successfully identified since the intensity of the sample holder peaks is much smaller than the other peaks and also due to the asymmetry of the total peak, evidencing that two peaks are superimposed. From this, it can be concluded that on Si, the thin film also had a preferential (*x* 1 1) growth, demonstrating that there was no substrate influence in the crystallographic thin film growth.
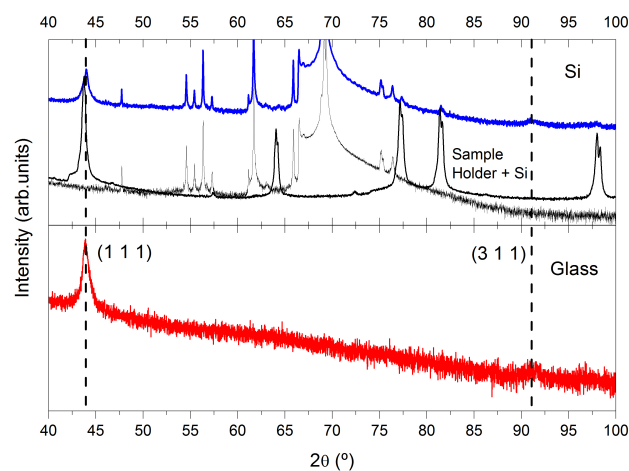
FIGURE 7.4: XRD pattern of the NiFe thin films.

The X-ray diffraction patterns of the heterostructures are represented in Figure 7.5. Focusing on the glass substrate, the traditional broad peak around 20° is observed as well as the sample holder peaks. The previously identified peaks of the Sb$_2$Te$_3$ (Subsection 6.1.4) and Ni$_{0.15}$Fe$_{0.85}$ phases are observed and their intensity depends on the heterostructure being analysed. In the heterostructure NiFe(10nm) / Sb$_2$Te$_3$(100nm), the

peaks corresponding to NiFe are not observed whereas the Sb_2Te_3 peaks are more intense. The reverse situation occurs in the NiFe(100nm) / Sb_2Te_3(10nm) structure, where the Sb_2Te_3 peaks are not observed but the NiFe peaks are detected. The XRD patterns of the NiFe(50nm) / Sb_2Te_3(50nm) and NiFe(100nm) / Sb_2Te_3(100nm) structures show all the peaks corresponding to all layers, with the intensity of NiFe increasing for the NiFe(100nm) / Sb_2Te_3(100nm) heterostructure.

For the heterostructures deposited on Si substrates, the situation is similar to the Glass substrate heterostructures. Peaks corresponding to the substrate and also to the sample holder are observed. The Sb_2Te_3 phase peaks as well as the $Ni_{0.15}Fe_{0.85}$ were also detected, having a similar behaviour to the thin films deposited in Glass. For the NiFe(100nm) / Sb_2Te_3(10nm) heterostructure no Sb_2Te_3 peaks exist, whereas for the NiFe(10nm) / Sb_2Te_3(100nm) structure only the Sb_2Te_3 peaks are visible. For the NiFe(50nm) / Sb_2Te_3(50nm) and the NiFe(100nm) / Sb_2Te_3(100nm) all the reflections are present, with an increase in intensity from the NiFe(50nm) / Sb_2Te_3(50nm) to the NiFe(100nm) / Sb_2Te_3(100nm) heterostructure reflections intensity.

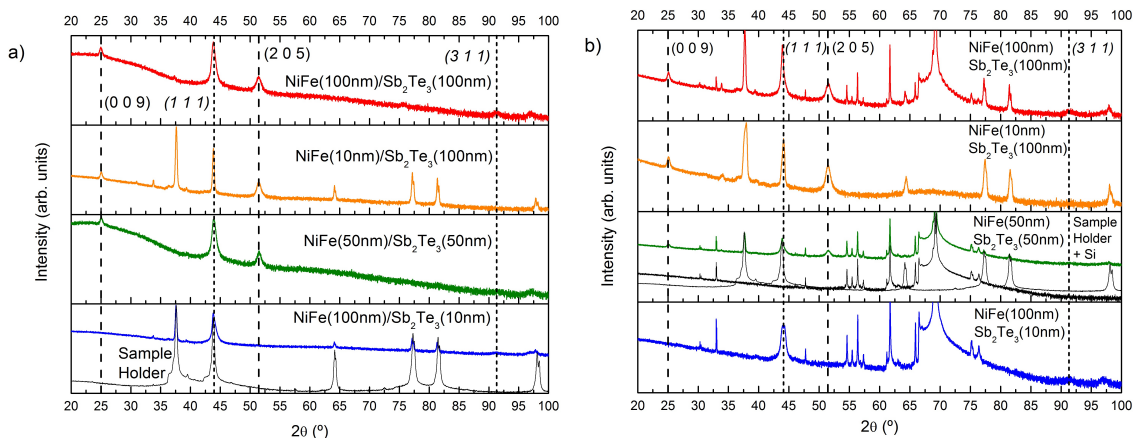
FIGURE 7.5: XRD pattern of the NiFe / Sb_2Te_3 heterostructures deposited on a) Glass and b) Si.

7.2 Electronic and Magnetic Properties

7.2.1 Resistivity

The resistivity of the 100 nm NiFe thin films as a function of temperature was measured as described in Chapter 3. Figure 7.6 shows the resistivity of the NiFe thin films as a function of temperature.

The resistivity increases with temperature for both thin films having values in th or-
der of $1 \times 10^{-7} \Omega m$. This is the characteristic behaviour of metals. Being the thin films
constituted by transition metals, this demonstrates that the metallic behaviour does not
change from bulk to thin film form. Furthermore, the resistivity behaves similarly for the
glass and Si substrate thin films. Only a small deviation is detected between the two films.
Being glass an insulator, this small difference might be due to the conductivity nature of
the Si substrate.
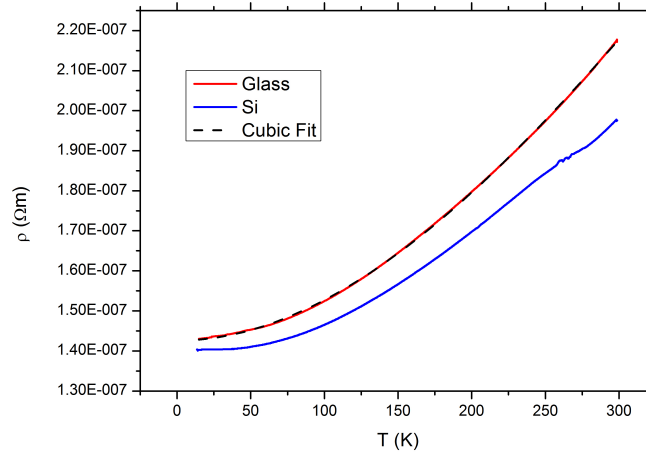
FIGURE 7.6: Resistivity of the NiFe 100 nm thin films deposited in glass and Si as a
function of temperature for temperatures between 15 and 300 K.

The resistivity of metals is explained by scattering phenomena [84]. Being the thin
films constituted by transition metals, scattering between the s-d electrons occurs, which
leads to a cubic dependence on temperature of the resistivity. Furthermore, a quadratic
dependence on the temperature can appear due to electron-electron interaction. In order
to verify the type of scattering present in the thin films, a cubic fit of the resistivity of
the thin film deposited in glass was performed and it is presented in Figure 7.6. From
the comparison of the fit with the experimental measured values, it can be estimated that
both mentioned types of scattering exist in the thin films. Thus, it is estimated that the
resistivity of the NiFe thin films is given by equation 7.1.

$$\rho(T) = \rho(0) + AT^2 + BT^3 \qquad (7.1)$$

The resistivity of the heterostructures as a function of the temperature was also mea-
sured. In Figure 7.7,the resistivity curves of the various heterostructures deposited in Si
and glass is presented as a function of temperature.
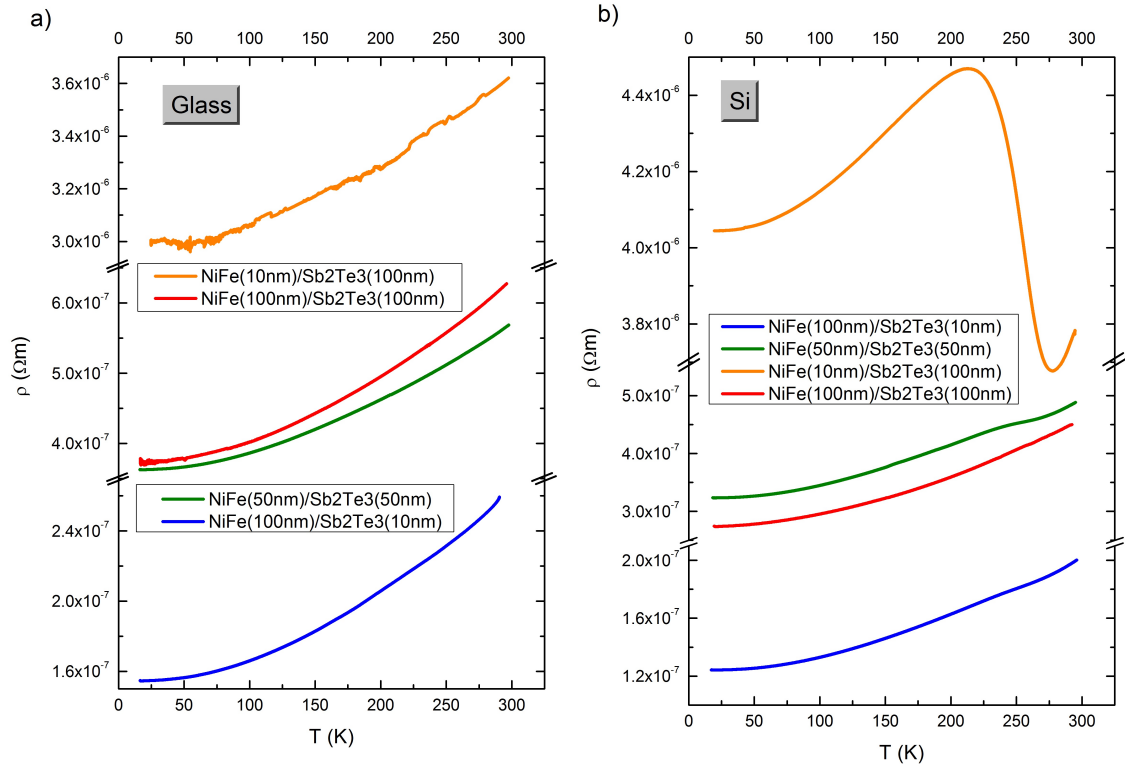
FIGURE 7.7: Resistivity of the NiFe / Sb_2Te_3 heterostructures as a function of temperature for temperature between 15 and 300 K for hetrostructures deposited in a) glass and b) si.

Analysing the heterostructures deposited in glass, it is visible that the resistivity increases with temperature. This behaviour is characteristic of metals and it was observed for the NiFe thin films resistivity presented in 7.6. Furthermore, a decrease in the value of the resistivity is observed with an increase in the Sb_2Te_3 layer thickness and a decrease in the NiFe layer thickness. For the NiFe(100nm) / Sb_2Te_3(10nm), the resistivity is of the order of $1 \times 10^{-6} \Omega m$, whereas it is of the order of $1 \times 10^{-7} \Omega m$ for the other heterostructures, reaching the same values as the NiFe thin films for the NiFe(100nm) / Sb_2Te_3(100nm). These resistivities are also much smaller than the resistivity of the Sb_2Te_3 thin films presented in subsection 6.2.3. It can thus be concluded that the main contribution to the conduction of the heterostructures comes mainly from the NiFe layer. It changes the semiconductor behaviour of the Sb_2Te_3 in thin films to a metallic behaviour in heterostructures, even with a layer thickness as small as 10 nm.

Focusing on the heterostructures deposited in Si, the resistivity starts behaving differently depending on the heterostructure. For the NiFe(100nm) / Sb_2Te_3(10nm) heterostructure, the behaviour and values of the resistivity are similar to the same heterostructure deposited in glass and to the NiFe thin films. A similar situation occurs for the NiFe(100nm)

/ Sb$_2$Te$_3$(100nm) heterostructure. It presents a similar dependence with temperature as the heterostructure deposited in Glass. However, the resistivity starts behaving differently with a decrease of the NiFe layer thickness.

For the NiFe(50nm) / Sb$_2$Te$_3$(50nm) heterostructure, at approximately 250 K, a small deviation of the monotonic increasing behaviour is observed. The resistivity of the NiFe (10nm) / Sb$_2$Te$_3$(100nm), although having the same order of magnitude as the glass heterostructure, it has a widely different temperature dependence. At low temperatures up to 215 K, the resistivity increases with temperature as observed for the other structures. At 215 K an inversion on the resistivity occurs and it starts to decreases with temperature, as it was observed in the Sb$_2$Te$_3$ thin films analysed in subsection 6.2.3. However, at 275 K, the resistivity inverts once again its behaviour, increasing with temperature up to the maximum temperature of 300K. Considering the values of the resistivity being much lower than the Sb$_2$Te$_3$ thin films resistivity values, but also higher than the NiFe thin film resistivity, it is concluded that the small 10 nm NiFe layer still plays an important role, with the Sb$_2$Te$_3$ 100 nm layer decreasing the conduction by one order of magnitude. The resistivity increase with temperature up to 215 K and for temperatures higher than 275 K is also indicative that the heterostructure still maintains some of the metallic behaviour present in the other heterostructures, originated form the NiFe layer. By comparing the resistivity values with the heterostructure deposited in glass, it is also seen that they are very similar. The observed exotic behaviour of the two heterostructures is not then caused by either the NiFe or the Sb$_2$Te$_3$ layers, but by conduction coming from the Si substrate. As observed for the Sb$_2$Te$_3$ thin films deposited in Si, the substrate has a huge influence in the transport properties. It was observed that for the Sb$_2$Te$_3$ 100 nm thin film resistivity for temperatures higher than, approximately, 200 K, there is a drastic decrease in the resistivity, which is in accordance with the behaviour presented by these heterostructures. From this, the resistivity originates then from an interplay between the smaller NiFe layer, which increases the resistivity from the Sb$_2$Te$_3$ thin film value and provides a metallic behaviour for certain temperatures; the Sb$_2$Te$_3$ layer increasing the resistivity from the NiFe thin film; and the Si substrate which causes the resistivity to decrease with temperature.

Considering all the heterostructures resistivities, it can be concluded that they have a majority metallic behaviour due to the NiFe layer, with a substrate influence that increases with a decrease in the NiFe layer thickness for heterostructures deposited in Si.

7.2.2   Seebeck

The Seebeck coefficient at room temperature of the NiFe thin films and heterostructures
was measured as described in Chapter 3. In Figure 7.8, the voltage drop across the thin
films as a function of the temperature difference is shown for the NiFe 100 nm thin films
deposited in Glass and Si. The expected linear behaviour was obtained for the two different thin films. The voltage was positive and monotonic increasing for all temperature
differences. Performing the linear fits of the presented data and following equation 3.3,
the Seebeck coefficient was obtained. The results are presented in Figure 7.8 as well as
summarised in Table 7.2.

Both thin films present a negative Seebeck coefficient. However, the Seebeck coefficient of the thin film deposited in Glass is approximately 5 times higher in magnitude
than the thin film deposited in Si. Considering that Si has an extremely high positive Seebeck coefficient, it can be concluded that the Seebeck coefficient of the NiFe thin film is
greatly influenced by the Si substrate.
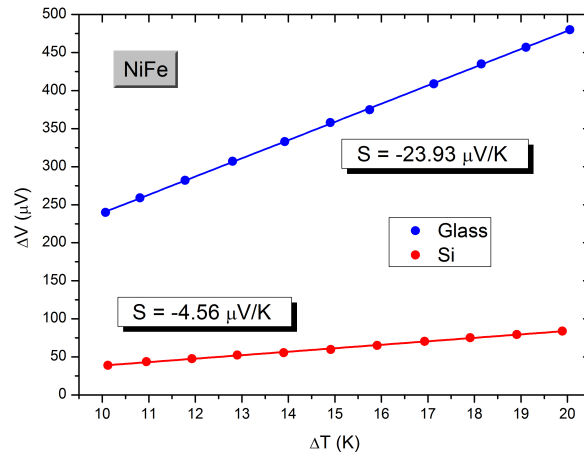
FIGURE 7.8: Seebeck Coefficient of the NiFe 100nm thin films.

In Figure 7.9, the voltage as a function of the temperature difference is presented for
the NiFe / Sb_2Te_3 heterostructures. The voltage of all the heterostrcutures had a linear
behaviour with the temperature, increasing in magnitude with an increase of the temperature. As before, from the linear fits, the Seebeck coefficients of the heterostructures were
obtained and are presented in Figure 7.9 and summarised in Table 7.2.

Analysing the heterostructures deposited in glass substrates, two distinct behaviours
are present. For the NiFe(100nm) / Sb_2Te_3(10nm), NiFe(50nm) / Sb_2Te_3(50nm) and NiFe

FIGURE 7.9: Seebeck Coefficient of the NiFe / Sb$_2$Te$_3$ heterostructures deposited in a) Glass and b) Si.

Heterostructure	Glass	Si
NiFe(100 nm)	-23.93 $\mu V/K$	-4.56 $\mu V/K$
NiFe(100nm) / Sb$_2$Te$_3$(10nm)	-23.9 $\mu V/K$	-4.35 $\mu V/K$
NiFe(50nm) / Sb$_2$Te$_3$(50nm)	-23.9 $\mu V/K$	18.02 $\mu V/K$
NiFe(10nm) / Sb$_2$Te$_3$(100nm)	-13.2 $\mu V/K$	75.2 $\mu V/K$
NiFe(100nm) / Sb$_2$Te$_3$(100nm)	-23.9 $\mu V/K$	12.3 $\mu V/K$

TABLE 7.2: Seebeck Coefficient of the Sb$_2$Te$_3$ thin films.

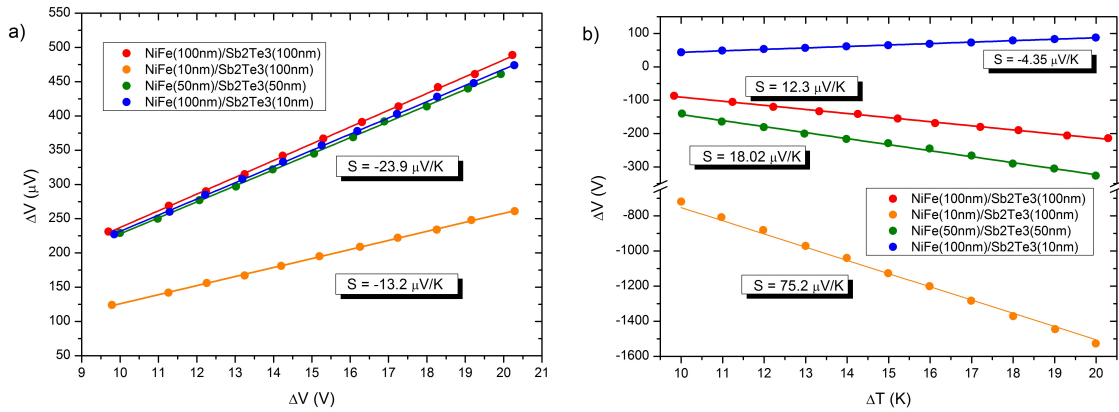(100nm) / Sb$_2$Te$_3$(100nm) heterostructures, the Seebeck coefficient had exactly the same value as the Seebeck coefficient of the NiFe thin film deposited in a glass substrate. This shows that although the Seebeck coefficient of the Sb$_2$Te$_3$ thin films with the same thicknesses is 41 $\mu V/K$, approximately two times higher in magnitude when compared to the NiFe thin film, the majority conduction contribution comes from carriers of the NiFe layer. This result is in great agreement with the resistivity of the heterostructures presented in the previous subsection 7.2.1, where it was shown that the majority contribution to the electric conduction comes from the NiFe layer.

The Seebeck coefficient of the NiFe(10nm) / Sb$_2$Te$_3$(100nm) has a smaller value in magnitude. It is still negative, which implies that the 10 nm NiFe layer still contributes with the majority of the charge carriers. However, the decrease in value shows that the larger Sb$_2$Te$_3$ layer starts to influence the heterostructure behaviour. Thus, it appears to be an interplay between the 10nm NiFe layer contributing with the majority of carriers and the 100 nm Sb$_2$Te$_3$ layer, having a Seebeck coefficient almost two times higher in magnitude than the NiFe Seebeck coefficient. Once again, these results are in accordance

with the resistivity of the heterostructure previously analysed.

Focusing on the heterostructures deposited in Si, a similar behaviour is observed. For the NiFe(100nm) / Sb_2Te_3(10nm), the Seebeck coefficient is identical to the value of the 100 nm Nife thin film deposited in Si. Once again, it is verified that the NiFe layer controls the charge transport of the heterostructure. For the other heterostructures, the Seebeck coefficient has a different behaviour, becoming positive and increasing with a reduction in the NiFe layer thickness. The Seebeck coefficient of the NiFe(100nm) / Sb_2Te_3(100nm) and NiFe(50nm) / Sb_2Te_3(50nm) heterostructure is very similar, with an increase of less than $6\mu V/K$ with the decrease in the thicknesses. However, the NiFe(10nm) / Sb_2Te_3(100nm) Seebeck coefficient is 6 times bigger than the coefficients of the other heterostructures. As previously observed, this is indicative of an interplay between the small NiFe 10 nm layer and the Si substrate influence, due to the Seebeck coefficient becoming positive but not reaching values as high as the Sb_2Te_3 thin films deposited in Si. This is also once again a behaviour identical to the observed for the resistivity of the thin films.

Chapter 8

Conclusions and Future Work

Topological Insulators are materials that present a protected metallic surface state while having an insulating bulk. The topological surface state closes the band gap in a Dirac like linear energy dispersion that is only broken in the presence of magnetic fields or magnetic materials or impurities. Nowadays, the Bi_2Te_3 family of semiconductors attracts the most attention for the realisation of the TI state and also heterostructured materials with a possible future wide range of applications.

Topological insulators based on Bi-Te and Sb-Te were fabricated. An optimised synthesis of Bi_2Te_3 was used to obtained bulk samples. A characterisation of their morphological and structural properties showed that the intended Bi_2Te_3 phase was obtained. Following these analysis, the transport properties of bulk Bi_2Te_3 were measured, and at room temperature the seebeck coefficient and resistivity were shown to be -153 $\mu V/K$ and $2.4 \times 10^{-4}\Omega m$, respectively. The values obtained are in agreement with previously reported values for bulk Bi_2Te_3. Thus, it can be concluded that the solid state reaction synthesis technique is an efficient method of bulk TI material. The electronic properties of Bi_2Te_3 were also calculated using WIEN2k and are also similar to the literature. By comparing the BoltzTraP calculated transport properties and the experimental measurements, a good agreement was also found, demonstrating that Wien2k and the BoltzTraP code are good tools to theoretically study the Bi_2Te_3 family of TI materials.

Following the successfully bulk Bi_2Te_3 studies, the realisation of Sb-Te topological insulators thin films was sought. Ion Beam Sputtering Deposition, a scalable and industrialised technique, was used to fabricate thin films with thicknesses of 10, 50, 100 and 400 nm in glass and Si substrates. Their morphology and structure was deeply analysed. It was shown that the Sb_2Te_3 phase was obtained, with an excess of Sb, and that the thin

film thickness was successfully controlled. The transport properties of the thin films were extensively studied. The resistivity showed that the thin films present an extrinsic semi-conductor behaviour, with the excess Sb acting as dopant atoms, having a resitivity of the order of $0.1\ \Omega m$ at low temperatures, whereas only $10^{-4}\Omega m$ at room temperature. From the resistivity measurements, the bulk band gap of the thin films was also obtained to be between 60 and 120 meV and it is in great accordance with its behaviour as a function of the thin films thickness. The seebeck coefficient at room temperature is also similar to previously reported values. From these results it was verified a strong substrate influence on the electronic transport of small thickness thin films, with 400 nm thin films already showing no influence at all. As for bulk Bi_2Te_3, first principle calculations of the electronic structure of bulk Sb_2Te_3 and 3 nm Sb_2Te_3 thin film, through a $1 \times 1 \times 1$ supercell calculation, were performed. Both the supercell total density of states and band structure showed the existence of the topological state. With these results, the transport properties were also calculated and an extremely good agreement was found. Magnetoresistance measurements at high magnetic fields were performed on the 100 nm Sb_2Te_3 thin film. The evidence of the existence of the Shubnikov-de Haas oscillations is present, which is a manifestation of the topological surface state. Thus, it is estimated that the fabricated Sb_2Te_3 thin films have the topological insulator behaviour.

In order to tune the possible topological surface state of the Sb-Te materials, several $NiFe/Sb_2Te_3$ heterostructures were fabricated using Ion Beam Sputtering Deposition. Prior to the heterostructures, NiFe thin films were deposited and analysed, showing good morphology, the intended structure and the expected metallic behaviour. The $NiFe/Sb_2Te_3$ heterostructures were analysed and it was demonstrated that the intended structure and morphology was obtained. The behaviour of the heterostructure transport was also preliminary analysed and showed the strong interaction between the magnetic and topological insulator layer.

On the whole, the work performed showed evidences of topological surface state on Ion Beam Sputtered Sb_2Te_3 thin films. To farther the analysis of the existence of this state and to have a complete description of its transport properties, further Magneto resistance measurements at high magnetic fields must still be pursuit. Furthermore, to improve the purity of the Sb_2Te_3 thin films, by reducing the Sb content, the thin films deposition could be made using a lower beam voltage followed by annealing treatments to reduce the polycrystalline grain size ($T_{annealing} < 350^\circ C$). Another important aspect, could be the use

of insulator substrates such as Si wafer with an oxidized surface (SiO2) or MgO, reducing the substrate influence on the transport properties of the TI. Both these processes could also improve the evidence of the topological surface state. Following these treatments and measurements, ARPES could be performed on the surface of the thin films to have a direct proof of the existence of the topological surface state.

Concerning the artificial tailoring of the TI materials, a complete analysis of the coupling of the Sb_2Te_3 layer with the NiFe layer in the $NiFe/Sb_2Te_3$ heterostructures, magnetoresistance measurements of the fabricated structures should be performed. This would give more insight into the type of coupling occurring between the two layers and ultimately tune with great precision the topological insulator properties.

First principle calculations of supercells corresponding to Sb_2Te_3 thin films with similar thicknesses as the fabricated thin films should also be performed. This would allow a direct calculation of electronic properties of the Sb_2Te_3 and a completely thorough study of these TI materials could be accomplished. Furthermore, first principle calculations of the NiFe thin films and $NiFe/Sb_2Te_3$ supercell calculations could also be carried out. As for the Sb_2Te_3 thin films and supercells, a direct comparison and more insight into the nature of the electronic properties and transport phenomena of the heterostructures would be obtained.

Bibliography

[1] Q. Niu, D. J. Thouless, and Y.-S. Wu, Physical Review B **31**, 3372 (1985).

[2] M. Franz and L. Molenkamp, *Topological Insulators*, Vol. 6 (Elsevier, 2013).

[3] J. E. Moore, Nature **464**, 194 (2010).

[4] D. Pesin and A. MacDonald, Nature Materials **11**, 409 (2012).

[5] S. Z. Butler, S. M. Hollen, L. Cao, Y. Cui, J. A. Gupta, H. R. Gutiérrez, T. F. Heinz, S. S. Hong, J. Huang, A. F. Ismach, *et al.*, ACS nano **7**, 2898 (2013).

[6] M. Z. Hasan and C. L. Kane, Reviews of Modern Physics **82**, 3045 (2010).

[7] D. Thouless, M. Kohmoto, M. Nightingale, and M. Den Nijs, Physical Review Letters **49**, 405 (1982).

[8] M. V. Berry, in *Proceedings of the Royal Society of London A: Mathematical, Physical and Engineering Sciences*, Vol. 392 (The Royal Society, 1984) pp. 45–57.

[9] C. L. Kane and E. J. Mele, Physical review letters **95**, 226801 (2005).

[10] C. L. Kane and E. J. Mele, Physical review letters **95**, 146802 (2005).

[11] L. Fu and C. L. Kane, Phys. Rev. B **74**, 195312 (2006).

[12] L. Fu and C. L. Kane, Phys. Rev. B **76**, 045302 (2007).

[13] L. Fu, C. L. Kane, and E. J. Mele, Phys. Rev. Lett. **98**, 106803 (2007).

[14] J. E. Moore and L. Balents, Phys. Rev. B **75**, 121306 (2007).

[15] R. Roy, Phys. Rev. B **79**, 195322 (2009).

[16] A. K. Geim and K. S. Novoselov, Nature materials **6**, 183 (2007).

[17] H. B. Nielsen and M. Ninomiya, Physics Letters B **130**, 389 (1983).

[18] B. A. Bernevig, T. L. Hughes, and S.-C. Zhang, Science **314**, 1757 (2006).

[19] M. König, S. Wiedmann, C. Brüne, A. Roth, H. Buhmann, L. W. Molenkamp, X.-L. Qi, and S.-C. Zhang, Science **318**, 766 (2007).

[20] D. Hsieh, D. Qian, L. Wray, Y. Xia, Y. S. Hor, R. J. Cava, and M. Z. Hasan, Nature (2008).

[21] G. J. Snyder and E. S. Toberer, Nature materials **7**, 105 (2008).

[22] B. Lenoir, A. Dauscher, X. Devaux, R. Martin-Lopez, Y. I. Ravich, H. Scherrer, and S. Scherrer, in *Thermoelectrics, 1996., Fifteenth International Conference on* (IEEE, 1996) pp. 1–13.

[23] D. Hsieh, Y. Xia, D. Qian, L. Wray, F. Meier, J. H. Dil, J. Osterwalder, L. Patthey, A. V. Fedorov, H. Lin, A. Bansil, D. Grauer, Y. S. Hor, R. J. Cava, and M. Z. Hasan, Phys. Rev. Lett. **103**, 146401 (2009).

[24] A. Nishide, A. A. Taskin, Y. Takeichi, T. Okuda, A. Kakizaki, T. Hirahara, K. Nakat-suji, F. Komori, Y. Ando, and I. Matsuda, Phys. Rev. B **81**, 041309 (2010).

[25] J. Moore, Nature Physics **5**, 378 (2009).

[26] Y. Xia, L. Wray, D. Qian, D. Hsieh, A. Pal, H. Lin, A. Bansil, D. Grauer, Y. Hor, R. Cava, *et al.*, arXiv preprint arXiv:0812.2078 (2008).

[27] H. Zhang, C.-X. Liu, X.-L. Qi, X. Dai, Z. Fang, and S.-C. Zhang, Nature physics **5**, 438 (2009).

[28] A. Damascelli, Physica Scripta **2004**, 61 (2004).

[29] Y. Chen, J. Analytis, J.-H. Chu, Z. Liu, S.-K. Mo, X.-L. Qi, H. Zhang, D. Lu, X. Dai, Z. Fang, *et al.*, Science **325**, 178 (2009).

[30] C. Riedl, C. Coletti, T. Iwasaki, A. Zakharov, and U. Starke, Physical review letters **103**, 246804 (2009).

[31] D. Hsieh, Y. Xia, L. Wray, D. Qian, A. Pal, J. Dil, J. Osterwalder, F. Meier, G. Bihlmayer, C. Kane, *et al.*, Science **323**, 919 (2009).

[32] G. Wang, X. Zhu, J. Wen, X. Chen, K. He, L. Wang, X. Ma, Y. Liu, X. Dai, Z. Fang, *et al.*, Nano Research **3**, 874 (2010).

[33] P. Roushan, J. Seo, C. V. Parker, Y. S. Hor, D. Hsieh, D. Qian, A. Richardella, M. Z. Hasan, R. J. Cava, A. Yazdani, and et al., Nature **460**, 1106–1109 (2009).

[34] S. Souma, K. Kosaka, T. Sato, M. Komatsu, A. Takayama, T. Takahashi, M. Kriener, K. Segawa, and Y. Ando, Physical review letters **106**, 216803 (2011).

[35] M. Saleemi, M. S. Toprak, S. Li, M. Johnsson, and M. Muhammed, Journal of Materials Chemistry **22**, 725 (2012).

[36] E. Rogacheva, A. Budnik, A. Y. Sipatov, O. Nashchekina, and M. Dresselhaus, Applied Physics Letters **106**, 053103 (2015).

[37] D.-X. Qu, Y. S. Hor, and R. J. Cava, Physical review letters **109**, 246602 (2012).

[38] P. H. Le, P.-T. Liu, C. W. Luo, J.-Y. Lin, and K. H. Wu, Journal of Alloys and Compounds **692**, 972 (2017).

[39] Y. S. Kim, M. Brahlek, N. Bansal, E. Edrey, G. A. Kapilevich, K. Iida, M. Tanimura, Y. Horibe, S.-W. Cheong, and S. Oh, Physical Review B **84**, 073109 (2011).

[40] H.-T. He, G. Wang, T. Zhang, I.-K. Sou, G. K. Wong, J.-N. Wang, H.-Z. Lu, S.-Q. Shen, and F.-C. Zhang, Physical Review Letters **106**, 166805 (2011).

[41] X. Wu, X. Li, Z. Song, C. Berger, and W. A. de Heer, Physical review letters **98**, 136801 (2007).

[42] S. Hikami, A. I. Larkin, and Y. Nagaoka, Progress of Theoretical Physics **63**, 707 (1980).

[43] P. Adroguer, W. E. Liu, D. Culcer, and E. Hankiewicz, Physical Review B **92**, 241402 (2015).

[44] S. L. and d. H. W. J., in *Proceedings of the Royal Netherlands Academy of Arts and Science.* (Royal Netherlands Academy of Arts and Science., 1930) pp. 363–378.

[45] D. E. Soule, J. W. McClure, and L. B. Smith, Phys. Rev. **134**, A453 (1964).

[46] D. Mo, W. Wang, and Q. Cai, Nanoscale research letters **11**, 354 (2016).

[47] D.-X. Qu, Y. S. Hor, J. Xiong, R. J. Cava, and N. Ong, Science **329**, 821 (2010).

[48] C. Weyrich, T. Merzenich, J. Kampmeier, I. Batov, G. Mussler, J. Schubert, D. Grützmacher, and T. Schäpers, Applied Physics Letters **110**, 092104 (2017).

[49] L. Pereira, M. Van Bael, K. Temst, A. Vantomme, *et al.*, Journal of Physics D: Applied Physics **44**, 215001 (2011).

[50] W. Zhou and Z. L. Wang, *Scanning microscopy for nanotechnology: techniques and applications* (Springer science & business media, 2007).

[51] I. Gomes, B. Almeida, A. Lopes, J. Araújo, J. Barbosa, and J. Mendes, Journal of Magnetism and Magnetic Materials **322**, 1174 (2010).

[52] *X-ray diffraction technique, Advanced Laboratory II, Department of Physics and Astronomy of the Faculty of Siences of the Univeristy of Porto* (2016).

[53] A. M. T. Pereira, *Rare-Earth Nanostratified Compounds With Novel Potentialities for Refrigeration and Magnetic Sensors*, Ph.D. thesis, Faculty of Sciences of the Univeristy of Porto (2010).

[54] A. L. Pires, *New Nanogenerators for Thermal Energy Harvesting - Activity Report*, Tech. Rep. (IFIMUP-IN - Materials Physics Institute of the University of Porto - Nanoscience and Nanotechnology Institute, 2017).

[55] V. Fock, Zeitschrift für Physik **61**, 14 (1930).

[56] P. Hohenberg and W. Kohn, Physical review **136**, B864 (1964).

[57] S. Cottenier, Instituut voor Kern-en Stralingsfysica, KU Leuven, Belgium **4**, 41 (2002).

[58] D. J. Singh and L. Nordstrom, *Planewaves, Pseudopotentials, and the LAPW method* (Springer Science & Business Media, 2006).

[59] Y. Xia, D. Qian, D. Hsieh, L. Wray, A. Pal, H. Lin, A. Bansil, D. Grauer, Y. Hor, R. Cava, and M. Hasan, Nature Physics (2009).

[60] G. K. Madsen and D. J. Singh, Computer Physics Communications **175**, 67 (2006).

[61] R. Euwema, D. Stukel, T. Collins, J. DeWitt, and D. Shankland, Physical Review **178**, 1419 (1969).

[62] D. Koelling and J. Wood, Journal of Computational Physics **67**, 253 (1986).

[63] W. E. Pickett, H. Krakauer, and P. B. Allen, Physical Review B **38**, 2721 (1988).

[64] P. Blaha, K. Schwarz, and J. Luitz, WIEN2k-FAQ (2001).

[65] T. Scheidemantel, C. Ambrosch-Draxl, T. Thonhauser, J. Badding, and J. Sofo, Physical Review B **68**, 125210 (2003).

[66] M. Safarov, Zhurnal Neorganicheskoj Khimii **39**, 1225 (1994).

[67] J. Navratil, I. Klichova, S. Karamazov, J. Šrámková, and J. Horak, Journal of Solid State Chemistry **140**, 29 (1998).

[68] H. Zhang, C.-x. Liu, X.-l. Qi, X. Dai, Z. Fang, and S.-c. Zhang, Nature Physics **5**, 438 (2009).

[69] H. Shi, D. Parker, M.-H. Du, and D. J. Singh, Physical Review Applied **3**, 014004 (2015).

[70] H. Zhang, H. Yu, and G. Yang, EPL (Europhysics Letters) **95**, 56002 (2011).

[71] B. Zheng, Y. Sun, J. Wu, M. Han, X. Wu, K. Huang, and S. Feng, Journal of Physics D: Applied Physics **50**, 105303 (2017).

[72] P. Kuznetsov, B. Shchamkhalova, V. Yapaskurt, V. Shcherbakov, V. Luzanov, G. Yakushcheva, V. Jitov, and V. Sizov, Journal of Crystal Growth **471**, 1 (2017).

[73] D. K. Schroder, *Semiconductor material and device characterization* (John Wiley & Sons, 2006).

[74] T.-A. Nguyen, D. Backes, A. Singh, R. Mansell, C. Barnes, D. A. Ritchie, G. Mussler, M. Lanius, D. Grützmacher, and V. Narayan, Scientific reports **6** (2016).

[75] W. Procarione and C. Wood, physica status solidi (b) **42**, 871 (1970).

[76] R. Sehr and L. Testardi, Journal of Physics and Chemistry of Solids **23**, 1219 (1962).

[77] B.-T. Wang, P. Souvatzis, O. Eriksson, and P. Zhang, The Journal of chemical physics **142**, 174702 (2015).

[78] Z. Li, C. Si, J. Zhou, H. Xu, and Z. Sun, ACS applied materials & interfaces **8**, 26126 (2016).

[79] J.-M. Zhang, W. Ming, Z. Huang, G.-B. Liu, X. Kou, Y. Fan, K. L. Wang, and Y. Yao, Physical Review B **88**, 235131 (2013).

[80] A. Lawal, A. Shaari, R. Ahmed, and N. Jarkoni, Results in Physics **7**, 2302 (2017).

[81] M. Boon, Physical Review B **7**, 761 (1973).

[82] Y. Kopelevich, R. Da Silva, B. Camargo, and A. Alexandrov, Journal of Physics: Condensed Matter **25**, 466004 (2013).

[83] A. Ramsden and E. Cameron, American Mineralogist **51**, 37 (1966).

[84] P. L. Rossiter, *The electrical resistivity of metals and alloys* (Cambridge university press, 1991).